NOVEL ASTROPHYSICAL AND COSMOLOGICAL SIGNATURES OF A SELF-INTERACTING DARK SECTOR

A thesis
submitted to the
Tata Institute of Fundamental Research, Mumbai
for the Degree of Doctor of Philosophy
in Physics

by

ANIRBAN DAS

Department of Theoretical Physics
Tata Institute of Fundamental Research, Mumbai

June 2019

Final version submitted in October, 2019

Anirban Das
Novel Astrophysical and Cosmological Signatures of a Self-Interacting Dark Sector,

To my loving parents and my sister

DECLARATION

This thesis is a presentation of my original research work. Wherever contributions of others are involved, every effort is made to indicate this clearly, with due reference to the literature, and acknowledgement of collaborative research and discussions.

The work was done under the guidance of Dr. Basudeb Dasgupta, at the Tata Institute of Fundamental Research, Mumbai.

Mumbai, October 2019

Anirban Das. 01/10/2019

Anirban Das

In my capacity as the advisor of the candidate's thesis, I certify that the above statements are true to the best of my knowledge.

Mumbai, October 2019

01/10/2019

Dr. Basudeb Dasgupta

A man is not old as long as he is seeking something.

— Jean Rostand

ABSTRACT

Dark matter accounts for about one quarter of the Universe. The galaxies and galaxy clusters are thought to be surrounded by halo-like structures consisting of dark matter. Yet its particle nature continues to remain unknown. We know about its macroscopic behaviour from various astrophysical and cosmological observations. We know that the dark matter particles do not interact strongly with the visible particles, such as protons and electrons. They are nonrelativistic, i. e., cold, and essentially collisionless, i. e., they do not interact much with each other as well. However, we do not know whether the dark matter particles are *exactly* collisionless and if not, when they became nonrelativistic and collisionless.

Interestingly, a 'small' amount of self-interaction between the dark matter particles help explain a few astronomical observations better. Long range self-interaction would also have important implications for dark matter detection experiments due to the Sommerfeld effect which can enhance/suppress dark matter annihilation rate. If cold dark matter is formed 'late', then that would affect the large scale structure formation etc.

In this thesis, we studied the novel changes expected in the astrophysical and cosmological observables if dark matter is not perfectly collisionless and was not cold at early times. We studied the nontrivial effects of *long range* self-interaction in multilevel dark matter model. Firstly, we show that a simple particle exchange symmetry can lead to a angular momentum and spin dependent selection rule in Sommerfeld effect. Thus p-wave annihilation, which is otherwise velocity-suppressed, could dominate the dark matter annihilation today. Moreover, the p-wave nature of the annihilation process would predict a large annihilation rate in the Milky Way-like galaxies, more than either in galaxy clusters or dwarf galaxies. Secondly, dark matter particles with multiple states can experience inelastic scattering in addition to the elastic scattering. We computed the scattering cross sections in a multilevel dark matter model and showed that inelastic scattering induced decay could lead to a new mechanism for halo cooling, and additional drag force between two colliding halos. Lastly, to investigate when dark matter became cold and collisionless, we studied the changes in the cosmological observables if the cold dark matter is formed *late* from a relativistic collisional fluid. We call it ballistic dark matter because of its ballistic bulk motion inherited from the acoustic oscillations in the primordial fluid. This bulk motion causes oscillations in the matter power spectrum at small scales. The envelope of the oscillations is enhanced relative to the power spectrum in the standard model of cosmology. We also give approximate analytic treatment of the density fluctuations in the ballistic dark matter fluid.

PUBLICATIONS

Papers included in the thesis –

1. Paper I [1]
   Selection rule for enhanced dark matter annihilation
   Anirban Das and Basudeb Dasgupta
   Phys.Rev.Lett. 118 (2017) no.25, 251101
   arXiv:1611.04606

2. Paper II [2]
   New dissipation mechanisms from multi-level dark matter scattering
   Anirban Das and Basudeb Dasgupta
   Phys.Rev. D97 (2018) no.2, 023002
   arXiv:1709.06577

3. Paper III [3]
   Ballistic Dark Matter oscillates above ΛCDM
   Anirban Das, Basudeb Dasgupta, and Rishi Khatri
   JCAP 04 (2019) 018
   arXiv:1811.00028

Papers not included in the thesis –

1. *New effects of non-standard self-interactions of neutrinos in a supernova*
   Anirban Das, Amol Dighe, and Manibrata Sen
   JCAP 1705 (2017) no.05, 051
   arXiv:1705.00468

2. *A tale of two dark neighbors: WIMP n′ axion*
   Suman Chatterjee, Anirban Das, Tousik Samui, and Manibrata Sen
   arXiv:1810.09471

CODES

Codes developed or used in this thesis –

1. Code for Wilson coefficient matching
   Available at https://github.com/anirbandas89/NREFT_Matching.

2. Code for Ballistic Dark Matter perturbation evolution
   Available at https://github.com/anirbandas89/BDM_CLASS.

ACKNOWLEDGMENTS

This work would not have been possible without the support and help from many people.

Foremost, I would like to thank and express my sincere gratitude to my advisor Dr. Basudeb Dasgupta for giving me the opportunity to work with him at such an esteemed department in TIFR, and introducing me to the fascinating area of astroparticle physics and cosmology. His motivation and enthusiasm have immensely helped me throughout my Ph.D. life. He has always been very supportive to me to learn new things. He encouraged me not only to think critically, be independent in my research, but also to improve the essential soft-skills. I cannot thank him enough for his generous financial support through the Max Planck Partner Group for Astroparticle Physics.

The Department of Theoretical Physics in TIFR undoubtedly is one of the best places in India for its unparalleled research atmosphere. I really enjoyed being here and my collaboration with Prof. Amol Dighe and Prof. Rishi Khatri. I learned many new things from the stimulating discussion sessions with them. A warm thanks to them. I have benefited a lot from the cosmology and astroparticle physics group journal club. My sincere thanks to Prof. Tuhin Roy, Prof. Rajdeep Sensarma, Prof. Rishi Sharma, Prof. Nilmani Mathur for their courses and insightful discussions. I would like to thank Mr. Kapil Ghadiali and Mr. Ajay Salve for their prompt and efficient help with any technical needs, and the department office staff Mr. Raju Bathija, Mr. Girish Ogale, Mr. Rajendra Pawar, and Mr. Aniket Surve.

I would like to thank Mr. Vladyslav Shtabovenko for his help with `FeynCalc` package during my first project. I also thank Prof. Steen Hannestad, Prof. Alejandro Ibarra, Prof. Georg Raffelt, Prof. Pasquale Serpico, and Prof. Christoph Weniger for their support and useful discussions during my academic visits. Many thanks to the IndoFrench Collaboration on High Energy Physics for their financial support through CNRS LIA (Laboratoire International Associé) for my visit to LAPTh, Annecy.

It was a wonderful experience being around my fellow Ph.D. students – Abhisek, Ahana, Anupam, Disha, Krishnendu, Manibrata, Sarbajaya, Shubhajit, Sounak, Srimanta, Tousik, Vishal, and many others. Many thanks to them for all the help, and being good friends.

Above all, my deepest gratitude to my parents and my sister who have always stood by me throughout my Ph.D. life and encouraged me to pursue my dream. I will always be indebted to them.

CONTENTS

LIST OF FIGURES

ACRONYMS

SM – Standard Model

DM – Dark Matter

CMB – Cosmic Microwave Background

CDM – Cold Dark Matter

BDM – Ballistic Dark Matter

DE – Dark Energy

DR – Dark Radiation

ΛCDM – Cold Dark Matter with cosmological constant Λ

ΛBDM – Ballistic Dark Matter with cosmological constant Λ

CMB – Cosmic Microwave Background

SPH – Smoothed Particle Hydrodynamics

SIDM – Self-Interacting Dark Matter

NREFT – Nonrelativistic Effective Field Theory

NRQED – Nonrelativistic Quantum Electrodynamics

1

INTRODUCTION

All known ordinary matter– the stars, galaxies, luminous and non-luminous gas clouds etc., that we see around us, forms only a subdominant 5% of the total energy content in our Universe. The rest of it is inferred to be residing in other forms whose true nature is still unknown to us [4–8]. The observation that the Universe is undergoing an accelerated expansion today gives us a hint that it is dominated by a hypothetical *Dark Energy* (DE), that could be the cosmological constant Λ, making up about 68% of the total energy density [9, 10]. The second most dominant part of the Universe is called *Cold Dark Matter* (CDM). It is the nonrelativistic matter which is needed to explain the formation of large structures, such as galaxies and clusters of galaxies etc [11]. This ΛCDM model, that includes DE and

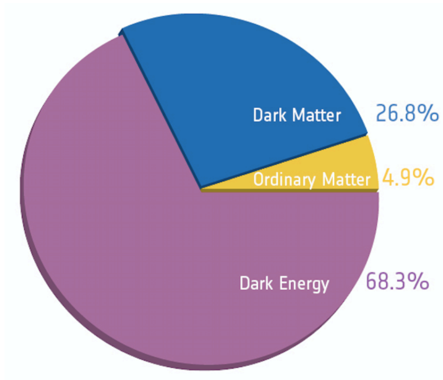

Figure 1.1: The energy budget of today's Universe. Image courtesy: ESA Science & Technology [12].

CDM, is the most compelling theory of the modern cosmology. It has been overwhelmingly successful in explaining many observations, like the accelerated expansion of the Universe, the formation of large scale structure, the anisotropies in the temperature and polarization of the relic of the primordial radiation, formation of stars and galaxies etc.

In this chapter, we shall give a brief introduction to the history of the Universe according the ΛCDM model, discuss about evidences and propositions about DM, concluding with a few unsettled issues with this cosmological theory.

1.1 OUR SPACETIME

The Universe is observed to be homogeneous and isotropic at large scales ($\gtrsim 100\,\mathrm{Mpc}$). From the observations of various galaxy surveys, we have seen that locally averaged galaxy density is homogeneous and the same in every direction on large scales. This fact dictates the symmetries of the spacetime telling us that the spatial part of the metric is isotropic and homogeneous while it expands with time. The Friedmann-Lemaître-Robertson-Walker (FLRW) metric has these properties [13–15],

$$ds^2 = dt^2 - a(t)^2 \left[\frac{dr^2}{1-kr^2} + r^2 \left(\sin^2\theta d\theta^2 + d\phi^2 \right) \right] . \tag{1.1}$$

Here the scale factor $a(t)$ is a function of time and denotes the expansion of the Universe with time. It is evident that the spatial part of the metric within square brackets signifies homogeneity and isotropy at any given instance of time. The parameter k determines the curvature of a spatial hypersurface. It can take only three values– $k = 0, +1$ or -1. The zero value of k means the Universe is spatially flat (zero curvature), and $k = +1$ or -1 means the it is closed or open, respectively. Our Universe is observed to be flat within a good precision [4]. In the rest of this thesis, we shall only consider the case $k = 0$.

It is suggestive to redefine the time coordinate to define the useful notion of the conformal time τ as follows,

$$d\tau = \frac{dt}{a(t)} . \tag{1.2}$$

In terms of the conformal time, the FLRW metric reads[1]

$$ds^2 = a^2(\tau) \left[d\tau^2 - dr^2 - r^2 \left(\sin^2\theta d\theta^2 + d\phi^2 \right) \right] . \tag{1.3}$$

Very often, conformal time τ is used in place of t to follow the evolution of various quantities.

The Universe is expanding at an accelerated pace which we can infer from the redshifted light from receding distant galaxies. This expansion is encoded in the time variation of the scale factor $a(t)$, which is conveniently chosen to be unity at present time. Using the FLRW metric, the *physical* distance between two points is increasing as $d_{\rm phys} = a(t) d_{\rm co}$ where $d_{\rm co}$ denotes the *comoving* distance. The distance to far away objects are often quoted in terms of redshift z. It is defined as

$$1 + z = \frac{1}{a} \tag{1.4}$$

which means today is redshift $z = 0$.

The Einstein equation describes the evolution of the metric under the influence of the stress energy $T_{\mu\nu}$ residing in it (including the part coming from the metric itself).

$$R_{\mu\nu} - \frac{1}{2} g_{\mu\nu} R = 8\pi G T_{\mu\nu} . \tag{1.5}$$

Here $R_{\mu\nu}$ and R are the Ricci tensor and the scalar, respectively. They depend on the metric $g_{\mu\nu}$ and its derivatives, and measure the curvature of

1 This form of the FLRW metric tells us that it is conformal to the Minkowski spacetime with $a(\tau)^2$ as the conformal factor. See Ref. [16] for more discussion.

the spacetime. The stress energy tensor is denoted as $T_{\mu\nu}$. In this chapter, we shall assume that the stress energy is constant throughout space. The effects of inhomogeneities will be discussed in a later chapter. A perfect isotropic fluid can be completely described by its energy ρ and pressure p, and has a stress-energy tensor

$$T^{\mu}{}_{\nu} = \begin{pmatrix} -\rho & 0 & 0 & 0 \\ 0 & p & 0 & 0 \\ 0 & 0 & p & 0 \\ 0 & 0 & 0 & p \end{pmatrix} . \tag{1.6}$$

Almost all components of the Universe behave like perfect fluid except during a few transient periods where particle annihilation, phase transition etc. take place. Apart from these transient phases, the total stress energy tensor can be well approximated by Eq.(1.6). Now, Eqs.(1.1) and (1.6) can be used to write down the two independent Einstein equations as

$$\begin{aligned} \left(\frac{\dot{a}}{a}\right)^2 &= \frac{8\pi G\rho}{3} + \frac{\Lambda}{3} , \\ 2\left(\frac{\ddot{a}}{a}\right) + \left(\frac{\dot{a}}{a}\right)^2 &= -8\pi G p + \Lambda . \end{aligned} \tag{1.7}$$

Here Λ is the cosmological constant. These are known as the Friedmann equations and describe the expansion of the Universe. The need for Λ will be explained in the next section. The first equation in Eq.(1.7) can be recast in another convenient form by defining the quantities: Hubble parameter $H = \dot{a}/a$, and critical density $\rho_c = 3H_0^2/(8\pi G)$,

$$\left(\frac{H}{H_0}\right)^2 = \frac{\rho}{\rho_c} \equiv \Omega , \tag{1.8}$$

where $H_0 = 73.52 \pm 1.62\ \mathrm{km\,s^{-1}\,Mpc^{-1}}$ is the Hubble parameter today [17][2]. The second equation in Eq.(1.7) describe the acceleration of the expansion.

1.2 EVOLUTION OF ENERGY

Although the stress energy $T^{\mu}{}_{\nu}$ is homogeneous throughout space, it evolves with time. The evolution equation for ρ and p follow from the energy-momentum conservation equation $T^{\mu}{}_{\nu;\mu} = 0$,

$$\frac{\partial\rho}{\partial t} + 3\frac{\dot{a}}{a}(\rho + p) = 0 . \tag{1.9}$$

Different components of the stress energy tensor can be collectively described using the equation of state (EoS) w which relates the energy and pressure,

$$p = w\rho . \tag{1.10}$$

2 This value was obtained from the MW Cepheid measurement. Hubble parameter inferred from CMB observation experiments is $H_0 = 67.36 \pm 0.54\ \mathrm{km\,s^{-1}\,Mpc^{-1}}$ [4] which is 3.6σ away from the value in Ref. [17]. The reason behind this mismatch between the values of the Hubble parameter from CMB experiments and low-redshift measurement data is not yet understood and is a topic of current research.

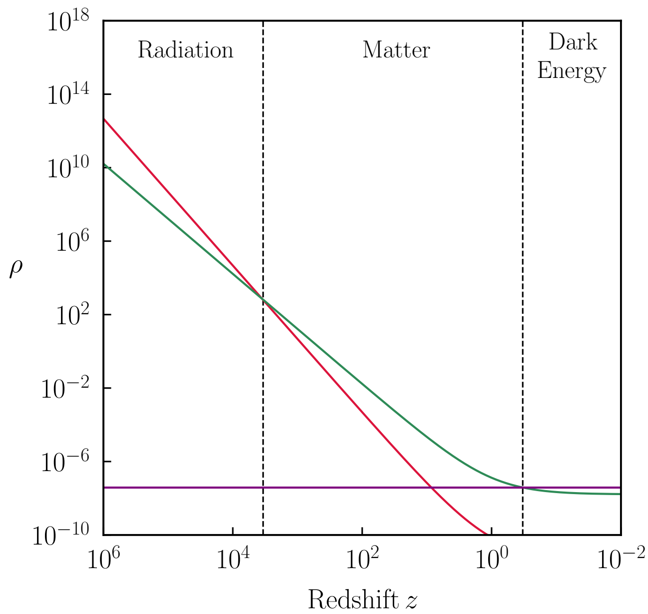

Figure 1.2: Evolution of the energy densities ρ with redshift z. The radiation density behaves as $\sim (1+z)^4$ (red), matter behaves as $\sim (1+z)^3$ (green) while DE density is constant (purple). The vertical dashed lines denote the boundaries between radiation, matter, and DE dominated eras.

The EoS of relativistic particles (radiation), nonrelativistic particles (matter), and cosmological constant are given by,

$$w = \begin{cases} \frac{1}{3} & \text{Radiation} \\ 0 & \text{Matter} \\ -1 & \text{Cosmological constant} \end{cases} \tag{1.11}$$

Eqs.(1.7) and (1.9) form the complete set of equations that describe the evolution of the homogeneous Universe and its contents.

As the Universe is expanding, the energy densities of all species are decreasing, but at different rates. For nonrelativistic matter, assuming the total number of particles is unchanged, their number density goes down as $\sim 1/a^3$ where m is the mass of each particle. This is because any physical length in each dimension is expanding as $\sim a$. Therefore, the energy density of matter $\rho_m = mn \sim 1/a^3$.

For radiation, the energy of individual particle 'redshifts' as $\sim 1/a$ in addition to the $1/a^3$ decrease of their number density. The energy density of relativistic particles, therefore, decreases as $\rho_r \sim 1/a^4$. If the radiation is in thermal equilibrium, then it has a well-defined temperature T. As the total energy density $\rho_r \sim T^4$, we can see that the temperature T redshifts as $T \sim 1/a$.

The idea of cosmological constant or dark energy was conceived to explain the accelerated expansion of the Universe [9, 10]. Its energy density is constant throughout space and does not evolve with time either. In Fig. 1.2, we have shown the evolution of different species with redshift.

1.3 THERMAL HISTORY

At very early time, all visible particles were 'hot', i. e., relativistic, and in thermal equilibrium sharing the same temperature T as the photons. As the Universe expanded, the temperature cooled down, and particles fell out of chemical and kinetic equilibrium. If Γ is the scattering rate leading to the thermalization, then this process becomes inefficient when the rate Γ falls below the expansion rate of the Universe $H = \dot{a}/a$, also known as the Hubble rate. When this happens the scattering is not fast enough to keep the participating particle baths in equilibrium, and they start to evolve independently.

At temperature above $T > 10$ MeV, the protons (p), neutrons (n), electrons (e^-), positrons (e^+), neutrinos (ν), and photons (γ) were in thermal equilibrium. The epoch $T \simeq 10$ to 0.1 MeV is known as the epoch of Big Bang Nucleosynthesis (BBN). During this time, the protons and neutrons had cooled down enough to form bound nuclei, and the first light elements started forming. The measured abundance of light elements like Deuterium (D), Helium (^3He,^4He), and lithium (^7Li) in today's Universe gives us useful information about BBN epoch. Also at around $T \sim 1$ MeV, the process $e^+e^- \leftrightarrow \bar{\nu}\nu$ becomes slower than the Hubble rate, and the neutrinos decouple from the thermal bath. The time period since the Big Bang until $z_{\rm eq} \simeq 3400$ ($T \simeq 3$ eV) is radiation dominated (RD) era, as the total energy density in the Universe is dominated by the relativistic energy. The matter and radiation energy density became equal at $z_{\rm eq} \simeq 3400$ when the Universe became matter dominated (MD). The important event is the recombination. When the temperature became $T \lesssim 0.1$ eV, the free electrons and protons formed bound states of neutral hydrogen and other atoms. As the Universe mostly consisted of neutral atoms after recombination, the photons started freely propagating without much scattering. Hence, the epoch just after recombination is known the 'surface of last scattering' of the cosmic photons. It is this background of cosmic photons that we see today as the Cosmic Microwave Background (CMB). It has maintained its primordial Planck spectrum, but the temperature has redshifted to a temperature $T = 2.7255 \pm 0.0006\,\mathrm{K}$ [18]. The DE dominated period started very late, at $z \simeq 0.3$. The thermal history of DM is model-dependent, and will be discussed in the next section.

1.4 DARK MATTER

CDM is an essential component of our Universe with $\Omega_c = 0.267$. It is thought to be a substance that does not interact much with the visible part of the Universe except via gravity. So far, all evidences of DM are through its gravitational interaction with the visible part.

1.4.1 *Evidences*

Diverse lines of experiments and observations at different length scales imply existence of DM. At Gpc or larger scales, the observation of the CMB gives us hint about DM. Experiments, such as WMAP [19], Planck [4], have measured the tiny fluctuations in the temperature and polarizations of the CMB sky map with great precision. Among other things, these fluctuations depend on the net amount of CDM in the Universe. The observed angular power spectra of the anisotropies can be explained very well within the ΛCDM paradigm. An excellent discussion about the physics of the CMB can be found in Ref. [20] (Also see the tutorial in Ref. [21]).

Observation of mergers of galaxy clusters also points towards presence of CDM in those objects. Structures like galaxies and galaxy clusters are thought to be surrounded by *halos* of DM. Merger of galaxy clusters, like 1E0657-558 (Bullet cluster) [11], MACSJ0025.4-1222 [22], MS 1054-0321 [23] etc. have shown a systematic displacement between the positions of X-ray emitting hot gas distributions and the distribution of the 'invisible mass' in the cluster using gravitational weak lensing. These observations

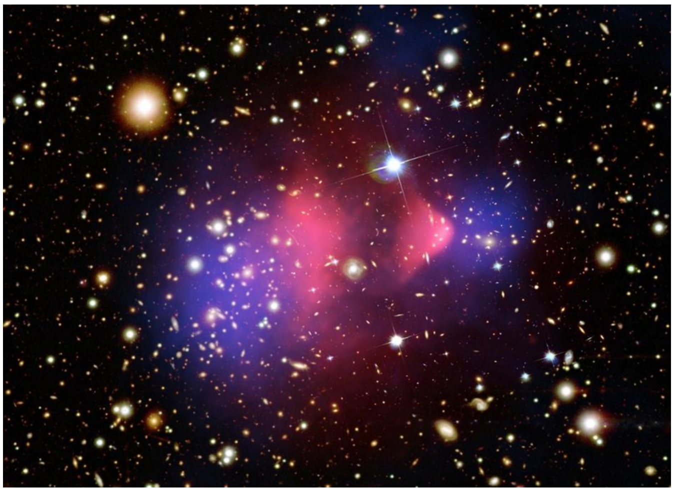

Figure 1.3: A composite image of the Bullet cluster merger. The blue region shows the weak lensing reconstruction of the mass distribution from the lensed images of the galaxies in the background. The pink region shows the X-ray emitting gas. Image courtesy: NASA/CXC/SAO [24].

can be explained if each cluster has an essentially collisionless DM halo dominating its total mass. The baryonic gaseous components of the merging clusters experience drag force while passing through each other. Whereas the DM components of the clusters do not feel substantial drag. As a result, the gaseous component lags behind the DM distribution. This gives an empirical evidence for *collisionless* CDM.

Gravitational lensing of the light from distant galaxies provide independent evidence for DM. The images of galaxies captured by Hubble space telescope and other telescopes show the lensing effect due to some invisible substance in the intermediate region between the source and the observer; the baryonic matter is unable to produce such large effect. Analysis of the lensed images show that such effects can be understood to be caused by gravitational lensing by DM halos [25, 26]. The lensing analysis also provide independent estimates of the amount of total DM in the Universe which is consistent with other analyses [25]. See Ref. [27] for a nice review on this topic.

The mass contained within a certain radius of a galaxy can be estimated by measuring its rotation curve. In most of the galaxies, it is seen that the luminous matter cannot explain the rotation curve [28–31]. If visible stars were the only mass in a galaxy, then one can show from the Kepler's law that the stars' circular velocity would fall as $v(r) \sim r^{-1/2}$ with radius. Whereas in reality, most galaxies show $v(r) \sim$ constant towards the outer radius, implying a 'dark mass' that surrounds the galaxies and contributes 3–10 times that of the visible matter to the total mass.

1.4.2 *Properties*

Several properties of DM can be discerned from the above observations:

- It is *cold*, i. e., nonrelativistic.

  If DM were relativistic, then the particles would have traveled longer distances because of high velocity. Its mean free path would be longer. As a result, all structures at length scales smaller than its mean free path, like the galaxies and dwarf galaxies, would not have formed. The fact that we see such structures around us today tells us that DM has to be nonrelativistic [32, 33]. Also, relativistic DM would affect the matter power spectrum, as well as the CMB angular power spectrum significantly. The earliest evidence of CDM is from the time of recombination. The possibility that DM may have been relativistic during pre-recombination era raises an interesting question about the formation epoch of CDM. We shall discuss more about this in a later chapter.

- It is *dark*, i. e., it does not interact much with the visible particles.

  Several experimental endeavours are currently going on along three main avenues– direct detection, indirect detection, and collider search, to detect any interaction between DM and the Standard Model (SM) particles. Direct detection experiments are looking for scattering between DM particle and the atoms inside a detector in laboratory [34–38]. The indirect detection experiments are trying to detect any annihilation or decay of DM particles into SM particles in various astrophysical objects like galaxies, dwarf galaxies etc [39–43]. DM could be produced in high energy particle collisions at colliders, such as LHC, and would be 'seen' as missing energy. Nonobservation of any such event puts upper limit on DM–SM particle interaction cross section [44–46].

- It is essentially *collisionless*.

> The weak lensing maps of DM halos in several galaxy cluster mergers tell us that DM cannot be strongly self-interacting as it would cause lag between the colliding halos [11, 22, 23]. Comparison of data with DM N-body simulations show that DM of mass m_χ in galaxy clusters must have self-interaction cross section $\sigma/m_\chi \lesssim 0.1\,\mathrm{cm}^2/\mathrm{g}$ [47].

1.4.3 *Thermal dark matter*

A popular candidate for DM is a weakly interacting massive particle (WIMP) that was in thermal equilibrium with other particles at early times, and its relic population forms the DM density in the present Universe. Because it is weakly interacting, it would have the properties of being dark and collisionless. Annihilation into other lighter particles would change its number density n_χ as

$$\frac{1}{a^3}\frac{d(n_\chi a^3)}{dt} = -\langle\sigma v\rangle\left[n_\chi^2 - (n_\chi^{eq})^2\right] , \tag{1.12}$$

where $\langle\sigma v\rangle$ is the thermally averaged cross section for annihilation, and n_χ^{eq} is the equilibrium number density of χ. On the LHS, the number density is multiplied by a^3 to take care of decrease of n_χ just due to the expansion of the spacetime. As the Universe expands, the density becomes too sparse for two DM particles come together and annihilate into other particles. This happens roughly when the annihilation rate $n_\chi\langle\sigma v\rangle$ drops below the Hubble expansion rate $H(t)$. After this, the annihilation process freezes out, and the comoving number density becomes constant. A straightforward calculation yields the final energy density, the relic abundance of χ as

$$\Omega_\chi = \frac{H(m_\chi)x_f T_0^3}{30 m_\chi^2\langle\sigma v\rangle\rho_c} , \tag{1.13}$$

where $H(m_\chi)$ is the Hubble parameter at $T = m_\chi$, $x_f = m_\chi/T_f$, T_f is the freeze-out temperature, and T_0 is the photon temperature today. For $m_\chi = 1$ GeV to 100 TeV, x_f lies within $20-30$. Therefore, WIMP-like DM is always nonrelativistic when its relic abundance is formed. Clearly, the energy density in Eq.(1.13) only decreases as $\sim T_0^3$. A cross section of about $\langle\sigma v\rangle \simeq 2.2\times10^{-26}\,\mathrm{cm}^3/\mathrm{s}$ is needed to thermally produce DM with the correct relic abundance [48].

1.5 SMALL SCALE CHALLENGES TO COLLISIONLESS DARK MATTER

Structure formation with collisionless CDM happens at all length scales. The properties of a large cluster-size DM halo would be similar to a smaller galaxy or dwarf galaxy-size halo. This self-similarity is evident in all N-body simulations run with collisionless CDM all the way down to smallest mass scale resolved. Higher resolution simulations revealed that the individual halo density profile is can be well fitted by the Navarro-Frenk-White (NFW) profile [49]

$$\rho(r) = \frac{\rho_s}{\frac{r}{r_s}\left(1 + \frac{r}{r_s}\right)^2}, \tag{1.14}$$

where ρ_s and r_s are the scale density and scale radius, respectively. This profile was found to be virtually *universal* as it could fit to any DM halo irrespective of its size.

- *Diversity in galaxy density profile*

  However observations at galactic and smaller scales have revealed a few issues with this simple universal picture. The NFW profile a'cuspy' central density, $\rho \sim r^{-\alpha}$ with $\alpha \simeq 1$, as in the NFW profile in Eq.(1.14). The measurements of rotation curves in several low-mass, DM-dominated galaxies show that they instead have shallow 'core' $\alpha = 0 - 0.5$ at the center [50–55]. This is known as *core-vs-cusp issue*. To resolve this discrepancy, hydrodynamic simulations with SPH codes were performed with complex astrophysical processes, such as star formation and supernova explosion. It has been shown that these astrophysical processes can blow away DM from the central region of the halo leading to shallow cores as observed [56, 57].

  A comparison between the MW satellite galaxies and the massive subhalos of MW-size halo in CDM simulations show that the MW satellites systematically have less central density than the subhalos in the simulations [58]. The question here is that if the observed satellite galaxies do not occupy the most massive subhalos of the MW and more massive subhalos exist, then why they have failed to form galaxies. This is known as the *too-big-to-fail problem*. Similar observation has also been made in the satellites of the Andromeda galaxy [59].

  These problems can be thought as two different manifestations of a single *diversity problem*. Galaxies with the same maximum velocity $V_{\max}$ show a wide variety of inner densities. This is shown in Fig. 1.4 where circular velocities $V_{\rm circ}$ at 2 kpc of several galaxies are plotted with their maximum rotation velocity $V_{\max}$ in the horizontal axis. Galaxies with same $V_{\max}$ are hosted by halos of similar mass. Large diversity in circular velocity shows a similar variety in density profile. This observation has not been satisfactorily explained in the paradigm of collisionless CDM. As was pointed out in Ref. [55], it is more prominent for dwarf galaxies. They tend to have lower circular velocities at small radii.

  Efforts have been made to explain this observation from the baryonic feedback near the centers of DM halos using hydrodynamic simulations. Initial efforts have found it difficult to reproduce such a diverse set of density profiles [55]. However, Ref.[56] have used an improved

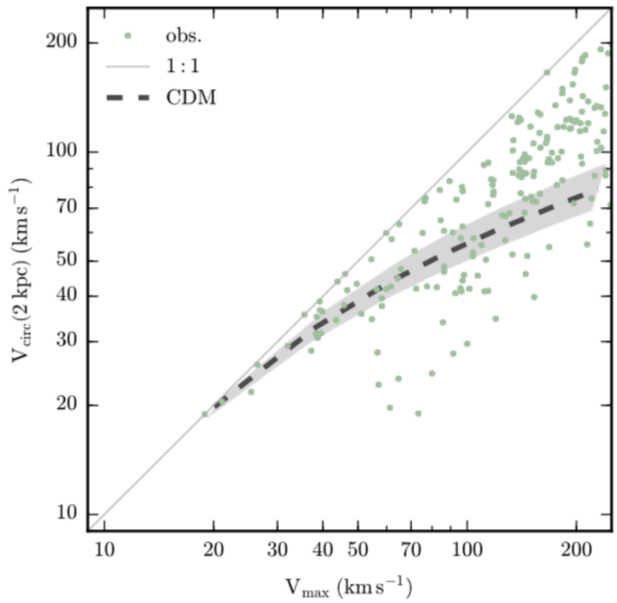

Figure 1.4: Circular velocity at 2 kpc radius of galaxies are plotted with their maximum velocity V_{max}, a tracer for the total mass of the DM halo. The galaxies show a wide diversity even for a single V_{max}. This figure is reproduced from Ref. [60].

version of SPH (Smoothed Particle Hydrodynamics) code to show that the shape of inner density profile changes over time as the halo accrete more mass. The final shape depends on the ratio of stellar to DM mass in the halo, and hence can exhibit a varied inner slope of density profile.

However, it is not completely clear if these problems can be entirely resolved by modelling the complex baryonic physics in simulations more carefully as there are contradictory claims from different groups of researchers. For example, the authors in Ref. [61] did not obtain cores in dwarf galaxy simulations, but were able to solve the too-big-to-fail problem. Also, several dwarfs have been observed to have steeper inner density slopes, such as NGC5963 ($\alpha = 1.28$), NGC6689 ($\alpha = 0.8$), NGC5949 ($\alpha = 0.88$), NGC4605 ($\alpha = 0.88$) [62]. Therefore it is worthwhile to explore other avenues to address these issues. In fact, one of the first proposed solutions to the core-vs-cusp problem involves self-interacting DM particles, which forms the topic of the next chapter.

- *Missing satellites of the Milky Way*

  We see fewer satellite galaxies around the MW than we expect to see according to CDM simulations [63, 64]. There are only ~ 50 known galaxies in the vicinity of the MW, whereas the simulations predict $\mathcal{O}(1000)$ satellite galaxies for a DM halo of MW mass that should have hosted galaxies in them.

Warm dark matter, (partially) acoustic dark matter (DM interacting with a relativistic species, dubbed *dark radiation*) etc. have been put forward as answer to the question of missing satellites. In these models, structure below a certain length scale is washed out due to free streaming of DM or diffusion of relativistic particles. For example, in case of warm dark matter the free streaming length scale is inversely proportional to its mass [65]

$$\lambda_{\rm fs} = 33 \left(\frac{m_\chi}{1\ {\rm keV}}\right)^{-1.11}\ {\rm kpc} \tag{1.15}$$

which corresponds to a mass

$$M_{\rm fs} = 2\times 10^7 \left(\frac{m_\chi}{1\ {\rm keV}}\right)^{-3.33} M_\odot\,. \tag{1.16}$$

This suppression of DM structure below a certain mass scale is known as the collisionless damping. Collisional damping can also suppress structure at small scales if the DM particles interacted with dark radiation at early times. In this scenario, the relativistic particles diffuse out of the overdense DM regions, erasing out structures at length scales shorter than its mean free path

$$\lambda^2_{\rm mfp} = \int_0^{t_{\rm dec}} dt \frac{1}{a^2(t)\Gamma(t)} \tag{1.17}$$

where Γ is the scattering rate and $t_{\rm dec}$ is the time of decoupling. It is also known as the Silk damping.

However it has also been shown that if proper completeness factor of the SDSS galaxy survey and the spatial distribution of the satellites of the MW are taken into account, then the collisionless CDM prediction could be consistent with the observations [66].

The interested reader is suggested to refer to the reviews in Refs.[60, 67, 68] for more detailed discussions about small scale problems.

2 SELF-INTERACTING DARK SECTOR

In this chapter, we shall describe a solution to the small scale problems using beyond collisionless CDM scenario, discuss the general aspects of such models with an emphasis on its late-time phenomenology.

2.1 MOTIVATION

Several 'beyond-standard' collisionless CDM models have been proposed to address the small scale challenges to ΛCDM discussed in the previous chapter. Self-interacting dark matter (SIDM) model is one of them.

In the ΛCDM paradigm, the DM particles are assumed to be perfectly collisionless. They interact only via gravity. On the other hand, SIDM models predict that the DM particles have *secret interactions* among themselves. For local DM density n_χ and self-scattering cross section σ, the mean free path would be $\lambda_{\rm mfp} = 1/(n_\chi \sigma)$. As we do not know the mass of the DM particle, it is customary to express the mean free path as $m_\chi/(\rho\sigma)$, and quantify the strength of the self-scattering in terms of σ/m_χ. Ref. [69] first suggested the idea of SIDM. Similar to collisionless CDM, the SIDM particles start forming clumps under the influence of gravity and start forming halos. At the initial stage of structure formation, the number density is not large enough for the nongravitational self-interaction to have any effect. After forming halos, at the center the density shoots up as more and more DM particles fall towards the center. When the mean free path becomes smaller than the typical size of a halo, the particles start undergoing collisions. As a result, SIDM can transport 'heat' or kinetic energy from hotter inner region to the relatively colder outer part through scattering. Eventually the particles at the center come to equilibrium and form an isothermal core.

Core-formation in dwarf galaxies have been confirmed by several N-body simulations. It has been found that a DM self-scattering cross section $\sigma/m_\chi \simeq 0.5 - 50\,\mathrm{cm}^2/\mathrm{g}$ can alleviate the core-cusp and the too-big-to-fail problems [70–73]. On the other hand, the galaxy cluster merger observations put an upper limit on this cross section $\sigma/m_\chi \lesssim 0.1\,\mathrm{cm}^2/\mathrm{g}$ [47]. Therefore, to simultaneously solve the small scale problems and satisfy the constraint from galaxy cluster mergers, a velocity-dependent scattering cross section is needed, i. e., $\sigma/m_\chi \simeq 1\,\mathrm{cm}^2/\mathrm{g}$ at velocity $v \sim 10\,\mathrm{km/s}$ in dwarf galaxies to $\sigma/m_\chi \lesssim 0.1\,\mathrm{cm}^2/\mathrm{g}$ at velocity $v \sim 1000\,\mathrm{km/s}$ in galaxy clusters. Recently, Ref. [74] have found that the diversity in the galactic rotation curves can be explained in the SIDM framework. A DM self-scattering cross section $\sigma/m_\chi = 3\,\mathrm{cm}^2/\mathrm{g}$ has been shown to be able to explain the density profiles of two dwarf galaxies, namely Draco and Fornax, with very different central densities [75]. The core-collapse of DM halo due to self-scattering and tidal interaction with the MW potential plays a key role here. Therefore the observed diversity in the density profiles of dwarf galaxies could very well be a result of a complex interaction between several effects, like baryonic feedback, DM self-scattering, tidal field of MW etc.

Strong constraint from direct detection experiments also motivates us to consider theories with additional light particles residing in the dark sector that interacts with the DM. Currently, direct detection experiments constrain the DM-visible sector interaction to such a small value which would imply overabundance of thermal DM. If other light particles are present in the dark sector, then during relic abundance formation, DM would annihilate into these particles, and could yield the correct relic abundance, without running into problems with the direct detection bound. At the same time, such models can also successfully address the small scale problems [76–78]. From the particle physics perspective as well, it is natural to expect that the dark sector contains more than just one particle. Very often the DM is predicted to be the lightest state of a multiplet of some gauge symmetry. One such example is the minimally supersymmetric SM. In these models, DM is naturally accompanied by its heavier 'cousins', as well as gauge particles mediating interactions.

Numerous particle physics models have been proposed with interactions between DM particles [76, 79–96]. Models with light force mediators are of special interest. For example, if the DM is charged under a gauge symmetry that is spontaneously broken, then it can become stable because of charge conservation. The gauge boson mediates the self-interaction. For global symmetries, a scalar can also mediate the interaction. A few possible interactions between the DM χ and the mediators A^μ or ϕ are given below–

$$\begin{aligned} \mathcal{L} \;&\supset\; gA^\mu\bar{\chi}\gamma_\mu\chi\,, && \text{Vector} \\ &\supset\; gA^\mu\bar{\chi}\gamma_\mu\gamma_5\chi\,, && \text{Pseudovector} \\ &\supset\; y\phi\bar{\chi}\chi\,, && \text{Scalar} \\ &\supset\; y\phi\bar{\chi}\gamma_5\chi\,, && \text{Pseudoscalar} \end{aligned} \tag{2.1}$$

In Chs. 3 and 4, we shall discuss the novel phenomenologies of self-interacting DM models.

The CMB experiment data tells us that the dark sector is collisionless at least since the time of recombination. However, we do not have any clue about the exact time when it became collisionless. The other epoch prior to recombination which we can probe is the time of BBN, but because the Universe was radiation dominated at that time we cannot tell anything about the existence of collisionless DM. Therefore, it is very much possible that the dark sector was a tightly-coupled collisional fluid until redshift $z \sim 10^4$. In fact, most of the DM models predict that DM was relativistic and collisional at early times. This motivates us to investigate the effects of late-forming cold collisionless dark matter on various cosmological observables. We shall discuss more about this in Ch. 5.

In the rest of this chapter, we discuss the interesting phenomenology of such models.

2.2 NONRELATIVISTIC FIELD THEORY

Today DM particles are nonrelativistic (NR), and their velocity dispersion varies over 2–3 orders of magnitude between astrophysical objects of different size. Galaxy clusters have the largest velocity dispersion $v \sim \mathcal{O}(1000 \text{ km/s})$. MW-like galaxies, $v \sim \mathcal{O}(100 \text{ km/s})$ and dwarf galaxies, $v \sim \mathcal{O}(10 \text{ km/s})$ have smaller velocities. Therefore it is suggestive to take the NR limit of the DM model to study its late time phenomenology.

This is done using the formalism of Nonrelativistic Effective Field Theory (NREFT). We shall give an example of this using NR electron-positron in quantum electrodynamics.

2.2.1 *Nonrelativistic quantum electrodynamics*

Let us consider the electrons and positrons interacting with each other through photons. The Lagrangian of this system is given by

$$\mathcal{L} = \bar{\psi}_e(i\partial\!\!\!/ - m_e)\psi_e - gA^\mu\bar{\psi}_e\gamma_\mu\psi_e - \frac{1}{4}F^{\mu\nu}F_{\mu\nu} \tag{2.2}$$

where $F_{\mu\nu} = \partial_\mu A_\nu - \partial_\nu A_\mu$. Moreover, let us assume that the electrons and positrons are NR, such that their kinetic energy is

$$E \simeq m_e + \frac{1}{2}m_e v^2\,. \tag{2.3}$$

In this limit, it is advantageous to use the two-component spinor notation for the Dirac fermion corresponding to electron and positron. Thus we write

$$u^r(\mathbf{p}) = \sqrt{\frac{E+m_e}{2E}}\begin{pmatrix} \xi^r \\ \dfrac{\boldsymbol{\sigma}\cdot\mathbf{p}}{E+m_e}\xi^r \end{pmatrix}\,,\quad v^r(\mathbf{p}) = \sqrt{\frac{E+m_e}{2E}}\begin{pmatrix} \dfrac{\boldsymbol{\sigma}\cdot\mathbf{p}}{E+m_e}\eta^r \\ \eta^r \end{pmatrix}\,. \tag{2.4}$$

Here r, s are the spin indices, and $|\mathbf{p}|/m_e = v$.

In the nonrelativistic limit, typical momentum exchange is much below the scale of the mass m_e of the NR electron. The momentum exchange is of order $\sim m_e v$, $m_e v^2$ etc., and hence, are *long range*. Short range processes of distance scale $\sim 1/m_e$ are described by the higher dimensional effective operators. The Lagrangian consists of the following three parts,

$$\mathcal{L} = \mathcal{L}_{\text{kin}} + \mathcal{L}_{\text{pot}} + \mathcal{L}_{\text{ann}} + \dots\,. \tag{2.5}$$

Here $\mathcal{L}_{\text{kin}}$ is the kinetic energy part and involves its NR form

$$\mathcal{L}_{\text{kin}} = \xi^\dagger\left(i\partial_t + \frac{\boldsymbol{\nabla}^2}{2m_e}\right)\xi + \eta^\dagger\left(i\partial_t + \frac{\boldsymbol{\nabla}^2}{2m_e}\right)\eta\,. \tag{2.6}$$

It is straightforward to derive this starting from Eq.(2.2) and (2.4) and neglecting all terms $\mathcal{O}((|\mathbf{p}|/m_e)^3)$.

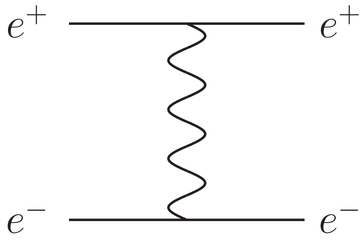

Figure 2.1: A virtual photon exchange between a pair of electron and positron.

The second part $\mathcal{L}_{\rm pot}$ contains the long range interaction potential between two particles which arises from nonlocal interaction typical to any NREFT,

$$\mathcal{L}_{\rm pot} = -\sum_{\chi=\xi,\eta} \int d^3r\, (\chi_i\chi_j)^\dagger V_{ijkl}\, \chi_k\chi_l \tag{2.7}$$

where χ_i stands for the spinors ξ and η, and $V_{ijkl}(r)$ represents the interaction potential between the two-body states $\chi_i\chi_j$ and $\chi_k\chi_l$. The form of the potential can be derived from a single photon exchange graph. One such example for a pair of electron and positron is shown in Fig. 2.1. In momentum space, its amplitude reads

$$\begin{aligned} i\mathcal{M} &= \bar{u}^r(\mathbf{p})(-ig\gamma^\mu)u^s(\mathbf{p}')\frac{-ig_{\mu\nu}}{q^2+i\epsilon}\bar{v}^m(\mathbf{k})(ig\gamma^\nu)v^n(\mathbf{k}')\,, \\ &= -ig^2\bar{u}^r\gamma^\mu u^s\frac{1}{q^2+i\epsilon}\bar{v}^m(ig\gamma_\mu)v^n\,. \end{aligned} \tag{2.8}$$

Here $q = p' - p = k - k'$. We approximate $q^2 \simeq \mathbf{q}^2 = (\mathbf{p}-\mathbf{p}')^2$ neglecting the kinetic energies ($\sim \mathcal{O}(m_e v^2)$) of the NR particles. For the spinors, it can easily be checked that in the NR limit

$$\begin{aligned} \bar{u}^r(\mathbf{p})\gamma^0 u^s(\mathbf{p}') &= \left[1 - \frac{1}{8m_e^2}(\mathbf{p}^2+\mathbf{p}'^2) + \frac{\mathbf{p}\cdot\mathbf{p}'}{4m_e^2}\right]\xi^{r\dagger}\xi^s\,, \\ \bar{u}^r(\mathbf{p})\gamma^i u^s(\mathbf{p}') &= \frac{1}{2m_e}\left[(\mathbf{p}+\mathbf{p}')^i\xi^{r\dagger}\xi^s + i\xi^{r\dagger}((\mathbf{p}-\mathbf{p}')\times\boldsymbol{\sigma})^i\xi^s\right]\,, \\ \bar{v}^r(\mathbf{p})\gamma^0 v^s(\mathbf{p}') &= \left[1 - \frac{1}{8m_e^2}(\mathbf{p}^2+\mathbf{p}'^2) + \frac{\mathbf{p}\cdot\mathbf{p}'}{4m_e^2}\right]\eta^{r\dagger}\eta^s\,, \\ \bar{v}^r(\mathbf{p})\gamma^i v^s(\mathbf{p}') &= \frac{1}{2m_e}\left[(\mathbf{p}+\mathbf{p}')^i\eta^{r\dagger}\eta^s + i\eta^{r\dagger}((\mathbf{p}-\mathbf{p}')\times\boldsymbol{\sigma})^i\eta^s\right]\,. \end{aligned} \tag{2.9}$$

Therefore at the leading order, we can write Eq.(2.8) as

$$i\mathcal{M} = \frac{-ig^2}{\mathbf{q}^2+i\epsilon}(\xi^{r\dagger}\xi^s)(\eta^{m\dagger}\eta^n)\,. \tag{2.10}$$

This amplitude is to be compared with the Born amplitude of scattering in a potential $V(\mathbf{q})$ in the NR limit [97],

$$\langle\mathbf{p}'|iT|\mathbf{p}\rangle = -iV(\mathbf{p}'-\mathbf{p})\,2\pi\delta(E_{\mathbf{p}'}-E_{\mathbf{p}})\,. \tag{2.11}$$

The comparison yields

$$V(\mathbf{q}) = \frac{-g^2}{\mathbf{q}^2+i\epsilon}\,, \tag{2.12}$$

which after taking a Fourier transform reads

$$V(r) = -\frac{g^2}{4\pi r} = -\frac{\alpha}{r}\,. \tag{2.13}$$

Here the fine structure constant α is defined as $\alpha = g^2/4\pi$. This represents an attractive Coulomb potential acting between the oppositely charged electron and positron.

One can repeat a similar exercise for two electrons and two positrons. In both cases, it is a repulsive Coulomb potential. It means that charged particles experience *long range* interaction potential $V(r)$, and it is more pronounced when the particles are NR. It is a manifestation of the exchange of infinite number of virtual photons between the particles [98]. Looking at the kinetic $\mathcal{L}_{\mathrm{kin}}$ and the potential $\mathcal{L}_{\mathrm{pot}}$ parts of the Lagrangian, it is not difficult to see that the equation of motion of the NR fields is given by a Schrödinger equation with the potential $V(r)$,

$$\left[-\frac{1}{2\mu}\boldsymbol{\nabla}^2 + V(\mathbf{r}) - E\right]\Psi(\mathbf{r}) = 0\,. \tag{2.14}$$

Here $\Psi(\mathbf{r})$ is the wavefunction, μ is the reduced mass, and E is the total energy of the particles in the center-of-mass frame which, for the scattering state, reads $E = \mu v_{\mathrm{rel}}^2/2$ with v_{rel} being the relative velocity between the particles.

In passing, we mention that if the mediator of the interaction were massive with a mass m_ϕ, then Eq.(2.13) becomes the Yukawa potential

$$V(r) = -\frac{\alpha\, e^{-m_\phi r}}{r}\,. \tag{2.15}$$

Unlike Coulomb, this potential is exponentially screened beyond a distance $\sim 1/m_\phi$. For a Yukawa interaction between a scalar and a fermion, potential is again the same except that it is always attractive.

Eq.(2.14) describes the evolution of the NR particles under the influence of a potential $V(r)$, but it does not contain any information about the annihilation of electron and positron. The last term in Eq.(2.5) contains this information through higher dimensional four-Fermi operators. As mentioned before, we cannot draw any Feynman graph with photons in the external leg. They can appear only as internal propagators. Such operators are included in the $\mathcal{L}_{\mathrm{ann}}$ term in Eq.(2.5). Cutkosky theorem tells us that the annihilation of a pair of electron and positron into two photons can be represented as the imaginary or absorptive part of the Wilson coefficients of these four-Fermi operators. Suppose, S is the scattering matrix of a process with a transition matrix T,

$$S = 1 - iT\,. \tag{2.16}$$

The unitarity property of S implies

$$\langle a|T^\dagger T|a\rangle = i\langle a|(T - T^\dagger)|a\rangle\,, \tag{2.17}$$

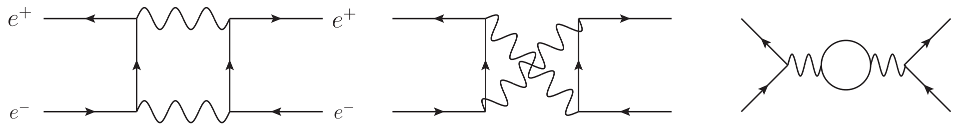

Figure 2.2: One-loop graphs that contribute to the four-Fermi operator $\chi^\dagger_{e^+}\chi_{e^-}\chi^\dagger_{e^+}\chi_{e^-}$ in NRQED.

for a general state $|a\rangle$. Now using the completeness of the states $\sum_{|f\rangle}|f\rangle\langle f| = 1$ on LHS gives

$$\sum_{|f\rangle}\langle a|T^\dagger|f\rangle\langle f|T|a\rangle = 2i\ \mathrm{Im}\left(\langle a|T|a\rangle\right) . \tag{2.18}$$

This equation tells us that the cross section of the process $|a\rangle \to |f\rangle$ is proportional to the imaginary part of the amplitude $\langle a|T|a\rangle$.

The general form of $\mathcal{L}_{\mathrm{ann}}$ is

$$\mathcal{L}_{\mathrm{ann}} = \sum_{i,j,k,l}\frac{c_{ij,kl}\left({}^{2s+1}\ell_J\right)}{m_e^2}\mathcal{O}_{ij,kl}\left({}^{2s+1}\ell_J\right), \tag{2.19}$$

where $\mathcal{O}_{ij,kl}\left({}^{2s+1}\ell_J\right)$ are the four-Fermi operators $\chi_i^\dagger\chi_j\chi_k^\dagger\chi_l$, and $c_{ij,kl}\left({}^{2s+1}\ell_J\right)$ are the respective Wilson coefficients. We have classified the operators according to their spin s and angular momentum ℓ. The Wilson coefficients are obtained by matching the corresponding four-point function in full theory with the operator $\mathcal{O}_{ij,kl}\left({}^{2s+1}\ell_J\right)$. The leading order contribution to $c_{ij,kl}\left({}^{2s+1}\ell_J\right)$ comes from the one-loop graph of the four-point function.

For annihilation of electron and positron, the first two graphs in Fig. 2.2 are relevant[1]. The two graphs correspond to the t and u-channels, respectively. After a long but straightforward calculation, we find

$$\mathrm{Im}(c({}^1S_0)) = \pi\alpha^2 . \tag{2.20}$$

This formalism is useful for any NR particles interacting with each other through a lighter particle. We shall use this extensively in the later chapters while discussing about the annihilation and scattering of NR DM particles.

2.3 PHENOMENOLOGIES & SIGNATURES

2.3.1 *Sommerfeld effect*

SIDM models with light mediators show large enhancement/suppression of DM annihilation rate through Sommerfeld effect. Arnold Sommerfeld first calculated this effect for electron-positron annihilation in 1931 [99]. When two particles experience a long range interaction prior to their annihilation, their wavefunctions are modified. In the absence of any potential, the incoming particles are described by plane waves with constant amplitude. An attractive potential 'pulls' the particles towards each other, and

1 The third graph has a fermion loop in the middle. Hence, it is not relevant for e^+e^- annihilation.

hence, distorts the wavefunctions from plane waves. A repulsive potential shows the opposite effect. This is known as the *Sommerfeld effect*. In the NR regime, Feynman graphs with more number of loops do not acquire higher powers of coupling making the theory nonperturbative.

In NREFT, typical momentum exchange between the NR particles is of the order of Bohr momentum, and hence scales as $|\mathbf{p}| \sim \alpha m_\chi$. For example in NRQED, typical photon momentum is $\sim \alpha m_e$, and the kinetic energy of electrons and positrons is $|\mathbf{p}|^2/m_e \sim \alpha^2 m_e$. While computing a loop momentum integral in NREFT, we need to keep these α-scalings in mind.

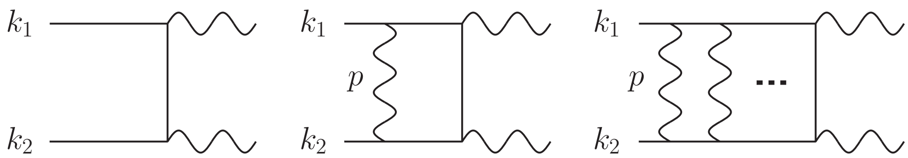

Figure 2.3: Each successive graph with an additional photon propagator always scales with the coupling as $1/\alpha$. Hence the whole ladder diagram with infinite number of terms needs to to be evaluated.

Now, let us estimate the α-scaling of the e^+e^- annihilation graphs shown in Fig. 2.3. The first graph is the tree level graph. The second graphs has one extra photon and two fermion propagators. It scales as $\sim \alpha \cdot \alpha^{-2} \sim \alpha^{-1}$. In the third graph, the additional factor coming from the loop is

$$\int d^4p \frac{i}{p^2 + i\epsilon} \cdot \frac{1}{\not{k}_1 - \not{p} + m_e + i\epsilon} \cdot \frac{1}{\not{k}_2 + \not{p} - m_e + i\epsilon} \,. \tag{2.21}$$

The photon propagator contributes a factor of α^{-2}, the electron and positron propagators are offshell by an amount $\sim |\mathbf{p}|^2/m_e$, thus each of them gives α^{-2}. The integration measure gives $\alpha^2 \cdot \alpha^3$. Putting all together yields $\alpha^5 \cdot \alpha^{-4} \cdot \alpha^{-2} \cdot \alpha^{-2} \cdot \alpha^2 \sim \alpha^{-1}$. Therefore, as we keep adding more and more photon lines between the annihilating pair of electron and positron, the α-scaling remains the same and those graphs contribute at the same order of α as the one-photon exchange graph. As a result, a perturbative expansion in powers of α is not possible. One needs to sum over all such graphs in Fig. 2.3 up to infinite number of rungs. Techniques like Bethe-Salpeter equation needs to be invoked to compute such diagrams.

Sommerfeld effect was included in DM annihilation calculation as early as in 2002 [100–105]. Later it was invoked to explain the positron excess in the cosmic rays seen by a host of experiments, such as PAMELA, Fermi-LAT, MASS, Wizard/CAPRICE, AMS-01, and HEAT [106–110]. For DM annihilation to account for this excess, the annihilation cross section needs to be significantly larger than its thermal relic value $\sigma v \simeq 2 - 3 \times 10^{-26}\,\text{cm}^3/\text{s}$. Sommerfeld enhancement provides a way to achieve such large cross section when the DM particles are nonrelativistic at late time, without changing the relic cross section.

Sommerfeld effect is quantified as the relative change in the wavefunction at the point $\mathbf{r} = 0$ of annihilation,

$$S = \frac{|\Psi(0)|^2}{|\Psi_0(0)|^2} \,. \tag{2.22}$$

Here, $\Psi_0(\mathbf{r})$ is the wavefunction of the free particles in the absence of any potential. The difference in the length scales between the long range potential and the actual annihilation allows us to factorize these two processes, such that the net annihilation cross section σ is given by

$$\sigma = S\sigma_0 \,, \tag{2.23}$$

where σ_0 is the cross section without any Sommerfeld effect.

We need to solve the Schrödinger equation in Eq.(2.14) in scattering state to find the Sommerfeld factor. In most of the cases of our interest, the potential is rotationally symmetric. Therefore, we can expand $\Psi(\mathbf{r})$ in the partial wave basis as

$$\Psi(\mathbf{r}) = \sum_\ell A_\ell P_\ell(\cos\theta) R_{k\ell}(r) \,. \tag{2.24}$$

Here $P_\ell(\cos\theta)$ are the Legendre polynomials, $R_{k\ell}(r)$ are the radial wavefunctions, $k = \mu v_{\rm rel}$ is the momentum, and A_ℓ are the coefficients for each partial wave. The radial wavefunctions are redefined as

$$R_{k\ell} = \frac{u_\ell(r)}{r} \,, \tag{2.25}$$

and the equation for $u_\ell(r)$ becomes

$$-\frac{1}{2\mu}\frac{d^2u_\ell}{dr^2} + \left(\frac{\ell(\ell+1)}{2\mu r^2} + V(r) - E\right) u_\ell = 0 \,. \tag{2.26}$$

The asymptotic $\Psi(\mathbf{r})$ at large r is matched with the following

$$\Psi(\mathbf{r}) \overset{r\to\infty}{\longrightarrow} e^{-ikz} + f(\theta)e^{ikr} \,, \tag{2.27}$$

with $f(\theta)$ being the scattering amplitude. Therefore, the Sommerfeld factor S becomes

$$S = \left|\frac{1}{k}R_{k0}(0)\right|^2 = \left|\frac{1}{k}\frac{du_0(0)}{dr}\right|^2 \,. \tag{2.28}$$

For Coulomb potential (Eq.(2.13)), an analytic form of S_0 for $\ell = 0$ is given as [99, 111]

$$S_0 = \frac{\pi\alpha/v}{1 - \exp(-\pi\alpha/v)} \,. \tag{2.29}$$

This factor goes to unity, $S \to 1$ in the large velocity limit $v \simeq 1$ which is expected in the relativistic limit. It grows as $\sim 1/v$ for small velocities. Higher partial wave Sommerfeld factors for Coulomb potential was derived in Ref. [98],

$$S_\ell = S_0 \prod_{n=1}^{\ell} \left(1 + \frac{1}{4n^2}\frac{\alpha^2}{v^2}\right) \,. \tag{2.30}$$

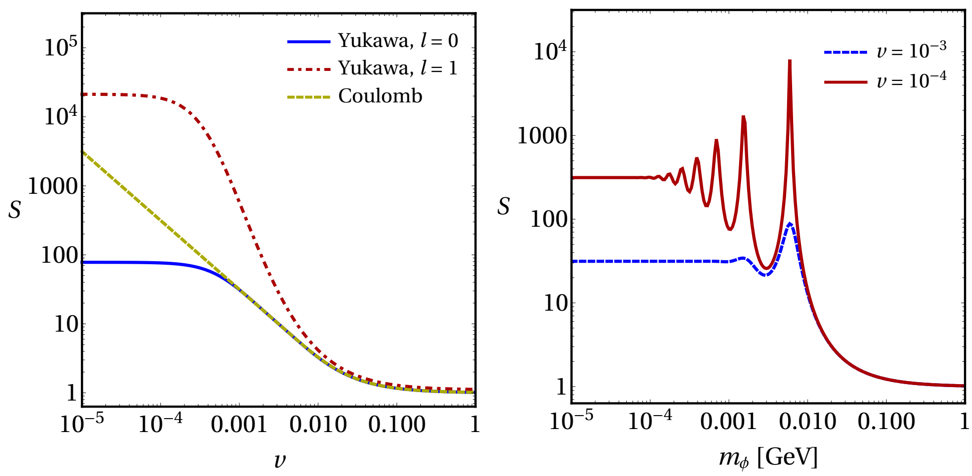

Figure 2.4: (Left) Sommerfeld factors for Yukawa potential, $\ell = 0$ (solid blue), $\ell = 1$ (dot-dashed red), and for Coulomb potential (dashed yellow). Note the different velocity dependence of the partial waves. The parameters are: coupling $\alpha = 0.01$, DM mass $m_\chi = 1$ GeV, and mediator mass $m_\phi = 1$ MeV. (Right) Variation of the Sommerfeld factor for $\ell = 0$ the Yukawa potential with velocities $v = 10^{-3}$ (dashed blue) and $v = 10^{-4}$ (solid red). Other parameters are: $\alpha - 0.01$, $m_\chi = 1$ GeV.

In the small velocity limit, the Sommerfeld factor for ℓ-th partial wave grows as $\sim 1/v^{2\ell+1}$.

For Yukawa potential, a closed form analytic solution for S_ℓ is not feasible. However, Yukawa potential can be replaced with the Hulthén potential

$$V_H(r) = \frac{\alpha m_* e^{-m_* r}}{1 - e^{-m_* r}}, \tag{2.31}$$

with $m_* = \pi^2 m_\phi/6$, for which analytic solution is possible [98]. In the left panel of Fig. 2.4, we show the velocity dependence of the Sommerfeld factors for both Coulomb and Yukawa potentials. Various partial waves have different behaviour in the small velocity limit. The main difference between the two potentials is that the factor for Coulomb potential keeps increasing as the velocity gets smaller and smaller without any bound. This is result of the infinite range of the Coulomb potential. On the other hand, the Yukawa potential has a finite range $\simeq 1/m_\phi$. When the de Broglie wavelength of the particle gets larger than the range of the potential, i. e., when $k \ll m_\phi$, the particles stop 'seeing' the potential, and the Sommerfeld factor saturates to a constant value as can be seen in Fig. 2.4.

In the right panel of Fig. 2.4, we show the variation of the $\ell = 0$ Sommerfeld factor with the mediator mass m_ϕ. The important feature in this figure is the appearance of the resonances at certain values of m_ϕ. The resonances are the result of the formation of virtual (zero energy) bound states between the DM particles. The attractive Yukawa potential has a finite number of negative energy bound states. Even though the annihilating DM particles are in the positive energy state ($E > 0$ at infinite distance), the bound state energy levels below $E = 0$ can enhance the wavefunction near the annihilation point. This gives rise to the large enhancements seen in the right panel of Fig. 2.4. The resonance positions are given by [98]

$$\frac{\alpha m_\chi}{\kappa m_\phi} = n^2, \qquad n = 1, 2, 3, \dots , \tag{2.32}$$

where $\kappa = \pi^2/6$. See the Chapter XVII in Ref. [97] for more discussion on resonances in zero energy scattering.

2.3.2 *Self-scattering*

DM self-scattering is inevitable in the models where self-interaction between DM particles (Eq.(2.1)) is present that causes the Sommerfeld enhancement. Ref. [86] first computed this cross section in a DM model. Later on, DM scattering with light mediator has been extensively used to achieve a unique velocity-dependent cross section that can yield a large enough cross section to solve the core-vs-cusp problem as well as satisfy the upper limit from the Bullet cluster observation.

The scattering cross section can be calculated again by solving the Schrödinger equation Eq.(2.26). However in this case, we need to solve this equation for many partial waves ℓ to find the phase shift δ_ℓ defined as [97]

$$f(\theta) = \frac{1}{2ik} \sum_{\ell=0}^{\infty} (2\ell + 1) P_\ell(\cos\theta) e^{2i\delta_\ell} , \tag{2.33}$$

where $f(\theta)$ is the scattering amplitude defined in Eq.(2.27). The total cross section σ_{tot} is defined as

$$\sigma_{\text{tot}} = \int |f(\theta)|^2 d\Omega = \int \frac{d\sigma}{d\Omega} d\Omega . \tag{2.34}$$

Substituting Eq.(2.33) in Eq.(2.34) and using the orthogonality of $P_\ell(\cos\theta)$ yields

$$\sigma_{\text{tot}} = \frac{4\pi}{k^2} \sum_{\ell=0}^{\infty} (2\ell + 1) \sin^2 \delta_\ell . \tag{2.35}$$

Even though the sum continues ad infinitum, for all practical purpose it can be truncated at a finite max such that

$$\ell_{\text{max}} \simeq \frac{k}{m_\phi} . \tag{2.36}$$

The phase shifts from higher partial waves are negligible because the 'impact parameter' $\sim \ell/k$ for the partial wave ℓ becomes larger than the range of the potential $\sim 1/m_\phi$. We follow the numerical procedure illustrated in Ref. [112] to compute the cross section.

If the mediator is light, then the differential cross section $d\sigma/d\Omega$ has a divergence in the forward direction, $\theta \simeq 0$. It means large scattering probability but with small momentum transfer. To mitigate this, alternative definitions, like transfer and viscosity cross sections are used. Transfer cross section is defined as

$$\sigma_{\text{T}} = \int \frac{d\sigma}{d\Omega} (1 - \cos\theta) d\Omega . \tag{2.37}$$

The weight factor $(1 - \cos\theta)$ removes all contribution from the forward divergence. Viscosity cross section is defined as

$$\sigma_{\rm V} = \int \frac{d\sigma}{d\Omega} \sin^2\theta d\Omega \,. \tag{2.38}$$

These alternative definitions are specially important for N-body simulations of SIDM particles. Large forward scattering is inconsequential for such simulations as the final state is the same as the initial state if the DM particles are identical.

In Fig. 2.5, we show the variation of σ/m_χ with the mediator mass and DM velocity. To understand the dependence of the cross section on different parameters, let us take the Born limit $\alpha M/m_\phi \ll 1$. In this limit, the potential essentially becomes a *short range* contact interaction, and the cross section can be computed analytically [81],

$$\sigma_{\rm T}^{\rm Born} = \frac{2\pi\beta^2}{m_\rho^2}\left[\ln\left(1+R^2\right) - \frac{R^2}{1+R^2}\right] \,. \tag{2.39}$$

Here, $\beta = 2\alpha m_\phi/(m_\chi v_{\rm rel}^2)$, and $R = m_\chi v_{\rm rel}/m_\phi$. For large velocity, the approximate value is $\sigma_{\rm T}^{\rm Born} \simeq \dfrac{8\pi\alpha^2}{m_\chi^2 v_{\rm rel}^4}(\ln R^2 - 1)$. In this limit, the de Broglie wavelength of the scattering particles becomes much smaller compared to the range of the potential where it is Coulomb-like, and the cross section goes as $\sim 1/v^4$ as in Rutherford scattering. In the low velocity limit ($R \ll 1$), only the s-wave scattering is important, and the cross section saturates to a constant value. The limiting form of the transfer cross section is $\sigma_{\rm T}^{\rm Born} \simeq 4\pi\alpha^2 m_\chi^2/m_\phi^4$. These features are evident in Fig. 2.5. Thus it shows that light mediator DM models are capable of achieving large self-scattering cross section in the dwarf galaxies and smaller value in the galaxy clusters, as was mentioned in Sec. 2.1. Away from the Born region, for smaller values of m_ϕ, zero energy resonances from virtual bound state formation (see Eq.(2.32)) results in large cross section for certain values of m_ϕ. Therefore, scattering resonances appear at the same places as in the case of annihilation.

In addition to the resonances, we note the appearance of *anti-resonances* between the resonances. They are the result of the Ramsauer-Townsend effect when the low energy s-wave phase shift δ_0 becomes integer multiples of π [113].

2.3.3 *Extra relativistic degrees of freedom*

SIDM models generically predict light particles in addition to the DM particle. They contribute to the total radiation energy density in the early Universe when it was radiation dominated. The extra relativistic degrees of freedom is parameterized as the *effective number of thermal neutrinos* $N_{\rm eff}$,

$$N_{\rm eff} = \frac{\sum \rho_{\nu_i}}{\rho_\nu^{\rm FD}} + \frac{\rho_{\rm DR}}{\rho_\nu^{\rm FD}} \tag{2.40}$$

$$\equiv N_{\rm eff}^{\rm SM} + \Delta N_{\rm eff} \,. \tag{2.41}$$

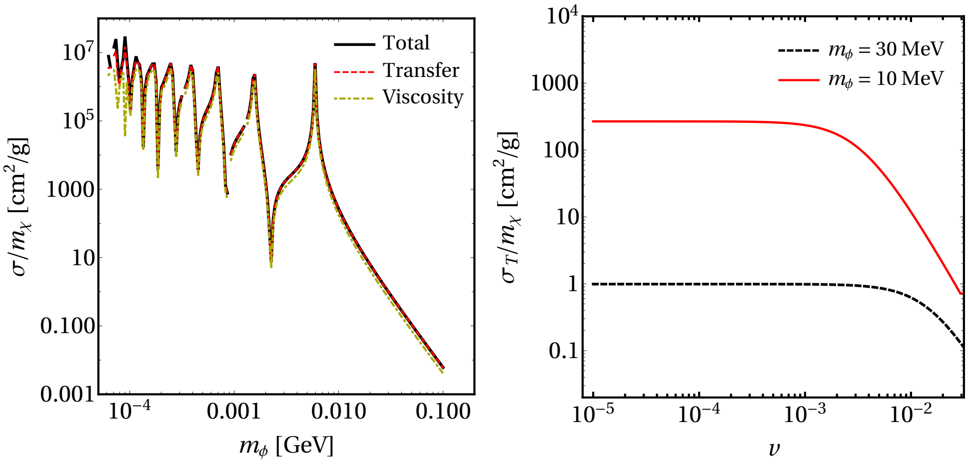

Figure 2.5: (Left) Three types of self-scattering cross section $\sigma_{\text{tot}}/m_\chi$, σ_{T}/m_χ, and σ_{V}/m_χ as a function of the mediator mass m_ϕ. (Right) The transfer cross section σ_{T}/m_χ as a function of DM velocity for two mediator mass, $m_\phi = 10,\ 30$ MeV, and DM mass $m_\chi = 1$ GeV.

Here ρ_{ν_i} is the energy density of i^{th} neutrino, ρ_ν^{FD} is the energy density of a single neutrino species assuming a thermal Fermi-Dirac distribution and no energy gain during the electron-positron annihilation epoch, and ρ_{DR} is the energy density of dark radiation in the form of light particles. With this definition the total radiation density can be written as

$$\rho = \left(1 + \frac{7}{8}\left(\frac{4}{11}\right)^{4/3} N_{\text{eff}}\right)\rho_\gamma\,. \tag{2.42}$$

In SM with only three active neutrino species, the theoretical prediction is $N_{\text{eff}} = 3.046$. The extra 0.046 comes from the partial decoupling of the neutrinos from the thermal bath around $T \simeq 1$ MeV when the electron-positron annihilation took place. Often the part not coming from SM neutrinos is quoted separately as

$$\Delta N_{\text{eff}} = N_{\text{eff}} - 3.046\,. \tag{2.43}$$

There are observational constraints on ΔN_{eff} at epochs in the early Universe. The extra radiation density leads to a faster expansion of the Universe during RD affecting the production of light elements during BBN. The measurement of primordial elements in today's Universe gives $N_{\text{eff}} = 3.28 \pm 0.28$ [114]. The other probe of ΔN_{eff} is the CMB observation. Extra radiation energy density during recombination damps the anisotropy power spectra of the CMB. The Planck experiment has measured $N_{\text{eff}} = 2.99^{+0.34}_{-0.33}$ (TT,TE,EE+lowE+lensing+BAO) [4]. If the mediator particle were relativistic during BBN, i. e., if its mass is $m_\phi \lesssim 1$ MeV, then it would contribute towards ΔN_{eff}, and the BBN bound would be applicable to the model. If $m_\phi < 0.3$ eV, then the CMB bound would also apply.

2.4 SUMMARY & CONCLUSIONS

In this chapter, we reviewed the motivation for self-interacting dark matter models and discussed the late-time nonrelativistic phenomenologies of such models, such as Sommerfeld effect, self-scattering. The abundance of different kinds of particles in the standard model gives the most natural motivation to consider multiparticle dark sector. Several theoretically motivated DM models also predict multiple states in the hidden sector. The proposed solutions to the small scale issues in structure formation predict light dark sector particles that mediate the long range interactions. Such interactions could potentially change the DM annihilation or scattering rate by several orders of magnitude, through late-time nonperturbative effects, relative to the perturbative rates. The light particles would also form excess radiation in the early Universe causing a faster Hubble expansion.

3 SELECTION RULE IN SOMMERFELD EFFECT

In this chapter, we shall discuss the selection rule in Sommerfeld effect in multilevel DM model, and its implications for DM annihilation signal as well as for indirect detection experiments. This chapter is based on our work in Paper I [1].

3.1 A DARK SECTOR MODEL

Now we describe the DM model that we shall use to demonstrate the selection rule in Sommerfeld effect. We consider an approximate global $U(1)$-symmetric theory consisting of a Dirac fermion χ and a complex scalar Φ with charges +1 and -2, respectively, as given by Eq.(3.1). They are coupled to each other through a Majorana-type interaction [76].

$$\begin{aligned}\mathcal{L} \quad \supset \quad & \partial^\mu \Phi^\dagger \partial_\mu \Phi + \mu_\Phi^2 |\Phi|^2 - \lambda_\Phi |\Phi|^4 + i\overline{\chi}\not{\partial}\chi - M\overline{\chi}\chi \\ & - \left(\frac{f}{\sqrt{2}}\Phi\chi^T \mathcal{C}\chi + \text{h.c.}\right) + \mathcal{L}_{U\!\!\!/(1)} \,.\end{aligned} \tag{3.1}$$

The $U(1)$-breaking term here can be of the form, e.g., $b^2\left(\Phi^2 + \Phi^{\dagger 2}\right)$ which we assume to be small. The scalar potential induces nonzero vacuum expectation value v_Φ and splits Φ into a massive mode ρ and a pseudo-Goldstone mode η: $\Phi \to v_\Phi + \rho + i\eta$, breaking the $U(1)$-symmetry spontaneously. Note that the explicit symmetry breaking term violates the prospective shift symmetry of the Goldstone mode and allows us to expand Φ in cartesian form. Due to the Majorana-type coupling with the scalar, χ also splits into two Majorana particles χ_1 and χ_2 with masses m_χ and $m_\chi + \Delta$ where $m_\chi \equiv M - f v_\Phi$ and $\Delta \equiv 2 f v_\Phi$. A residual $\mathcal{Z}_2$-symmetry gives χ_1 stability and renders it as a DM candidate. The final Yukawa couplings between the fermions and the scalars are

$$-\frac{f}{2}\rho(\overline{\chi}_1\chi_1 - \overline{\chi}_2\chi_2) - \frac{f}{2}\eta(\overline{\chi}_2\chi_1 + \overline{\chi}_1\chi_2)\,. \tag{3.2}$$

With these interactions, $\{\chi_1, \chi_2\}$ form a two-level SIDM model. While the ρ couples the similar DM states, the exchange of η leads to off-diagonal coupling. Additionally, the η-interaction allows χ_2 to decay to the lighter state through $\chi_2 \to \chi_1\eta$. The symmetry broken scalar potential reads

$$\begin{aligned}V(\rho,\eta) \quad = \quad & \tfrac{1}{2}m_\rho^2\rho^2 + \tfrac{1}{2}m_\eta^2\eta^2 \\ & + \lambda_\Phi v_\Phi\left(\rho^3 + \rho\eta^2\right) + \lambda_\Phi\left(\rho^4 + \eta^4\right)\,.\end{aligned} \tag{3.3}$$

The mass of η will arise from the $U(1)$-breaking term and the thermal corrections to its propagator. At low energy, we are left with five free parameters– $\{m_\chi,\ m_\rho,\ m_\eta,\ \alpha,\ \Delta\}$.

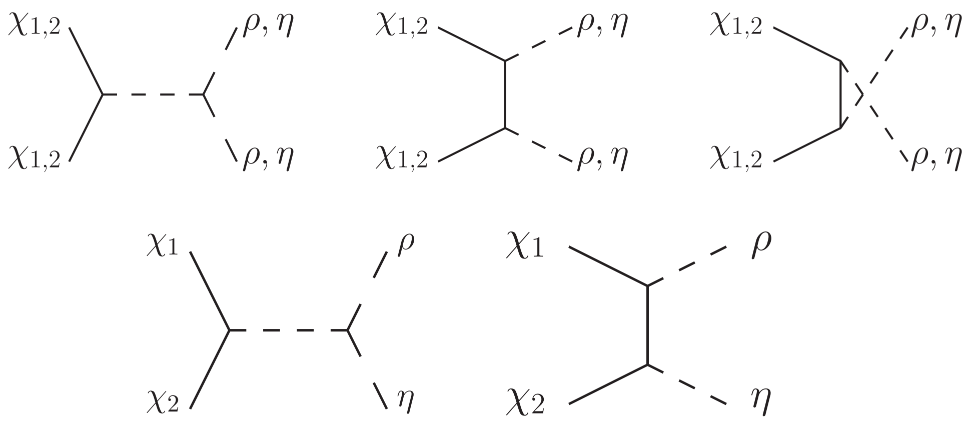

Figure 3.1: Feynman graphs for DM annihilation (top) and coannihilation (below).

3.1.1 *Thermal history of the dark sector*

After the initial production of the dark sector particles, they decouple from the SM particles at some temperature T_*. We assume this to occur at a scale much higher relative to the other energy scales in the theory, i.e., $T_* \gg M,\ \mu_\Phi$. After decoupling, the SM and the dark sectors evolve independently with separate temperatures, defined as T and T_d, respectively. We define the ratio of these temperatures as $\xi_d \equiv T_d/T$. After the spontaneous symmetry breaking at $T_d \simeq v_\Phi$, the dark sector has two Majorana fermions χ_1, χ_2 and two scalars ρ, η. The comoving entropy of this sector changes only during the decays of χ_2 and ρ. In general ξ_d can be written as

$$\xi_d(T) = \left(\frac{g_d(T_*)g_{\rm SM}(T)}{g_d(T_d)g_{\rm SM}(T_*)}\right)^{1/3}. \tag{3.4}$$

Here $g(T)$ is the relativistic degrees of freedom in the respective sector at temperature T. From Fig. 3.2, it is clear that the ratio ξ_d is never too far away from unity. After ρ goes out of chemical equilibrium, it decays into η. We shall also assume some portal between the scalars and the charged leptons– e^+e^-, $\mu^+\mu^-$, $\tau^+\tau^-$ in the SM. This can be realized in a similar way as in the leptophilic models [105, 115]. We shall see later that this preferential decay of ρ, η into the leptons could account for the excess positrons seen in the cosmic ray by several experiments. Dark sector temperature T_d rises after the DM decouples from the thermal bath. Later during the QCD phase transition at $T \sim \Lambda_c$, a large amount of entropy is dumped into the SM thermal bath and heats it up.

We shall always assume that $M < v_\Phi$, so that the symmetry breaking takes place before DM relic abundance formation. The ensuing phenomenology was discussed in Ref.[76, 77]. During relic annihilation, the interactions in Eq.(3.2) provide both annihilation and coannihilation,

$$\begin{aligned} &\chi_1\chi_1,\ \chi_2\chi_2 \to \rho\rho,\ \eta\eta \qquad && \text{annihilation}\,, \\ &\chi_1\chi_2 \to \rho\eta && \text{coannihilation}\,. \end{aligned} \tag{3.5}$$

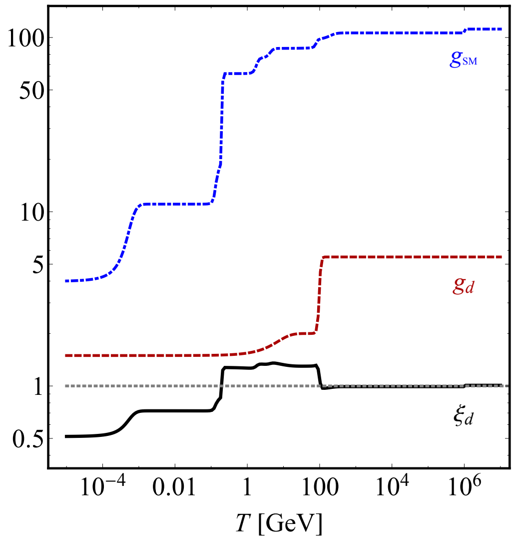

Figure 3.2: Variation of the relativistic degrees of freedom in both SM $g_{\rm SM}$ (red) and dark sector g_d (black). Also shown is the ratio of the dark sector temperature to the SM temperature ξ_d (blue).

Even though in this case the DM is lighter than the symmetry breaking scale v_Φ, the scalar particle can be much lighter than $\chi_{1,2}$ if the hierarchy $v_\Phi > M > \mu_\Phi$ is satisfied.

Because χ_1 and χ_2 are Majorana particles, their annihilation into two scalars does not have any s-wave ($\ell = 0$) component, and hence is p-wave ($\ell = 1$) suppressed. This is because they are identical fermions, their two-body states must have even $(\ell + s)$, such that the total wavefunction is antisymmetric under particle exchange. However, the CP quantum number of the fermions is $(-1)^{\ell+1}$, and that for the final state scalars is simply $(-1)^{\ell_f}$ where ℓ_f is the angular momentum of the final state. Therefore, the conservation of the CP-symmetry restricts $|\ell - \ell_f|$ to be odd, which prohibits the $\ell = 0$, $s = 0$ state for annihilation. Coannihilation is not subject to such restriction as χ_1 and χ_2 are distinguishable.

Even after the DM is not in chemical equilibrium with the other particles in the dark sector, it exchanges kinetic energy with them as kinetic decoupling happens later than the chemical decoupling. In this case, the elastic scattering between χ_1 and η helps keep the DM in kinetic equilibrium with η. It was shown in Ref.[78] that a small mass split between the two DM states enhances this scattering cross section through a resonance, and thus delaying the DM kinetic decoupling to ameliorate the *missing satellite problem* [116].

3.2 SOMMERFELD ENHANCEMENT IN ANNIHILATION

Before annihilation, DM particles interact with each other through the Yukawa interactions in Eq.(3.2). These interactions lead to long range pontentials between the DM particles.

The possible two-body states in the present case are

$$\left.\begin{array}{l}|\chi_1\chi_1\rangle \\ |\chi_2\chi_2\rangle\end{array}\right\} \quad \text{Annihilation}$$

$$\left.\begin{array}{l}|\chi_1\chi_2\rangle \\ |\chi_2\chi_1\rangle\end{array}\right\} \quad \text{Coannihilation} \tag{3.6}$$

The Feynman graphs for annihilation and coannihilation are shown in Fig. 3.1. The η-interaction leads to mixing between the two states in each of annihilation and coannihilation space. But the two subspaces remain separate as neither ρ nor η interaction can couple one to the other. As mentioned before, the annihilation subspace does not have any s-wave process, but coannihilation has both s and p-wave component. Although the two states for coannihilation consist of the same particles, we write them separately because it is easier to understand the transition from one to the other due to the η-exchange. We shall follow the discussion about NREFT given in Ch. 2 to first compute the perturbative cross sections for these three processes, and then calculate the Sommerfeld factors by solving the matrix Schrödinger equations numerically.

3.2.1 *Annihilation matrices*

DM annihilation process typically takes place over a length scale $1/m_\chi$. Therefore typical momentum exchange in such a process is $\sim \mathcal{O}(m_\chi)$. In NREFT, as *hard* modes of momentum exchange are integrated out, the annihilation process cannot be described using tree level graphs. However, like in any EFT, all information regarding these 'high energy' processes is contained the series of higher dimensional operators,

$$\mathcal{L}_{\text{eff}} = \sum_{i,j,k,l} c_{ij,kl}(m_\chi)\, \overline{\chi}_i\chi_j\overline{\chi}_k\chi_l + \dots . \tag{3.7}$$

Here $c_{ij,kl}(m_\chi)$ are the Wilson coefficients computed at the scale m_χ, and $\overline{\chi}_i\chi_j\overline{\chi}_k\chi_l$ are four-Fermi operators– $\overline{\chi}_1\chi_1\overline{\chi}_1\chi_1$, $\overline{\chi}_1\chi_2\overline{\chi}_1\chi_1$, $\overline{\chi}_2\chi_2\overline{\chi}_1\chi_1$, and so on. The $c_{ij,kl}$ coefficients can be calculated by matching a four-point amplitudes in the full theory with the corresponding four-Fermi operator in the effective Lagrangian.

To classify the effective operators according to the spin and angular momentum of the two-body states, we write the Dirac spinors of χ_i using the Pauli two-component spinors ξ_i, η_i as

$$\begin{aligned} u_i(\mathbf{p}) &= \sqrt{\frac{E_i+m_i}{2E_i}}\begin{pmatrix}\xi_i \\ \dfrac{\boldsymbol{\sigma}\cdot\mathbf{p}}{E_i+m_i}\xi_i\end{pmatrix}, \\ v_i(-\mathbf{p}) &= \sqrt{\frac{E_i+m_i}{2E_i}}\begin{pmatrix}\dfrac{-\boldsymbol{\sigma}\cdot\mathbf{p}}{E_i+m_i}\eta_i \\ \eta_i\end{pmatrix}, \end{aligned} \tag{3.8}$$

with $E_i = \sqrt{\mathbf{p}^2 + m_i^2} \simeq m_i + m_i v^2/2$ in the nonrelativistic limit.

Interaction between a Dirac fermion ψ of mass m and a scalar or a vector can lead to the following bi-spinor contractions $\bar{v}(-\mathbf{p})\Gamma u(\mathbf{p})$. We expand them in powers of $|\mathbf{p}|/m_\chi$ and keep terms only upto $\mathcal{O}(|\mathbf{p}|^2/m_\chi^2)$,

$$\begin{aligned}
&\bar{v}(-\mathbf{p})u(\mathbf{p}) = -\frac{1}{m}\eta^\dagger \mathbf{p}\cdot\boldsymbol{\sigma}\xi\,,\\
&\bar{v}(-\mathbf{p})\gamma^0 u(\mathbf{p}) = 0\,,\\
&\bar{v}(-\mathbf{p})\gamma^0\gamma^5 u(\mathbf{p}) = \left(1-\frac{\mathbf{p}^2}{2m^2}\right)\eta^\dagger\xi\,,\\
&\bar{v}(-\mathbf{p})\gamma^i u(\mathbf{p}) = \eta^\dagger\boldsymbol{\sigma}\xi - \frac{\mathbf{p}^i}{2m^2}\eta^\dagger\mathbf{p}\cdot\boldsymbol{\sigma}\xi\,,\\
&\bar{v}(-\mathbf{p})\gamma^0\gamma^i u(\mathbf{p}) = -\left(1-\frac{\mathbf{p}^2}{m^2}\right)\eta^\dagger\boldsymbol{\sigma}^i\xi - \frac{\mathbf{p}^i}{2m^2}\eta^\dagger\mathbf{p}\cdot\boldsymbol{\sigma}\xi\,,\\
&\bar{v}(-\mathbf{p})\gamma^i\gamma^5 u(\mathbf{p}) = \frac{i}{m}\eta^\dagger(\mathbf{p}\times\boldsymbol{\sigma})^i\xi\,,\\
&\bar{v}(-\mathbf{p})\gamma^5 u(\mathbf{p}) = -\eta^\dagger\xi\,.
\end{aligned} \tag{3.9}$$

Here we have suppressed the spinor index on ζ_i and η_i for clarity.

The two bi-spinors $f(\mathbf{p})\eta^\dagger\xi$ and $g(\mathbf{p})\eta^\dagger\boldsymbol{\sigma}\xi$ are the scalar (spin $s = 0$) and vector (spin $s = 1$) combinations, respectively. All expressions are approximated to the order $\mathcal{O}((|\mathbf{p}|/m)^3)$. In the four-Fermi operators, two bi-spinors are combined together. The orbital angular momentum of such combinations is dictated by the rotational symmetry property of individual operator. A few relevant examples are listed in Table 3.1 where we used the notations: $\mathbf{v} = \mathbf{p}/m$, $(\xi'^\dagger\eta')(\eta^\dagger\xi) = \mathbf{1}\otimes\mathbf{1}$, $(\xi'^\dagger\boldsymbol{\sigma}^i\eta')\cdot(\eta^\dagger\boldsymbol{\sigma}^i\xi) = \boldsymbol{\sigma}^i\otimes\boldsymbol{\sigma}^i$, $(\xi'^\dagger\mathbf{v}'\cdot\boldsymbol{\sigma}\eta')(\eta^\dagger\mathbf{v}\cdot\boldsymbol{\sigma}\xi) = \mathbf{v}'\cdot\boldsymbol{\sigma}\otimes\mathbf{v}\cdot\boldsymbol{\sigma}$, and $(\xi'^\dagger\mathbf{v}\cdot\boldsymbol{\sigma}\eta')(\eta^\dagger\mathbf{v}'\cdot\boldsymbol{\sigma}\xi) = \mathbf{v}\cdot\boldsymbol{\sigma}\otimes\mathbf{v}'\cdot\boldsymbol{\sigma}$.

The effective operators are classified according to their spin and angular momentum

$$\mathcal{L}_{\text{eff}} = \sum_{i,j,k,l}\sum_{\ell,s} c_{ij,kl}(^{2s+1}\ell_J)\,\mathcal{O}_{ij,kl}(^{2s+1}\ell_J)\,, \tag{3.10}$$

where $\mathcal{O}_{ij,kl}(^{2s+1}\ell_J)$ are the effective operators consisting of the spinors ξ_i, η_i corresponding to spin s and angular momentum ℓ of the associated two-body states [117].

To find the annihilation matrices in Eq.(3.12) for a particular process $|a\rangle \to X_A X_B$ where $|a\rangle = \{|\chi_1\chi_1\rangle, |\chi_2\chi_2\rangle\}$ for annihilation, and $\{|\chi_1\chi_2\rangle, |\chi_2\chi_1\rangle\}$ for coannihilation, we performed the following steps in `Mathematica`.

1. Write down the amplitude for $\Gamma_{ab} = |a\rangle \to X_A X_B \to |b\rangle$ using two-component spinors.

2. Expand it in powers of $|\mathbf{p}|/m_\chi$ and other small numbers, like m_ρ/m_χ, Δ/m_χ.

3. Collect the the terms that correspond to an operator $f(^{2s+1}\ell_J)$.

Once the Wilson coefficients are known, the annihilation cross sections into the light scalars can be found by using the Cutkosky theorem which

OPERATOR	${}^{2s+1}\ell_J$
$\mathbf{1} \otimes \mathbf{1}$	$f({}^1S_0)$
$\boldsymbol{\sigma}^i \otimes \boldsymbol{\sigma}^i$	$f({}^3S_1)$
$v^2\mathbf{1} \otimes \mathbf{1}$	$h({}^1S_0)$
$\mathbf{v}' \cdot \mathbf{v}\,\mathbf{1} \otimes \mathbf{1}$	$g({}^1P_1)$
$\mathbf{v}' \cdot \mathbf{v}\,\boldsymbol{\sigma}^i \otimes \boldsymbol{\sigma}^i$	$\frac{1}{2}(g({}^3P_2) + g({}^3P_1))$
$\mathbf{v}' \cdot \boldsymbol{\sigma} \otimes \mathbf{v} \cdot \boldsymbol{\sigma}$	$\frac{1}{3}(g({}^3P_0) - g({}^3P_2))$
$\mathbf{v} \cdot \boldsymbol{\sigma} \otimes \mathbf{v}' \cdot \boldsymbol{\sigma}$	$\frac{1}{2}(g({}^3P_2) - g({}^3P_1))$

Table 3.1: Symmetries of the four-Fermi operators.

states that the annihilation cross section of a process $\chi_i\chi_j \to X_A X_B$ is proportional to the imaginary part of the Wilson coefficient of the operator $\chi_i\chi_j \to X_A X_B \to \chi_i\chi_j$ [118]. If $(\sigma v)_{\chi_i\chi_j \to X_A X_B} \equiv \Gamma\left(\chi_i\chi_j \to X_A X_B\right)$ is the annihilation rate then

$$(\sigma v)_{\chi_i\chi_j \to X_A X_B} = 2\,\mathrm{Im}\left[c_{ij,ij}({}^{2s+1}\ell_J)\right]. \tag{3.11}$$

In addition to $|\mathbf{p}|/m_\chi$, we also expand the operators in powers of other dimensionless parameters, such as m_ρ/m_χ, m_η/m_χ, and Δ/m_χ. We computed the Wilson coefficients for both annihilation and coannihilation using `FeynCalc` package in `Mathematica`[1] and classified them according to their spin and angular momentum [119].

To the leading order in the dimensionless parameters mentioned above, we get the following annihilation matrices.

$$\begin{aligned} \Gamma^{\text{ann}}_{\ell=1,s=1} &= \frac{2\pi\alpha^2 v^2}{m_\chi^2}\begin{pmatrix} +1 & +1 \\ +1 & +1 \end{pmatrix}, \\ \Gamma^{\text{coann}}_{\ell=0,s=1} &= \frac{\pi\alpha^2}{16 m_\chi^2}\begin{pmatrix} +1 & -1 \\ -1 & +1 \end{pmatrix}, \\ \Gamma^{\text{coann}}_{\ell=1,s=1} &= \frac{\pi\alpha^2 m_\rho^2 v^2}{16 m_\chi^4 \Delta^2}\begin{pmatrix} +1 & +1 \\ +1 & +1 \end{pmatrix}. \end{aligned} \tag{3.12}$$

The $\ell = 0$ coannihilation matrix has opposite signs for the off-diagonal entries relative to the diagonal elements. However, all elements of the $\ell = 1$ matrices have the same sign. This fact is related to the particle exchange symmetry, and will be discussed in more detail when we describe our results. It is unique to this model, and relates to its ability to explain the AMS-02 positron excess and avoid the dwarf galaxy constraint.

1 Notebooks are available at https://github.com/anirbandas89/NREFT_Matching

3.2.2 *Sommerfeld factors*

We shall first review the formalism of the computation of the Sommerfeld effect in DM models with multiple states with diagonal and off-diagonal long range interactions between them, following Ref. [120].

Let us assume, a general N-level system with a spherically symmetric $N \times N$ matrix potential. The lightest states has a mass m_χ, and the higher state masses are $m_i = m_\chi + \Delta_i$. We shall always assume the mass gaps to be much smaller than the lightest state mass, i. e., $\Delta_i \ll m_\chi$. The complete Schrödinger equation reads

$$\left[\left(-\frac{\nabla^2}{2\mu} - E\right)\delta_{ij} + V(r)_{ij}\right]\Psi(\mathbf{r})_{jk} = 0\,. \tag{3.13}$$

Here, we have approximated the reduced mass of all states to be $\mu_{ij} \simeq \mu = m_\chi/2$. Therefore, the energy E is given by

$$E = \frac{1}{2}\mu v_{\text{rel}}^2 = m_\chi v^2\,. \tag{3.14}$$

The mass gap between different states means that the threshold for coannihilation occurs at velocity $v_a^{\text{thr}} \equiv \sqrt{(m_a - 2m_\chi)/m_\chi} = \sqrt{\Delta_a/m_\chi}$ for the two-body state $|\chi_i\chi_j\rangle$ with total mass m_a. Therefore, we define the momentum

$$k_a^2 = m_\chi(E - \Delta_a)\,. \tag{3.15}$$

If k_a is real then the channel a is kinematically open. An imaginary k_a means the channel is closed.

The asymptotic solution of the wavefunction should look like

$$\Psi(\mathbf{r})_{ij} \overset{r\to\infty}{=} \delta_{ij}e^{-ik_i z} + f_{ij}(\theta)\frac{e^{ik_i r}}{r}\,. \tag{3.16}$$

The first term describes an incoming plane wave along the z-direction, and the second term describes an outgoing spherical wave with scattering amplitude $f_{ij}(\theta)$, assuming azimuthal symmetry. The solution of Eq.(3.13) has to be matched with this expression at large r.

The full wavefunction is expanded in the partial wave basis as

$$\Psi(\mathbf{r})_{ij} = \sum_\ell \psi_\ell(\mathbf{r})_{ij} = \sum_\ell \frac{u_\ell(r)_{ik}}{r} A_{kj} P_\ell(\cos\theta)\,. \tag{3.17}$$

The reduced radial wavefunction $u(r)_{ij}$ obeys the equation

$$\left[\left(-\frac{d^2}{dr^2} + \frac{\ell(\ell+1)}{r^2} - m_\chi E\right)\delta_{ij} + m_\chi V(r)_{ij}\right]u_\ell(r)_{jk} = 0\,. \tag{3.18}$$

This equation has $2N$ number of linearly independent solutions, out of which N are regular at the origin, the rest being irregular. The asymptotic form of the regular solutions is given by

$$u_\ell(r)_{ij} \overset{r\to\infty}{=} N_{ij}\sin\left(k_i r - \frac{\ell\pi}{2} + s_{ij}\right)\,, \tag{3.19}$$

where N_{ij} are constant coefficients, s_{ij} are scattering phase shifts. We compare this asymptotic form with $\Psi(\mathbf{r})$ in Eq.(3.17) to find

$$A_{ij} = i^{\ell}(2\ell+1)\frac{\left[M^{-1}\right]_{ij}}{k_i}\,. \tag{3.20}$$

Here, we used $M_{ij} = N_{ij}e^{-is_{ij}}$. In last two equations, no summation is implied over any repeated index. For Sommerfeld factor, we need the wavefunction and its radial derivative of the wavefunction at the origin. The series expansion of the reduced wavefunction $u_\ell(r)$ around $r=0$ reads

$$u_\ell(r)_{ij} = \frac{1}{(\ell+1)!}u_\ell^{(\ell+1)}(0)_{ij}\, r^{\ell+1} + \dots\,, \tag{3.21}$$

where $u_\ell^{(\ell+1)}(0)_{ij}$ is the $(\ell+1)$-th derivative of $u_\ell(r)_{ij}$ at the origin. Using this in the full solution yields

$$\psi_\ell(\mathbf{r})_{ij} \overset{r\to 0}{=} \frac{i^{\ell}(2\ell+1)}{(\ell+1)!}u_\ell^{(\ell+1)}(0)_{ik}\frac{\left[M^{-1}\right]_{kj}}{k_j}\, r^{\ell}P_\ell(\cos\theta)\,. \tag{3.22}$$

The ratio of this near-origin solution to the free particle exact solution gives

$$[Q_\ell]_{ij} = \frac{(2\ell+1)!!}{(\ell+1)!}\left[u_\ell^{(\ell+1)}(0)\right]^*_{ik}\frac{\left[M^{-1}\right]^*_{kj}}{k_j^{\ell+1}}\,. \tag{3.23}$$

To use this, one needs to know the matrix M containing the phase shifts s_{ij}. It is avoided by using the fact that the Wronskian W_ℓ of the linearly independent solutions of the Schrödinger equation is r-independent. We compute the Wronskian both at $r\to 0$ and $r\to\infty$ limits and compare them to obtain the M matrix in terms of the amplitude of the wavefunctions at infinity.The Wronskian is defined as

$$W_\ell(r)_{ij} \equiv v_\ell^\dagger(r)_{ik}u_\ell'(r)_{kj} - v_\ell^{\dagger\prime}(r)_{ik}u_\ell(r)_{kj}\,, \tag{3.24}$$

where $v_\ell(r)_{ij}$ are the irregular solutions and prime denotes derivative w.r.t. r. They have the asymptotic behaviour

$$v(r)_{ij} \overset{r\to 0}{=} \delta_{ij}r^{-\ell}, \quad v(r)_{ij} \overset{r\to\infty}{=} T^\dagger_{ij}e^{-ik_i r}. \tag{3.25}$$

Substituting the asymptotic forms of the solutions we find

$$\begin{aligned} W_\ell(r)_{ij} &\overset{r\to 0}{=} \frac{2\ell+1}{(\ell+1)!}\frac{d^{\ell+1}u_\ell(r)}{dr^{\ell+1}}\bigg|_{r=0}\,, \\ W_\ell(r)_{ij} &\overset{r\to\infty}{=} i^{\ell}\textstyle\sum_a k_a T_{ia}M_{aj}\,. \end{aligned} \tag{3.26}$$

Now equating these two quantities yields the phase shift matrix M in terms of the large-r amplitude T. Using this in Eq.(3.23) yields,

$$[Q_\ell]_{ij} = (2\ell-1)!!\, i^{-\ell}\frac{T^\dagger_{ij}}{k_i^{\ell}}\,. \tag{3.27}$$

Using this expression for the wavefunction at the origin in the definition of Sommerfeld factor gives

$$[S_\ell]_i = \left(\frac{(2\ell-1)!!}{k_i^\ell}\right)^2 \frac{\left[T^\dagger\right]_{ia} \Gamma_{ab}({}^{2s+1}\ell_J) T_{bi}}{\Gamma_{ii}({}^{2s+1}\ell_J)}\,. \tag{3.28}$$

Here, no summation is implied over the index i.

The T matrix is computed by solving the Schrödinger equation numerically. A short algorithm is provided below.

1. Eq.(3.18) is solved in between $r = r_0$ and r_f. The point r_0 is chosen such that the centrifugal term dominates over the potential and Eq.(3.21) is valid. The initial conditions are as follows

$$u_\ell(r_0)_{ij} = \frac{r_0^{\ell+1}}{2\ell+1}\,\delta_{ij}, \qquad u'_\ell(r_0)_{ij} = \frac{(\ell+1) r_0^\ell}{2\ell+1}\,\delta_{ij}\,. \tag{3.29}$$

   With this choice of the boundary conditions, the Wronskian turns out to be exactly identity from Eq.(3.24).

2. At a large $r = r_f$, the Wronskian is written as below, using Eq.(3.25) and (3.24).

$$W_\ell(r_f)_{ij} = T_{ia}\left[u'_\ell(r_f)_{aj} - ik_i u_\ell(r_f)_{aj}\right] e^{ik_i r_f} = \delta_{ij}\,. \tag{3.30}$$

3. The T matrix obtained by inverting the B matrix,

$$T = B^{-1}, \qquad B_{ij} \equiv \left[u'_\ell(r_f)_{ij} - ik_i u_\ell(r_f)_{ij}\right] e^{ik_i r_f}. \tag{3.31}$$

4. The stability of the result is ensured by increasing r_f until S_ℓ is independent of r_f.

This procedure works well when all the two-body states are kinematically open, i.e. all k_is are real. When this is not the case, the wavefunctions of the closed states are exponentially growing/decaying which, through mixing with other states, makes the whole system numerically unstable. Thus the matrix inversion in Eq.(3.31) with those solutions becomes difficult. To mitigate this problem, we followed the modified variable phase method as outlined in Refs.[121, 122]. The key improvement in this technique is to separate out the free particle solution (i. e., the Bessel functions) from the full solution, and then find out the modification to free solution. We implemented the numerical routines in `Mathematica`.

In the present scenario, the potential $V(r)$ that arises from the exchange of the scalars ρ and η is given by

$$V(r) = \begin{pmatrix} V_{11} & V_{12} \\ V_{21} & V_{22} \end{pmatrix}, \tag{3.32}$$

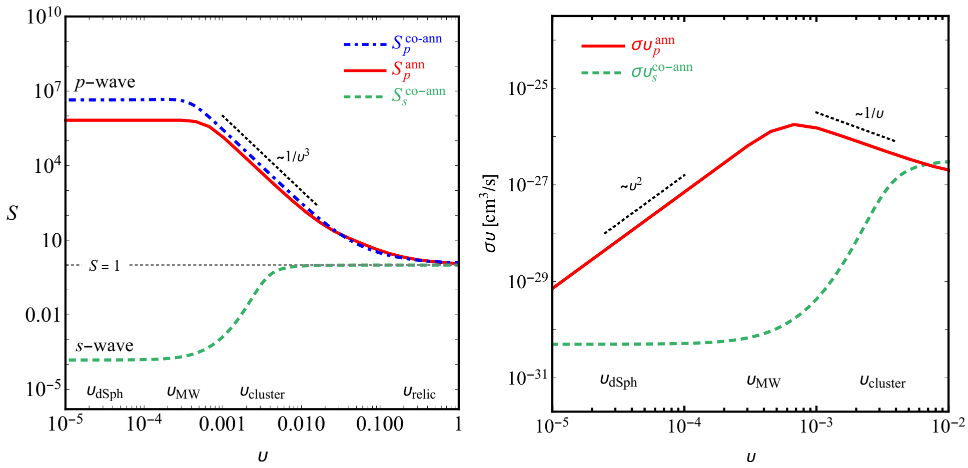

Figure 3.3: (Left) Sommerfeld factors for annihilation (p-wave) and coannihilation (s and p-wave) as a function of DM velocity v. (Right) Annihilation rate for p-wave. Off-diagonal mediator mass is fixed to be $m_\eta = 0.7 m_\rho$. Other parameters are $\alpha = 0.036$, $m_\rho / m_\chi = 0.0016$, $\Delta / m_\chi = 0.001$.

with $V_{11} = -\alpha\, e^{-m_\rho r}/r$, $V_{12} = V_{21} = -\alpha\, e^{-m_\eta r}/r$, and $V_{22} = -\alpha\, e^{-m_\rho r}/r + 2\Delta$ for annihilation and $V_{22} = -\alpha\, e^{-m_\rho r}/r$ for coannihilation. The extra term 2Δ in V_{22} for annihilation comes from the mass gap between the two two-body states $|\chi_1\chi_1\rangle$ and $|\chi_2\chi_2\rangle$. No such mass gap exist for coannihilation.

We solved the Schrödinger equation using two methods– a) directly using `NDSolve` in `Mathematica`, and b) using the *variable phase method*. The direct method works well as long as the kinetic energy of the incoming particles is above the threshold for the $|\chi_2\chi_2\rangle$ state, i. e.,

$$E \geq 2\Delta\,. \tag{3.33}$$

When the incoming particles are below threshold, the wavefunctions for $|\chi_2\chi_2\rangle$ final state are not scattering state anymore. In this case, the direct method fails as it simultaneously tries to solve for scattering and bound state solutions within a single system. We have verified the results from the variable phase method with direct method solutions for above threshold parameters. We found excellent match between the results.

3.3 SELECTION RULE

To reduce the number of parameters, we fix $m_\eta = 0.7 m_\rho$ for all the results shown in this thesis. In the left panel of Fig. 3.3, we show the Sommerfeld factors as a function of DM velocity v. Both p-wave annihilation and coannihilation show large enhancement in the small velocity limit. The enhancement factor has a $1/v^3$-dependence in the intermediate velocity regime. However, the s-wave Sommerfeld factor is less than one. In the right panel, we show the annihilation rate $S\sigma_0 v$ for the same set parameters. The v^2-dependence of the perturbative cross section convoluted with the Sommerfeld factor yields a nonmonotonic behaviour of σv with velocity –

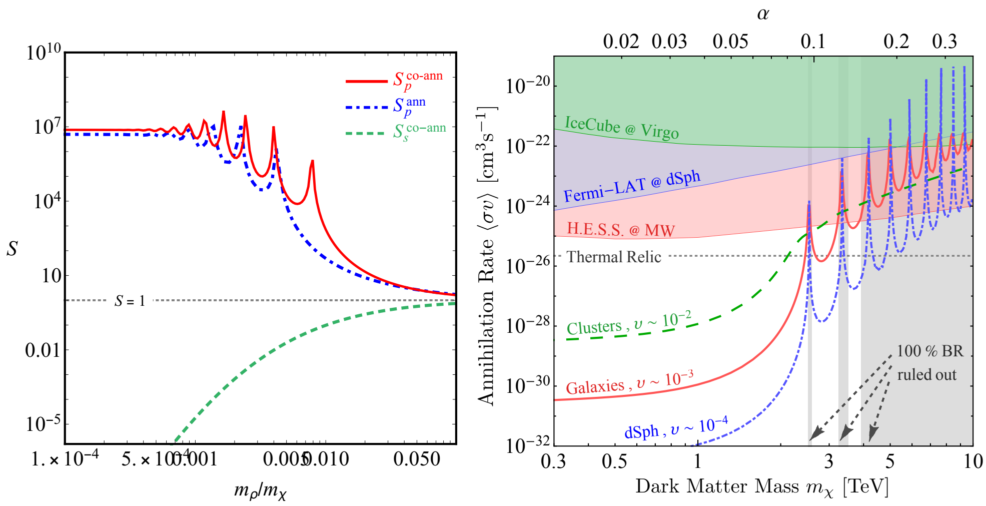

Figure 3.4: (Left) Sommerfeld factors for annihilation (p-wave) and coannihilation (s and p-wave) as a function of the diagonal mediator mass m_ρ. Off-diagonal mediator mass is fixed to be $m_\eta = 0.7 m_\rho$. Other parameters are $\alpha = 0.036$, $m_\rho/m_\chi = 0.0016$, $\Delta/m_\chi = 0.001$. (Right) The p-wave annihilation rates for different astrophysical objects. Indirect detection search constraints from the respective sources are also shown. We chose $m_\rho = 30$ GeV, $m_\eta = 0.9 m_\rho$, and $\Delta = 10$ GeV for this figure. This figure is reproduced from Paper I [1].

rising as $\sim v^2$ at small velocity, followed by a $\sim 1/v$ fall at larger v. As a result, the annihilation rate is maximum at some intermediate velocity.

Fig. 3.4 shows the m_ρ-dependence of the factors. In addition to a large overall enhancement for p-wave, a resonance feature is also present for certain values of m_ρ.

In all cases, the s-wave process is suppressed. We shall explain the origin of this selective enhancement in the rest of this section.

3.3.1 *Particle exchange symmetry*

We shall use the particle exchange symmetry following Paper I [1]. Suppose, A and B are two fermions. They can form two two-body states, namely $|AB\rangle$ and $|BA\rangle$ of total angular momentum ℓ and spin s. However, these two states consist of the same set of particles and are related to each other through an exchange of them,

$$|AB\rangle = (-1)^{\ell+s}|BA\rangle\,. \tag{3.34}$$

This factor has three components: $(-1)^\ell$ from relative angular momentum, $(-1)^{s+1}$ from their spins, and (-1) due to Wick exchange of two fermions.

We can directly apply this to the coannihilation channel in the present model implying that two states $|\chi_1\chi_2\rangle$ and $|\chi_2\chi_1\rangle$ in the matrix Schrödinger equation are related to each other,

$$|\chi_1\chi_2\rangle = (-1)^{\ell+s}|\chi_2\chi_1\rangle\,. \tag{3.35}$$

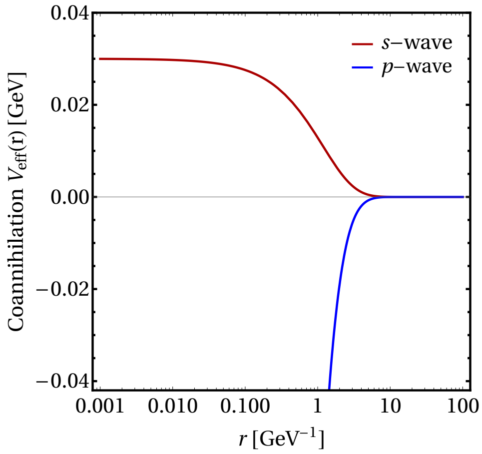

Figure 3.5: The 1D effective potential for coannihilation for $m_\rho = 1$ GeV, $m_\eta = 0.7$ GeV, and $\alpha = 0.1$.

It further implies that we can combine the two equations into a single equation with an effective potential which is a linear combination of the diagonal and off-diagonal potentials,

$$V_{\rm eff} = V_{11} + (-1)^{\ell+s} V_{12}\,. \tag{3.36}$$

Therefore $V_{\rm eff}$ has the following forms for the two cases,

$$\begin{aligned} \ell = 0,\, s = 1: \quad V_{\rm eff} &= -\frac{\alpha\, e^{-m_\rho r}}{r} + \frac{\alpha\, e^{-m_\eta r}}{r}\,, \\ \ell = 1,\, s = 1: \quad V_{\rm eff} &= -\frac{\alpha\, e^{-m_\rho r}}{r} - \frac{\alpha\, e^{-m_\eta r}}{r}\,. \end{aligned} \tag{3.37}$$

We note that in the $\ell = 0$ case, the difference between the two potentials is acting as the effective 1D potential. When $r \ll 1/m_\rho$, m_η, $V_{\rm eff}$ saturates to the value $(m_\rho - m_\eta)$. For larger r, it gradually decreases to zero never becoming negative. The nature of the net potential thus becomes *repulsive* (See Fig. 3.5). However for $\ell = 1$, the diagonal and off-diagonal potentials are added with the same sign, and hence yield an *even stronger attractive* potential. This explains the behaviour of the different Sommerfeld factors in Figs. 3.3 and 3.4. The effective repulsive nature of $V_{\rm eff}$ leads to the suppression in $S_s^{\rm coann}$.

Velocity dependence & resonances

The $1/v^3$-dependence of S_p in Fig. 3.3 can be understood by taking the limit $m_\rho/m_\chi \ll 1$ and $\alpha/v \gg 1$. In this Coulomb limit, an analytic expression for S_ℓ for general angular momentum ℓ is given by [98]

$$S_\ell = S_0 \prod_{m=1}^{\ell} \left(1 + \frac{\alpha^2/v^2}{m^2}\right)\,, \tag{3.38}$$

where S_0 is the s-wave factor in the Coulomb approximation

$$S_0 = \frac{\pi\alpha/v}{1-e^{-\pi\alpha/v}}\,. \tag{3.39}$$

Clearly, for small velocity $S_\ell \sim 1/v^{2\ell+1}$. For finite m_ρ, the Sommerfeld factor does not grow indefinitely for smaller velocity. Instead, it saturates to a constant value when the de Broglie wavelength of the DM particles gets much longer than the range of the potential, i. e., approximately when the condition $\mu_1 v/m_\rho \ll 1$ is met.

Resonances from virtual bound states arise and cause large Sommerfeld enhancement as can be seen in Fig. 3.4. This occurs whenever the range of the potential matches a multiple n of the Bohr radius $1/2\alpha m_\chi$ of the DM particles, i. e., [98]

$$\frac{\alpha m_\chi}{\kappa m_\rho} = n^2, \qquad n = 1, 2, 3, \ldots\,. \tag{3.40}$$

Here $\kappa \simeq \pi^2/6$. Note that this resonance condition is only approximately true in the present model as we have two mediators with slightly different masses. Also the presence of the mass gap Δ shifts the resonance positions by a small amount [120].

The right panel of Fig. 3.4 illustrates the source-specific m_χ-dependence of the p-wave annihilation rates. In the mass range $m_\chi \gtrsim 3$ TeV, the galactic annihilation rate is larger than the rates in dwarf galaxies or galaxy clusters. Moreover, in this region of the parameter space the predicted annihilation rate is even greater than the thermal relic cross section (shown in dotted black line). The H.E.S.S. experiment already rules out much of the parameter space if 100% branching ratio of the annihilation products into SM particles is assumed.

3.4 galactic positron excess

An important consequence of the peculiar velocity scaling of the p-wave Sommerfeld factor is that it predicts different annihilation rate of DM in astrophysical objects of different size. In the net p-wave annihilation rate, the perturbative cross section provides an additional velocity scaling $\sim v^2$. Therefore, the enhanced annihilation rate $S_p\,\sigma v$ first increases as $\sim v^2$ for small velocity, reaches a maximum, and then falls as $\sim 1/v$, as shown in Fig. 3.3. The position of the maximum annihilation depends on the ratio m_ρ/m_χ. Hence this model naturally predicts large DM annihilation signal in the galaxies with $\langle\sigma v\rangle \sim$ a few $\times 10^{-24}\,\mathrm{cm}^3/\mathrm{s}$ which is needed to explain the positron excess seen by the AMS-02 experiment [123], but small signal from the dwarf galaxies. In the left panel of Fig. 3.6, we show the variation of the DM annihilation rate with m_ρ/m_χ and α in the MW. The points within the overlaid white band yield a relic annihilation cross section within $2-3\times 10^{-26}\,\mathrm{cm}^3/\mathrm{s}$. Clearly a few resonant points within the white band, marked with yellow asterisks, can provide large enough annihilation cross section to explain the AMS-02 positron excess without running into problem with thermal relic or dwarf galaxy constraints.

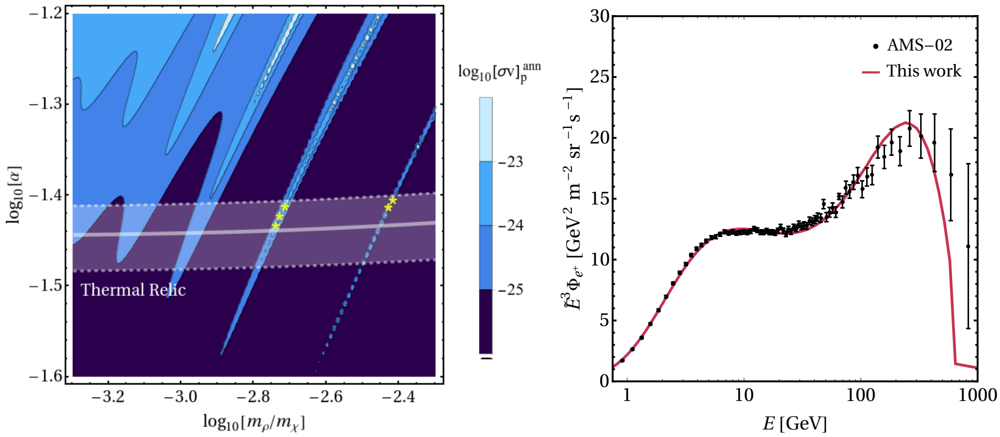

Figure 3.6: (Left) A contour plot showing the variation of the p-wave annihilation rate with m_ρ/m_χ and α. The white band shows the region of the parameter space with relic annihilation cross section within $2-3\times 10^{-26}\,\mathrm{cm}^3/\mathrm{s}$. The parameter points marked with asterisks can yield large annihilation cross section $\langle\sigma v\rangle \sim$ a few $\times 10^{-24}\,\mathrm{cm}^3/\mathrm{s}$ and satisfy the relic constraint. (Right) A representative plot of the positron flux in our model with the parameters shown in Tab. 3.2.

We computed the expected positron flux spectrum in our galaxy using `PPPC4DMID` [124]. We assume that the annihilation products ρ, η couple to the charged leptons through some leptophilic portal. We show a representative plot of the spectrum along with the data in the right panel of Fig. 3.6. An astrophysical background of positron flux was assumed following Ref. [123],

$$F_{e^+}(E) = C_d^2\left(\frac{E^2}{\hat{E}^2}\right)\left(\frac{\hat{E}}{E_1}\right)^{\gamma_d} \tag{3.41}$$

where $\hat{E} = E + \phi_{e^+}$ is the positron energy in the interstellar space. The dark sector and the astrophysical background parameters used in the figure are listed in Table 3.2. Note that we are not using the values quoted in Ref. [123]

Parameter	Value
m_χ	780 GeV
σv	$4.63\times 10^{-24}\,\mathrm{cm}^3/\mathrm{s}$
B.R.(e^+e^-)	38%
B.R.$(\mu^+\mu^-)$	62%
Halo profile	Einasto
C_d	$6.42\times 10^{-2}\,(\mathrm{GeV\,m^2\,s\,sr})^{-1}$
ϕ_{e^+}	0.869 GeV
E_1	7 GeV
γ_d	-3.6

Table 3.2: The dark sector and background model parameters used in Fig. 3.6.

since this is an independent model.

This section of the work is not published yet, and will be a part of a future publication.

3.5 SUMMARY & CONCLUSIONS

In this chapter, we discussed about a selection mechanism in the Sommerfeld enhancement that leads to large and possibly observable p-wave DM annihilation rates in the present Universe, without enhancing s-wave rates at the same time. The key signature of this mechanism is the velocity-dependence and source-dependence of $\langle \sigma v \rangle$, with the possibility of it exceeding $\langle \sigma v \rangle^{\text{relic}}$. These features are distinctive of large p-wave annihilation of degenerate multi-level DM.

We described a DM model implementing the selection mechanism and showed that large parts of its parameter space are already probed by existing experiments, thanks to the Sommerfeld-enhanced annihilation rate. We also demonstrated that using the large p-wave Sommerfeld enhancement, it is possible to explain the galactic positron excess seen in the cosmic ray experiments without exceeding the bounds from dwarf galaxy observations. The exact constraints are model-dependent, but in general multi-source indirect DM detection, cosmological searches for dark radiation, and small-scale DM structure are the main ways to test this mechanism. Collider searches can pin down the dark-to-visible sector connection.

This mechanism opens up a new area for model-building and phenomenology, allowing enhanced DM annihilations in specific sources where DM has velocities in an optimal range. As further work, one may also consider the several variations on this theme: more than two DM particles in the dark sector, gauge particle mediator, even-s incoming states, multiple mediators, etc. Some of these possibilities may also turn out to be theoretically interesting and find phenomenological application.

4

INELASTIC DARK MATTER SCATTERING

In this chapter, we shall discuss the nontrivial self-scattering phenomenologies, such as additional energy dissipation from DM halo, arising from the multilevel nature of the DM. The discussion in this chapter is based on Paper II [2].

4.1 TWO-LEVEL DARK MATTER MODEL

We consider a simple version of the two-level DM model inspired from the previous chapter. Suppose, χ_1 and χ_2 are the two DM states with masses m_χ and $m_\chi + \Delta$, respectively. We again assume $\Delta \ll m_\chi$. The DM states have diagonal and off-diagonal Yukawa interactions mediated by two scalars ρ_1 and ρ_2 of equal mass m_ρ,

$$\mathcal{L}_{\text{int}} \supset f\rho_1 \left(\bar{\chi}_1\chi_1 - \bar{\chi}_2\chi_2\right) + f\rho_2 \left(\bar{\chi}_1\chi_2 + \bar{\chi}_2\chi_1\right) . \tag{4.1}$$

Through scattering, two DM particles in the ground state can either stay in the ground state (elastic) or upscatter to the excited state (inelastic). For upscattering to occur, the incoming particles need to have enough kinetic energy to overcome the mass gap 2Δ between the two two-body states, $|\chi_1\chi_1\rangle$ and $|\chi_2\chi_2\rangle$. However, even if there is not enough kinetic energy, the excited state can be produced as virtual particles during the collision. Moreover, the scattering cross-section between nonrelativistic DM particles is enhanced due to exchange of the light particles. We show the schematic

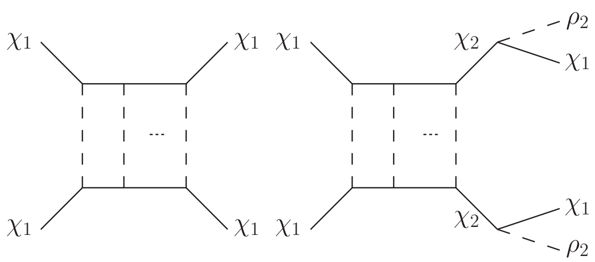

Figure 4.1: Feynman graphs for elastic self-scattering of DM in the ground state (left) and for upscattering induced decay (right). The vertical lines represent multiple exchanges of scalar particles in the nonrelativistic limit of the incoming DM particles.

Feynman graphs for the possible elastic and inelastic scatterings in Fig. 4.1 where the vertical lines represent exchange of many $\rho_{1,2}$ particles in the nonrelativistic regime. In the case of inelastic scattering, the final particles decay to the ground state by emitting two light particles. DM particles lose energy in this process as the final χ_1 particles are less energetic than the initial ones. This energy loss mechanism can potentially lead to interesting phenomenology which will be discussed later.

We computed scattering cross-sections by calculating the transition amplitude between an allowed initial state $|i\rangle$ and final state $|f\rangle$. The possible two-body states are $|\chi_1\chi_1\rangle$, $|\chi_2\chi_2\rangle$ and $|\chi_1\chi_2\rangle$. However, as one can see from Eq.(4.1), the states $|\chi_1\chi_1\rangle$ and $|\chi_2\chi_2\rangle$ are decoupled from $|\chi_1\chi_2\rangle$. Therefore, we shall always assume that the DM particles are initially in the ground state. Hence it suffices to work in a space spanned by $|\chi_1\chi_1\rangle$ and $|\chi_2\chi_2\rangle$ only. This restriction could be removed, but it makes the calculation more difficult, and does not yield any qualitatively new features. We neglect the scattering between χ_1 and χ_2, because χ_2 decays soon after freeze-out and its population is rapidly depleted. For the same reason, the scattering between two χ_2 particles will also not be considered. Therefore, we have two channels, i.e., the elastic cross section σ_{el} for $|\chi_1\chi_1\rangle \to |\chi_1\chi_1\rangle$, and inelastic cross section σ_{in} for $|\chi_1\chi_1\rangle \to |\chi_2\chi_2\rangle$.

The overlap between two 2-body states is defined as $u_{ab} \equiv \langle\chi_a\chi_a|\chi_b\chi_b\rangle$ with $a, b = 1, 2$ and satisfies the Schrödinger equation,

$$\left[\frac{1}{r^2}\frac{d}{dr}\left(r^2\frac{d}{dr}\right) + k^2 - \frac{\ell(\ell+1)}{r^2} - 2\mu V(r)\right] u_\ell(r) = 0\,, \tag{4.2}$$

where ℓ is the orbital angular momentum, and k is a diagonal matrix with the momentum of the incoming 2-body state,

$$k = k_a\delta_{ab}, \quad \text{and}\,. \tag{4.3}$$

The incoming momentum k_a is different for the two 2-body states due to the presence of the mass gap $2\Delta = 2(M_2 - M_1)$ between the states $|\chi_1\chi_1\rangle$ and $|\chi_2\chi_2\rangle$. Depending on the energy

$$E_1 = k_1^2/2\mu_1 = \mu_1 v^2/2 \tag{4.4}$$

two cases are possible:

- Below threshold: $\mu_1 v^2/2 < 2\Delta$

  The scattering particles do not have enough kinetic energy to produce the $|\chi_2\chi_2\rangle$ state onshell. In this case, only elastic scattering in the ground state is allowed.

- Above threshold: $\mu_1 v^2/2 > 2\Delta$

  The kinetic energy of the scattering particles is larger than the mass gap between the two two-body states. Therefore, in addition to the elastic scattering, inelastic upscattering from the ground to the excited state is also possible.

The exchange of the light scalars leads to the attractive potential matrix $V(r)$,

$$V = \begin{pmatrix} V_1 & V_1 \\ V_1 & V_1 \end{pmatrix}, \quad V_1(r) = -\frac{\alpha\, e^{-m_\rho r}}{r}, \tag{4.5}$$

where $\alpha \equiv f^2/4\pi$. This attractive Yukawa potential matrix, with equal entries results due to the identical interaction strength between either pair

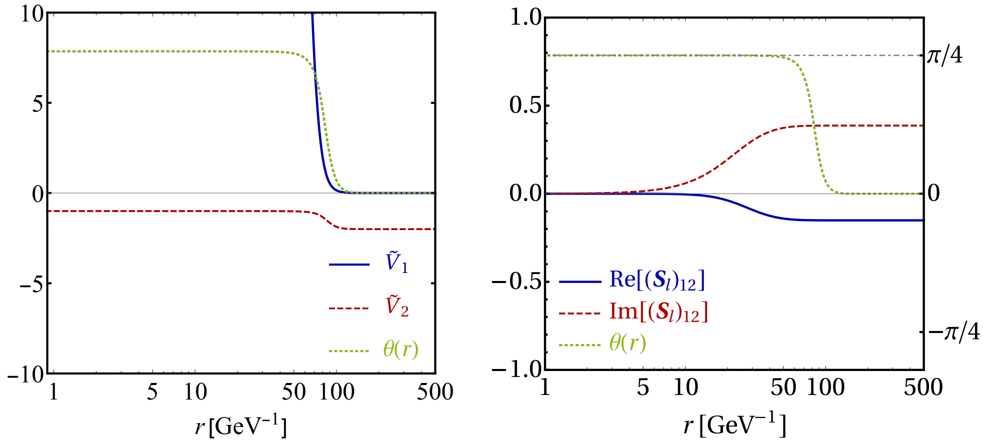

Figure 4.2: (Left) Two eigenvalues $\tilde{V}_{1,2}(r)$ of the potential matrix $V(r)$ are shown in blue solid and red dashed lines. The mixing angle $\theta(r)$ is shown as the green dotted line. (Right) The real (blue solid) and the imaginary (red dashed) parts of the off-diagonal element of the scattering function $\mathbf{S}_\ell(r)$. Figure taken form Paper II [2].

of two-body states. Variations of the DM model, such as multiple scalar mediators, vector mediator from broken dark sector gauge symmetry etc. would give rise to different potential matrices. However, the qualitative nature of our results does not depend on these variations as long as the off-diagonal interaction is nonzero.

4.2 SCATTERING CROSS SECTION

We computed the self-scattering cross sections by calculating the phase shifts for each partial wave ℓ. The definitions of total, transfer, and viscosity cross sections are given in Sec. 2.3.2. In a multilevel DM model, the cross section σ_{ab} is a matrix whose diagonal elements are the elastic cross sections in the respective state and off-diagonal elements are the inelastic cross sections of going from $|b\rangle$ to $|a\rangle$. We numerically computed the scattering cross sections following the method outlined in Ref. [125].

4.2.1 *Below threshold*

When the kinetic energy of the incoming particles is below threshold, upscattering is classically forbidden. However, the excited state can still be produced during scattering as virtual intermediate state. One could rotate the matrices by an angle $\theta(r)$ to go to the diagonal basis of the potential matrix $V(r)$ with eigenvalues,

$$\tilde{V}_{1,2} = -V_1 - \Delta \pm \sqrt{V_1^2 + \Delta^2}\,. \tag{4.6}$$

As the potentials are functions of r, the rotation angle $\theta(r)$ is also a function of r, and is given by

$$\tan 2\theta(r) = -V_1(r)/\Delta\,. \tag{4.7}$$

In the left panel of Fig. 4.2, we show the rotation angle as a function of r. We see that the states mix maximally with $\theta(r) = \pi/4$ as $r \to 0$, but the mixing decreases when $V_1(r) \lesssim 2\Delta$, finally vanishing in the large r limit. The eigenvalues of $V(r)$ never cross each other representing the fact that the system is always adiabatic. Fig. 4.2 shows only the $\ell = 0$ case, but these features are present for other partial waves as well. Because the system is adiabatic, the ground state elastic cross section can be computed by solving the rotated equations with only the potential $\tilde{V}_1(r)$.

4.2.2 *Above threshold*

As mentioned before, in above threshold scenario, upscattering is classically allowed. We shall first compute the cross sections using the *variable phase method* following Ref. [126] to gain some insight. To this end, we write the solution to Eq.(4.2) in an integral form,

$$\begin{aligned} u_\ell(r) &= \left(\frac{\mu}{k}\right)^{1/2} \mathcal{J}_\ell(kr) \\ &\quad -\frac{2\mu}{k}\int_0^r dt\,\left(\mathcal{J}_\ell(kr)\mathcal{N}_\ell(kt) - \mathcal{J}_\ell(kt)\mathcal{N}_\ell(kr)\right) V(t) u_\ell(t)\,, \end{aligned} \tag{4.8}$$

where $\mathcal{J}_\ell(x)$, $\mathcal{N}_\ell(x)$ are the Riccati-Bessel functions defined as

$$\begin{aligned} [\mathcal{J}_\ell(kr)]_{ab} &= +k_a r\, j_\ell(k_a r)\delta_{ab}, \quad \text{above threshold,} \\ &= +k_a r\, \iota_\ell(k_a r)\delta_{ab}, \quad \text{below threshold,} \\ [\mathcal{N}_\ell(kr)]_{ab} &= -k_a r\, n_\ell(k_a r)\delta_{ab}, \quad \text{above threshold,} \\ &= -k_a r\, \kappa_\ell(k_a r)\delta_{ab}, \quad \text{below threshold.} \end{aligned} \tag{4.9}$$

To isolate the change in the wavefunction owing to the presence of the potential $V(r)$, another function $\mathcal{F}_\ell(r)$ is defined as

$$\mathcal{F}_\ell(r) = \frac{1}{2}\left[1 + 2\int_0^r dt\,\mathcal{H}_\ell^{(2)}(t) V(t) u_\ell(t)\right]. \tag{4.10}$$

On substitution of this in Eq.(4.8), one gets

$$u_\ell(r) = -i\left[\mathcal{H}_\ell^{(1)}(r)\mathcal{F}_\ell(r) - \mathcal{H}_\ell^{(2)}(r)\mathcal{F}_\ell^*(r)\right]. \tag{4.11}$$

Here $\mathcal{H}_\ell^{(1),(2)} \equiv (\mu/k)^{1/2}(\mathcal{N}_\ell \pm i\mathcal{J}_\ell)$ are the free particle plane wave solutions, and the unknown functions $\mathcal{F}_\ell$ and $\mathcal{F}_\ell^*$ are the *distortions* to the plane wave solution caused by the potential. The scattering matrix function $\mathbf{S}_\ell(r)$ is defined in terms of $\mathcal{F}_\ell(r)$ as

$$\mathbf{S}_\ell(r) \equiv \mathcal{F}_\ell(r)\mathcal{F}_\ell^*(r)^{-1}. \tag{4.12}$$

This definitions of $\mathbf{S}_\ell$ is such that the large r asymptotic values of the diagonal and off-diagonal elements of it are proportional to the elastic and

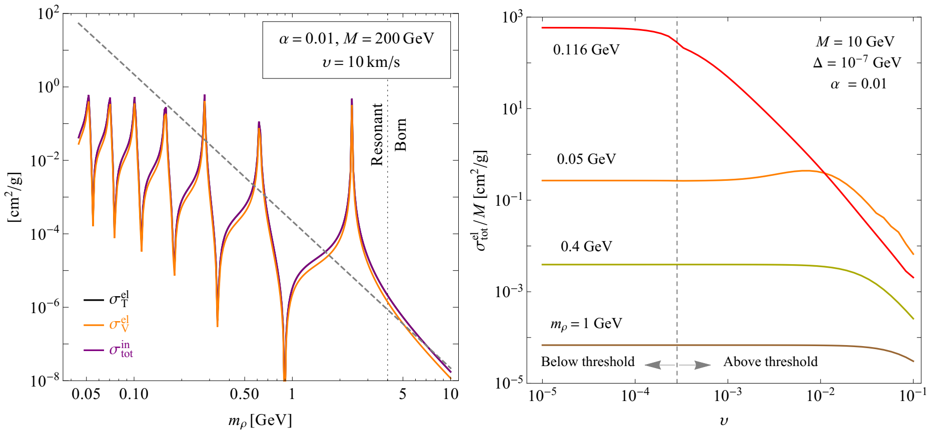

Figure 4.3: (Left) The velocity dependence of the elastic self-scattering cross-section for different values of m_ρ as indicated in the figure. (Right) The elastic transfer and viscosity cross-sections for a particular choice of the parameter values: $M = 200$ GeV, $\alpha = 0.01, v = 10\,\text{km/s}$. The grey dashed line shows the analytical estimate of the Born cross-section for the 2-level model, obtained using the one-level equivalent proposed in Paper I [1]. Figure taken from Paper II [2].

inelastic scattering cross sections, respectively. Now using Eq.(4.12) and the definition of $\mathcal{F}_\ell(r)$, the differential equation for $\mathbf{S}_\ell(r)$ can be obtained,

$$\frac{d\mathbf{S}_\ell}{dr} = i\left(\mathbf{S}_\ell \cdot \mathcal{H}_\ell^{(1)} - \mathcal{H}_\ell^{(2)}\right) \cdot V \cdot \left(\mathcal{H}_\ell^{(1)} \cdot \mathbf{S}_\ell - \mathcal{H}_\ell^{(2)}\right) . \tag{4.13}$$

This equation is to be solved with the boundary condition $\mathbf{S}_\ell(0) = \mathit{1}$.

In the right panel of Fig. 4.2, we show the r-dependence of the real and imaginary parts of the off-diagonal component of the scattering matrix function $\mathbf{S}_\ell(r)_{12}$ representing the inelastic cross section. We note that the $|\mathbf{S}_\ell(r)_{12}|$ increases from zero as one goes towards larger r starting from $r = 0$. However, $\mathbf{S}_\ell(r)_{12}$ saturates to a constant value as soon as the mixing angle vanishes beyond $r \sim 1/m_\rho$. Therefore, the adiabatic mixing between the two states induced by the off-diagonal interaction is the source of the inelastic upscattering from the ground to the excited state.

We also numerically solved Eq.(4.2) directly using `Mathematica` to compute the cross sections. In a general N-level system, the inner products of all possible 2-body states can be arranged in an $N \times N$-matrix $\Psi_\ell(r)$ [125]. The columns of $\Psi_\ell(r)$ denote the linearly independent regular solutions of the Schrödinger equation

$$\left[\frac{1}{r^2}\frac{d}{dr}\left(r^2\frac{d}{dr}\right) + k^2 - \frac{\ell(\ell+1)}{r^2} - 2\mu V(r)\right]\Psi_\ell(r) = 0\,, \tag{4.14}$$

where k and μ are two diagonal matrices with channel momenta and reduced masses. These set of equations are supplemented by the boundary conditions at $r = r_0$ as follows,

$$[\Psi_\ell(r_0)]_{ab} = r_0\,\delta_{ab}, \qquad [\Psi'_\ell(r_0)]_{ab} = (\ell+1)\,\delta_{ab}\,. \tag{4.15}$$

The initial point r_0 is chosen to be small enough so that the centrifugal term dominates over the other two terms in the differential equation. The overall normalization is irrelevant as we are interested only in the final cross-section. Numerically, we start solving the equations at $r = r_0$ and proceed towards larger r. We choose a sufficiently large $r = r_f$ where the potential becomes negligible compared to the kinetic energy term. At $r = r_f$, we match our solutions with the asymptotic solutions given below,

$$\lim_{r \to \text{large}} \Psi_\ell(r) = \mathcal{J}_\ell(kr) - \mathcal{N}_\ell(kr)\mathcal{K}_\ell\,. \tag{4.16}$$

Here $\mathcal{K}_\ell$ is the reaction matrix and

$$\begin{aligned}
[\mathcal{J}_\ell(kr)]_{ab} &= +k_a r\, j_\ell(k_a r)\delta_{ab}, \quad \text{above threshold,} \\
&= +k_a r\, \iota_\ell(k_a r)\delta_{ab}, \quad \text{below threshold,} \\
[\mathcal{N}_\ell(kr)]_{ab} &= -k_a r\, n_\ell(k_a r)\delta_{ab}, \quad \text{above threshold,} \\
&= -k_a r\, \kappa_\ell(k_a r)\delta_{ab}, \quad \text{below threshold.}
\end{aligned} \tag{4.17}$$

Here $j_\ell(x)$ and $n_\ell(x)$ denote spherical Bessel functions of first and second kinds, and $\iota_\ell(x)$ and $\kappa_\ell(x)$ are the modified spherical Bessel functions of first and second kinds, respectively. These two types of functions serve as the asymptotic forms of the wavefunction as indicated above. In the below threshold case the boundary conditions need to be changed for the excited state. In Ref. [127, 128], the author has shown that in the below threshold case, only the open-open part (the part which consists of only the open channels) of the $\mathcal{K}_\ell$ matrix contributes to the final scattering matrix though one has to solve the full system of Schrödinger equation. In this case the asymptotic wavefunctions are either exponentially growing or decaying which may cause trouble in the numerical computation (see the second line in Eq.(4.9)). It is solved by normalizing the closed channel wavefunctions and their derivatives by $\mathcal{J}_\ell$ and $\mathcal{N}_\ell$ respectively such that the new asymptotic wavefunctions become $\mathcal{J}_\ell(kr) \to 1$, $\mathcal{J}'_\ell(kr) \to \mathcal{J}'_\ell(kr)/\mathcal{J}_\ell(kr)$ and similarly for $\mathcal{N}_\ell(kr)$.

We solve for $\mathcal{K}_\ell$ from Eq.(4.16) by taking logarithmic derivative of the equation,

$$\begin{aligned}
\mathcal{K}_\ell &= [\mathcal{B}_\ell(kr_f)\mathcal{N}_\ell(kr_f) - \mathcal{N}'_\ell(kr_f)]^{-1} \\
&\quad \times [\mathcal{B}_\ell(kr_f)\mathcal{J}_\ell(kr_f) - \mathcal{J}'_\ell(kr_f)]\,,
\end{aligned} \tag{4.18}$$

where $\mathcal{B}_\ell(r) = \Psi'_\ell(r)[\Psi_\ell(r)]^{-1}$. Everywhere prime denotes derivative w.r.t. r. Once the $\mathcal{K}_\ell$ matrix is obtained, the S-matrix can computed through

$$\mathcal{S}_\ell \equiv 1 - \mathcal{T}_\ell = (1 + i\mathcal{K}_\ell)^{-1}(1 - i\mathcal{K}_\ell)\,. \tag{4.19}$$

This $\mathcal{S}_\ell$ is computed for all partial waves starting from $\ell = 0$ to $\ell_{\max}$. As stated in the text, the value of $\ell_{\max}$ depends on the initial momentum of the particles and the range of the potential. A useful lower bound on its value can be given as $\ell_{\max} \geq k/m_\rho$ for the case discussed in this paper. The final total cross-section is given by

$$\begin{aligned}
[\sigma_{\mathrm{tot}}]_{ab} &= \int d\Omega \frac{d\sigma_{ab}}{d\Omega} \\
&= \frac{1}{2k_b^2} \int d\Omega \left| \sum_\ell \frac{1}{2}(2\ell+1)(\tilde{\mathcal{T}}_\ell)_{ab} P_\ell(\cos\theta) \right|^2 \\
&= \frac{\pi}{2k_b^2} \sum_\ell (2\ell+1) |(\tilde{\mathcal{T}}_\ell)_{ab}|^2 .
\end{aligned} \tag{4.20}$$

where $(\tilde{\mathcal{T}}_\ell)_{ab} = (\mathcal{T}_\ell)_{ab} + (-1)^\ell (\mathcal{T}_\ell)_{a'b}$. Here the prime on a denotes an exchange of particles in the final 2-body DM state. Note that the last term in Eq.(4.20) is present only when the final state particles are identical. In case of distinguishable particles, this term will be absent and so will be the extra factor of 1/2. The other two quantities of interest are the transfer and viscosity cross-sections. The definition of the transfer cross-section σ_{T} is given in Eq.(2.37). Expanding the differential cross section in the partial wave basis gives

$$\begin{aligned}
[\sigma_{\mathrm{T}}]_{ab} &= \int d\Omega \frac{d\sigma_{ab}}{d\Omega}(1-\cos\theta) \\
&= \frac{\pi}{2k_b^2} \sum_\ell (\ell+1) |(\tilde{\mathcal{T}}_{\ell+1})_{ab} - (\tilde{\mathcal{T}}_\ell)_{ab}|^2 .
\end{aligned} \tag{4.21}$$

Similarly the viscosity cross-section in Eq.(2.38) is given by

$$\begin{aligned}
[\sigma_{\mathrm{V}}]_{ab} &= \int d\Omega \frac{d\sigma_{ab}}{d\Omega} \sin^2\theta \\
&= \frac{\pi}{2k_b^2} \sum_\ell \frac{(\ell+1)(\ell+2)}{(2\ell+3)} |(\tilde{\mathcal{T}}_{\ell+2})_{ab} - (\tilde{\mathcal{T}}_\ell)_{ab}|^2 .
\end{aligned} \tag{4.22}$$

The left panel in Fig. 4.3 shows the variation of the elastic cross section with mediator mass m_ρ. In the Born limit, i. e., when $\alpha M/m_\rho \ll 1$, the interaction becomes point-like and the cross section can be computed perturbatively. The transfer Born cross section given in Eq.(2.39) is restated here for the reader's convenience,

$$\sigma_{\mathrm{T}}^{\mathrm{Born}} = \frac{2\pi\beta^2}{m_\rho^2} \left[\ln\left(1+R^2\right) - \frac{R^2}{1+R^2} \right] . \tag{4.23}$$

Here, $\beta = 4\alpha m_\rho/(m_\chi v_{\mathrm{rel}}^2)$, and $R = m_\chi v_{\mathrm{rel}}/m_\rho$. Note that although ours is a two-level scattering system, an analytic expression of the Born cross-section is obtained by the substitution $\alpha \to 2\alpha$, or equivalently $\beta \to 2\beta$. This follows from the approximately particle exchange symmetry as discussed in Sec. 3.3 in the previous chapter. In the limit of small Δ, the states $|\chi_1\chi_1\rangle$ and $|\chi_2\chi_2\rangle$ are approximately identical and related to each other through the relation $|\chi_2\chi_2\rangle \simeq (-1)^{\ell+s}|\chi_1\chi_1\rangle$ with s being the total spin of the two-body state [1]. The Born cross section is shown in the gray dashed line. When $\alpha M/m_\rho \gtrsim 1$, virtual bound state formation takes place during

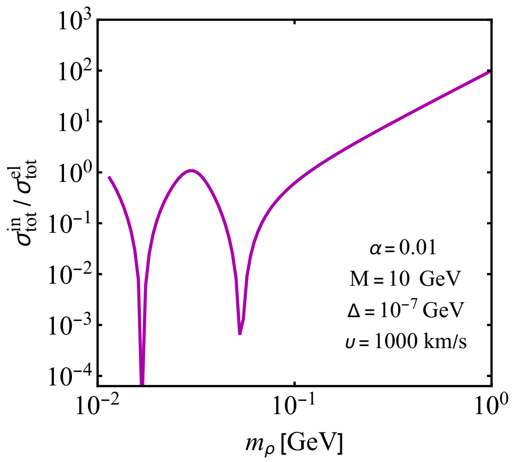

Figure 4.4: The ratio of the inelatic to elastic scattering cross sections with purely off-diagonal interactions. Figure taken from Paper II [2].

scattering. This is known as the resonant region. The resonance points can again be obtained from Eq.(2.32) with the replacement $\alpha \to 2\alpha$.

We show the elastic cross section σ_{el} as a function of velocity for various values of m_ρ in the right panel of Fig. 4.3. For large velocity, σ_{el} goes as $\sigma_{\mathrm{el}} \sim 1/v^4$ as expected in Rutherford scattering, but it saturates to a constant value depending on m_ρ in the small velocity limit. As m_ρ is increased from 0.05 to 1 GeV, the cross section undergoes a resonance due to virtual bound state formation.

In most of the parameter space, we found that the inelastic cross section is comparable to the elastic cross section. This is a direct result of the fact that the potential matrix has equal diagonal and off-diagonal entries. The large off-diagonal interaction leads to maximal mixing between the states resulting in large inelastic scattering as discussed previously. When the diagonal potentials are weaker than the off-diagonal potentials, these two cross-sections can differ by several orders of magnitude. An example of such a scenario is a two-component Majorana DM model, where the DM particles are charged under a broken $U(1)$ gauge symmetry [83, 129]. The conserved currents are $\bar{\chi}_1\gamma^\mu\chi_2$ and $\bar{\chi}_2\gamma^\mu\chi_1$. Hence elastic scattering $\chi_{1,2}\chi_{1,2} \to \chi_{1,2}\chi_{1,2}$ is not possible at tree level, even though inelastic scattering $\chi_{1,2}\chi_{1,2} \to \chi_{2,1}\chi_{2,1}$ can take place through an exchange of a gauge particle. The lowest order elastic process involves at least one loop implying that, in the Born limit, elastic scattering is loop-suppressed. However, in the resonant and classical regime, nonperturbative effects will be important, and both elastic and inelastic cross-sections will be comparable (see Fig. 4.4). However, depending on the parameter choice, one may dominate over the other.

4.3 SIGNATURES OF INELASTIC SCATTERING

The energy loss by the DM particles through inelastic scattering induced decay will provide a heat dissipation mechanism for DM halos. An estimate of the timescale for the upscattering rate in a typical galaxy cluster sized DM halo, assuming prompt decay of the excited state, is

$$t_{\rm up} \simeq 10^{12}\,{\rm yrs}\,\frac{10^4\,{\rm M}_\odot/{\rm kpc}^3}{\rho}\,\frac{1\,{\rm cm}^2/{\rm g}}{\sigma_{\rm in}/m_\chi}\,\frac{10^3\,{\rm km/s}}{v}\,. \tag{4.24}$$

We choose DM velocity to be $\mathcal{O}(1000)$ km/s so that the upscattering is kinematically allowed. Clearly $t_{\rm up}$ is a few orders of magnitude larger than the age of the Universe. Moreover, upscattering can take place only inside collapsed DM structures or halos which are around for a much shorter time (only since nonlinear structures started forming). Therefore the dissipation mechanism cannot possibly cause a too large effect. We now discuss two possible effects due to inelastic scattering.

4.3.1 *Halo cooling*

If the $\chi_1 - \rho$ scattering cross-section is small, then these light mediator particles will not be trapped inside and escape the halo. They will carry away energy from the halo in the form of radiation which therefore cools the halo at a certain rate. Large upscattering requires the colliding DM particles to be energetic enough so that sufficient phase space is available for the excited state. For example, DM of mass 10 GeV with mass gap $\Delta = 1$ MeV has a velocity threshold of about 1000 km/s. Thus, its effect will be important in astrophysical objects with large DM velocity dispersions, e. g., in large galaxies and galaxy clusters.

A thorough analysis of the effect of such energy dissipation on the structure and dynamics of DM halo does not exist in the literature. We shall try to gain a qualitative understanding from the response of DM halos for similar cooling processes from the baryonic matter– gas, dust, stars etc. After falling towards the center, the baryons interact with each other and condense into lower energy states. In the process, they dissipate away a large amount of energy in the form of radiation which escapes the halo. The less energetic baryons then condense and undergo further infall towards the center. The baryon density eventually comes to dominate the energy density near the center, and affects the DM profile. The analytical estimations of this effect have been worked out using adiabatic contraction approximation [130]. In this approximation, the DM particle orbits are assumed to be circular or nearly circular and the total mass enclosed by the orbit is assumed to be changing very slowly compared to the orbital time period of the DM particle. In this adiabatic regime, the invariance of $\oint pdq$ implies $M(r)r =$ constant, where $M(r)$ is the total mass enclosed inside the orbit of radius r. Using this invariance, an analytic estimate has been obtained that matches fairly well with computer simulation results [130, 131]. The main effect is the steepening of the DM profile near the center forming a denser core. As more baryons fall towards the center, the gravitational potential well becomes deeper and more DM particles are attracted inward, thus increasing the slope of the central density profile.

The dark sector 'heat' dissipation or cooling mechanism through an upscattering and a subsequent decay of the excited state is mostly independent of baryonic cooling process. Hence the effect of halo cooling will presumably be more prominent in this scenario and one would predict more diversity in DM halo structure.

The rate of this new dissipation mechanism will mainly be dictated by the upscattering rate as the the decay is very fast relative to other timescales, and hence can be assumed to be prompt. Here we shall give a rough estimate of the of energy loss rate. In the limit of nonrelativistic DM and $\Delta \ll m_\chi$, the net kinetic energy lost per particle is approximately $\sim \Delta$. The upscattered χ_2 particles will decay and produce lighter particles with some amount of kinetic energy from the phase space available. One can estimate the leading order contribution to this energy gain to be $\mathcal{O}(\Delta^2/m_\chi^2)$ and $\mathcal{O}(v_2^2\Delta/m_\chi)$, where v_2 is velocity of the upscattered χ_2 particles prior to decay. Therefore for all relevant parameter values, the gain in the kinetic energy from the decay is small compared to the energy loss from the upscattering. The requirement for the upscattering and the decay to happen constrains the parameter space as

$$m_\chi v^2/2 > \Delta > m_\rho \,. \tag{4.25}$$

For simplicity, we shall assume that all light scalars generated from the decays leave the halo.

In a halo, the average rate of energy loss from a shell of radius r and width dr, is given by

$$4\pi r^2 dr\,\Gamma_{\rm up}(r) n_\chi(r)\,2\Delta = 4\pi r^2 dr\,\frac{2\Delta}{m_\chi}\frac{\sigma_{\rm in}}{m_\chi}\,v\rho(r)^2\,. \tag{4.26}$$

The radial dependence of DM velocity could be estimated from simple Newtonian dynamics. It peaks around the scale radius of the halo with an NFW density profile defined in Eq.(1.14). The individual DM velocities at a given position is assumed to follow a Maxwell-Boltzmann (MB) distribution characterized by a virial velocity dispersion $\bar{v}(r)$. In a fully virialized halo, the high energetic DM particles mostly reside at the outer edge of the halo. The halo cooling rate will be given by a convolution over the DM velocity distribution

$$\frac{dE}{dt} = 4\pi r^2 dr\,\frac{2\Delta}{m_\chi}\rho(r)^2\int_0^\infty \frac{\sigma_{\rm in}}{m_\chi}\bar{v}(r) f(v) dv\,, \tag{4.27}$$

where we take $f(v)$ to be approximated by a Maxwell distribution $f_{\rm MB}(v) = 4\pi v^2 \exp\left[-v^2/\bar{v}(r)^2\right]/(\sqrt{\pi}\bar{v}(r))^3$. Here we note that the velocity distribution $f(v)$ also depends on radial distance r through $\bar{v}(r)$.

An approximate radial dependence of the cooling rate dE/dt for a halo of the size of that of the Virgo cluster is shown in Fig. 4.5. The profile was taken to be an NFW profile with a scale radius $r_s = 560$ kpc and density $\rho_s = 3.2\times10^5\,\mathrm{M}_\odot/\mathrm{kpc}^3$. For simplicity the inelastic cross-section is taken to be velocity-independent constant $\sigma_{\rm in}/m_\chi = 1\,\mathrm{cm}^2/\mathrm{g}$. The cooling rate shows a strong radial dependence and is largest near the virial radius.

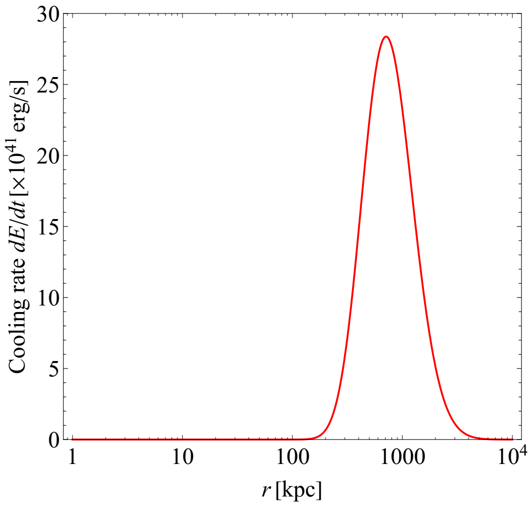

Figure 4.5: The radial dependence of the cooling rate dE/dt (see Eq.(4.27)) of a Virgo cluster-size halo with a scale radius $r_s = 560$ kpc and density $\rho_s = 3.2 \times 10^5\,\mathrm{M}_\odot/\mathrm{kpc}^3$. The chosen DM parameters are $m_\chi = 10$ GeV, $\Delta = 10^{-4}$ GeV, and $\sigma_{\rm in}/m_\chi = 1\,\mathrm{cm}^2/\mathrm{g}$. Figure taken from Paper II [2].

This feature arises from the competition of the two factors, namely the density $\rho(r)$ and velocity dispersion $\bar{v}(r)$ in Eq.(4.27). The density increases towards the center, but average velocity increases towards larger radius. Hence the cooling rate is maximum near r_s.

This cooling rate can be compared with the energy inflow from the gravo-thermal collapse of the DM particles and due to the heat diffusion through elastic self-scattering. The gravitational collapse brings faster (hotter) particles from the outer region of the halo to the cooler inner part. And the scattering between the particles help diffuse the kinetic energy from the hotter particles to the relatively colder ones. The process of gravo-thermal collapse can be modelled following the Refs. [132, 133]. The negative specific heat of a halo after virialization leads to this collapse. If we treat the DM particles as a fluid, the inward heat-flow at some radius r is given by

$$\frac{L}{4\pi r^2} = -\frac{3}{2} abv\sigma \left(a\sigma^2 + \frac{b}{C}\frac{4\pi G}{\rho v^2} \right)^{-1} \frac{\partial v^2}{\partial r}\,. \tag{4.28}$$

Here the two terms within parenthesis on the RHS correspond to two different *mean free path* regimes. The first term describes the *hard sphere scattering* with the dimensionless coefficient $a = \sqrt{16/\pi}$. The second term describes the *short mean free path* regime which is proportional to the gravitational constant and the numbers $b = 25\sqrt{\pi}/32$ and $C \approx 0.75$. Typical values of this heat inflow rate are 2-3 orders of magnitude larger than the cooling rate discussed above. However, in models with large inelastic cross section than the elastic one, this halo cooling can be efficient enough to distort the halo.

Upscattering and decay do not start abruptly, but are rather continuous processes which will be present during the virialization process of the halo. At the initial epoch of structure formation the DM particles are highly nonrelativistic and there will be no dissipation. After DM falls towards the centers of the potential wells, acquires more energy and inelastic collisions become possible, leading to cooling. From Eq.(4.24) it is clear that the inelastic scattering is a rather slow process and the halo will virialize at a faster rate than the dissipation. As a result, subsequent changes in the halo shapes is expected to be continuous and not episodic. A more detailed study of the effect of this new cooling mechanism requires an N-body simulation with this extra energy loss implemented in the dark sector [134]. Recently two groups have done N-body simulations with inelastic dark sector, and have found inelastic scattering to be more efficient in modifying halo shapes than the elastic scattering [135, 136].

A similar halo cooling mechanism was considered in Ref. [85] in the context of an atomic DM model. There neutral atomic dark hydrogen makes the DM abundance in the present Universe. The hyperfine splitting in the ground state of the dark atom leads to inelasticity in the system and the excited state decays to the ground state emitting massless dark photons. The masslessness of the dark photon implies that this cooling mechanism is more important for smaller halos because of their lower gravitational binding energy. On the contrary, in our case the particle ρ is massive. Hence the cooling mechanism shuts off for small mass halos where the DM particles do not have enough energy to upscatter, and the dissipation arises mainly in large galaxies or clusters. Note that the details of the particle physics model do not affect the radial dependence shown in Fig. 4.5, and all such details are encapsulated into the velocity dependence of the cross-section that determines this feature.

4.3.2 *Additional drag force*

Upper limit on DM self-scattering can also be obtained from particle evaporation during collision of clusters and the movement of smaller dwarf-sized halos through larger halos [137, 138]. SIDM particles experience collisions in mergers clusters, whereas the stellar components of the objects will move freely without any appreciable friction. If the momentum transfer in a DM scattering is such that the final velocity is larger than the escape velocity of the parent halo then the particles would leave the halo and would lead to *DM evaporation* from the halo. The existing observations from colliding clusters put strong constraint on this process yielding an upper bound on the DM self-scattering. An estimate of the scattering rate can be obtained following the analysis in Ref. [137], in the limit of long-range interaction (as the hierarchy $m_\chi v^2/2 > \Delta > m_\rho$ is easy to satisfy with smaller value of m_ρ even at cluster size scale). In Ref. [137], the cumulative evaporation rate was shown to be more important than the immediate evaporation when DM has long range self-interaction. The cumulative evaporation rate is

$$R_{\rm cml} = \frac{\eta \alpha^2 \rho_\chi}{m_\chi^3 v_0^3} \left[1 - 2 \ln \left(\frac{\theta_{\rm min}}{2} \right) \right] . \tag{4.29}$$

Here v_0 is the relative velocity between the two colliding clusters, and $\rho_\varnothing$ is the DM density in the bigger halo. The parameter $\theta_{\rm min}$ encodes the screening of the long range interaction potential and regulates the forward scattering divergence which is typical in such cases. As a result of the DM evaporation, the halos experience a drag force given by

$$\begin{aligned}\frac{F_{\rm drag}}{m_\chi} &= v_0 R_{\rm cml} \\ &= \frac{\eta\alpha^2\rho_\chi}{m_\chi^3 v_0^2}\left[1-2\ln\left(\frac{\theta_{\rm min}}{2}\right)\right] = \frac{\tilde{\sigma}\rho_\chi}{4m_\chi v_0^2}\,,\end{aligned} \tag{4.30}$$

where η is an $\mathcal{O}(1)$ numerical factor depending on the particle nature of the mediator. In the last equality, $\tilde{\sigma}$ is defined as

$$\frac{\tilde{\sigma}}{m_\chi} \equiv \frac{4\eta\alpha^2}{m_\chi^3}\left[1-2\ln\left(\frac{\theta_{\rm min}}{2}\right)\right]. \tag{4.31}$$

The existing bound on $\tilde{\sigma}$ from the abundance of dwarfs in our MW halo is very strong, $\tilde{\sigma}/m_\chi \lesssim 10^{-11}\,{\rm cm}^2/{\rm g}$ [137].

For two-level DM, two distinct cases may arise. Firstly the usual evaporation of DM particles is still possible in this model, and has contributions from both elastic and inelastic scattering. If the velocities of the scattered particles are larger than the escape velocities then they can escape the halo and would cause dynamical friction between the halos. Secondly, inelastic scattering and subsequent decay provides an additional way for energy dissipation and gives an additional contribution to the dynamical friction or the drag force. For simplicity, if we assume that all DM particles are moving at the same velocity v_0, then $n_\chi\sigma_{\rm in}v_0$ is the upscattering rate per unit time. After each upscattering and decay event, two light particles escape the halo taking away an amount of energy which is roughly $\langle E_{\rm decay}\rangle \simeq 2\Delta$. Therefore, the halo loses energy at a rate

$$\frac{dE}{dt} = \langle E_{\rm decay}\rangle n_\chi \sigma_{\rm in} v_0\,. \tag{4.32}$$

The resulting drag force per unit DM mass (or deceleration) due to this energy loss is given by

$$\frac{F_{\rm drag}^{\rm decay}}{m_\chi} = \frac{1}{m_\chi v_0}\frac{dE}{dt} = \frac{\langle E_{\rm decay}\rangle}{m_\chi}\frac{\rho_\chi\sigma_{\rm in}}{m_\chi}\,. \tag{4.33}$$

The net drag force acting between the halos is given by

$$\begin{aligned}\frac{F_{\rm drag}}{m_\chi} &= v_0 R_{\rm cml} + \frac{\langle E_{\rm decay}\rangle}{m_\chi}\frac{\rho_\chi\sigma_{\rm in}}{m_\chi} \\ &= \frac{(\tilde{\sigma}_{\rm el}+\tilde{\sigma}_{\rm in})\rho_\chi}{4m_\chi v_0^2} + \frac{2\Delta}{m_\chi}\frac{\rho_\chi\sigma_{\rm in}}{m_\chi}\,.\end{aligned} \tag{4.34}$$

The first term on the r.h.s above represents the cumulative evaporation rate, due to elastic and inelastic processes that are approximately equal across a large portion of the parameter space. We neglect the tiny velocity gain of χ_1 from the decay as we have seen it to be of even smaller order of magnitude in the previous subsection. The second term corresponds to the new dissipation mechanism from upscattering and decay. The quantity $\langle E_{\rm decay}\rangle$ denotes the energy loss rate averaged over the phase space of the final particles which, in the last equality, has been approximated to $\langle E_{\rm decay}\rangle \simeq 2\Delta$. For simplicity here we have assumed that all DM particles in the incident halo have velocity v_0. Of course a more careful analysis would require averaging over a Maxwellian distribution characterized by a velocity dispersion v_0.

The relative size of the new term in Eq.(4.34) compared to the old term is given by $\sim 4v_0^2\Delta/m_\chi \simeq 10^{-8}$ for $m_\chi = 10$ GeV, $\Delta = 1$ MeV and $v_0 = 1000\,\mathrm{km/s}$, and assuming $\sigma_{\rm in} \simeq \tilde{\sigma}_{\rm in}$. The parametric smallness of the new drag force term may be traced back to the smallness of the mediator mass. A light particle-mediated interaction has a negative power dependence on DM velocity, and is enhanced at small velocities, whereas the new term is essentially velocity independent. This velocity dependence may be useful to extract the impact of the second term, relative to the larger first term.

There may be other signatures of this energy loss process. For example, just as the baryonic energy loss processes like Compton scattering and bremsstrahlung are responsible for the collapse of the ordinary matter into disk-like structures forming the galaxies, for two-level DM, upscattering and subsequent decay processes help DM lose energy and can lead to the formation of a rotating dark disk in DM halo [139–144]. As another signature, the authors in Ref. [145], observed a discrepancy between the predicted positions of the splashback radii (see [146–148]) of cluster-size halos in simulation and the observational data [149, 150]. This mismatch could in principle be addressed by this energy dissipation mechanism through DM inelastic scattering.

4.4 SUMMARY & CONCLUSIONS

In this chapter, we studied the self-scattering of a two-level DM model. The off-diagonal interaction leads to inelastic scattering of a pair of DM particles from the ground state to the excited state, in addition to the ordinary elastic scattering.

If the incoming energy of the particles is below threshold, the excited state is not produced as physical states. Nevertheless, those states are produced offshell in the intermediate steps of the scattering and can affect even the elastic scattering cross-section. It was shown that the equations in this case, can be rotated to a new basis where the potential matrix becomes diagonal, and because of adiabaticity can be solved as a single state system with an appropriate potential.

When the incoming particles are above threshold, inelastic scattering may also take place. We showed that in a large part of the parameter space, the inelastic cross-section is comparable to its elastic counterpart. This large inelasticity is a result of the maximal adiabatic mixing between the two states. We have also identified the Born and resonant regions in the relevant parameter space, and an estimate for the resonance condition has been given using a mapping of the two-level system to an equivalent one-level equation.

The off-diagonal interaction between the DM states allows the heavier state to decay to the ground state emitting a mediator. The upscattering and subsequent decay thus provides a mechanism for energy dissipation in DM halos. Assuming the decay to be prompt, the rate of the upscattering induced decay is given by the inelastic scattering rate which we computed to be 1-2 orders of magnitudes larger than the age of the Universe. Therefore, the DM halos can not condense into smaller halos via this mechanism. Rather, the inelastic process takes place only in larger objects and is effective only after the DM density becomes large enough at the centers of those objects. We compared this cooling rate with the heating due to ordinary elastic scattering and found that in some regions of the parameter space, the cooling rate could be a large fraction of the heating rate. We expect that this will leave an observable imprint on DM halo formation and evolution which can be only be probed by an N-body simulation incorporating this dissipative feature.

The same dissipation gives rise to an additional drag force between two colliding halos or for a small halos drifting through a larger one. When two halos collide with each other, the self-interacting DM particles scatter with each other and lose energy by emitting the light scalars. This energy loss can be interpreted as a new drag force acting between the halos. We calculated an analytical expression for this new drag force and found that it is small relative to the other contribution from ordinary scattering, but has a distinctive velocity independence unlike the usual drag force.

5 LATE FORMING BALLISTIC DARK MATTER

Almost all particle physics models of DM predict that DM was not cold at very early time. In many of these models, it is thought that when the temperature of the Universe was high, the DM particles were relativistic and interacted with other particles. As the Universe expanded, the DM particles cooled down, and eventually became nonrelativistic and stopped interacting with other particles. In typical WIMP-like scenarios, this happens when the temperature falls below the DM mass $T \sim m_\chi/3$. Therefore for DM mass in the MeV to TeV range, it becomes cold at very early time or high redshift $z \sim 10^9 - 10^{12}$. However, several other models predict that the formation of *cold* DM could have been relatively *late*, for example, after $z = 10^9$ [93, 94, 151–160]. A question then naturally arises, *how late could CDM have formed in our Universe?* To answer this question in a model-independent way, we assume an *effective macroscopic* setup of late-forming ballistic dark matter (BDM), and study on the cosmological observations. Here the term *ballistic* refers to the fact that the DM inherits large peculiar velocities from the acoustic oscillations in the relativistic collisional phase.

In this chapter, we shall first review cosmological linear perturbation theory which will be required for our study, and then describe and explain the novel effects due to late-formation of CDM. This chapter is based on Paper III [3].

5.1 COSMOLOGICAL PERTURBATION THEORY

The Universe is homogeneous and isotropic at large scales, but at the same time it abounds with structures like galaxies. This tell us that the Universe is, in fact, inhomogeneous and anisotropic at small enough length scales. However, the fluctuations of the metric from the smooth FLRW background, or perturbations in the energy density were very small at early time, e. g., during recombination. The observation of the CMB radiation in the sky have confirmed that the fluctuations in the temperature, and hence, in density of the CMB photons are of the order of 10^{-5}. The smallness of the fluctuations lets us use linear perturbation theory for the study of CMB physics and large scale structure formation. Here we shall give a brief outline of this theory following Ma & Bertschinger [161].

To begin with, we consider the perturbed, flat (i. e., $k = 0$ in Eq.(1.1)) FLRW metric (see Eq.(1.3)) in the *conformal Newtonian gauge* as follows[1],

$$ds^2 = a^2(\tau)\left[-(1+2\psi)d\tau^2 + (1+2\phi)dx^i dx^i\right] . \qquad (5.1)$$

1 Throughout this chapter, we follow the 'mostly positive' sign convention $g_{\mu\nu} = (-1, +1, +1, +1)$ for the Minkowski metric. For the metric perturbations, we follow the sign convention in Ref. [15]

The quantities $\psi(\mathbf{r},\tau)$ and $\phi(\mathbf{r},\tau)$ include only the scalar modes of the metric perturbations. The vector and tensor perturbations are not included in this gauge. It is suggestive to take spatial Fourier transform of the fluctuations to take the advantage of the linearity of the theory.

$$A(\mathbf{r},t) = \int \frac{d^3k}{(2\pi)^3} e^{-i\mathbf{k}\cdot\mathbf{r}} \tilde{A}(\mathbf{k},t)\,. \tag{5.2}$$

Each spatial derivative that appears in the evolution equations of various quantities yields a factor of the wavenumber k_i for a particular Fourier mode: $\partial_i \rightarrow k_i$. We will drop the tilde from the Fourier transformed quantities henceforth to simplify notation.

It is straightforward to derive the Einstein equation from Eq.(5.1). The zeroth order part of it gives the Friedmann equations (Eq.(1.7)) describing the evolution of the homogeneous FLRW Universe. The next leading order terms gives the following equations of motion of ψ and ϕ,

$$\begin{aligned}
&k^2\phi + 3\frac{\dot{a}}{a}\left(\dot{\phi} - \frac{\dot{a}}{a}\psi\right) = 4\pi G a^2 \bar{\rho}\delta\,,\\
&k^2\left(\dot{\phi} - \frac{\dot{a}}{a}\psi\right) = -4\pi G a^2(\bar{\rho}+\bar{p})\theta\,,\\
&\ddot{\phi} + \frac{\dot{a}}{a}(2\dot{\phi} - \dot{\psi}) - \left(2\frac{\ddot{a}}{a} - \frac{\dot{a}^2}{a^2}\right) + \frac{k^2}{3}(\phi+\psi) = -\frac{4\pi}{3} G a^2 \delta T^i_i\,,\\
&k^2(\phi+\psi) = -12\pi G a^2(\bar{\rho}+\bar{p})\sigma\,.
\end{aligned} \tag{5.3}$$

Here we have defined the following quantities

$$\delta = -\delta T^0_0/\bar{\rho}, \quad (\bar{\rho}+\bar{p})\theta \equiv ik^i\delta T^0_i, \quad (\bar{\rho}+\bar{p})\sigma \equiv -(\hat{k}^i\hat{k}^j - \frac{1}{3}\delta^{ij})\Sigma^i_j\,, \tag{5.4}$$

where θ is known as the velocity perturbation, σ is the anisotropic stress, and $\Sigma^i_j \equiv T^i_j - \delta^i_j T^k_k$ is the traceless part of T^i_j.

These set of equations are to be closed with the equations of motion for the perturbations in density δ, velocity θ, and anisotropic stress σ. As a perfect fluid can be completely described by density and pressure, the anisotropic stress vanishes, and δ and θ are the only perturbation variables. Their equations of motion can be found easily by using the stress-energy conservation $T^{\mu\nu}{}_{;\nu} = 0$. This results in

$$\begin{aligned}
\dot{\delta} &= -(1+w)(\theta + 3\dot{\phi}) - 3\frac{\dot{a}}{a}\left(c_s^2 - w\right)\delta\,,\\
\dot{\theta} &= -\frac{\dot{a}}{a}(1-3w)\theta - \frac{\dot{w}}{1+w}\theta + \frac{c_s^2}{1+w}k^2\delta + k^2\psi\,.
\end{aligned} \tag{5.5}$$

Here w is the EoS, c_s is the adiabatic sound speed in the fluid.

They can be obtained from the perturbations in a general phase space distribution $f(x^i, q^j, \tau)$ of the species defined through

$$\int d^3x d^3q\, f(x^i, q^j, \tau)\,(1-3\phi) = N\,, \tag{5.6}$$

where q^j ($= ap^j$) is the comoving 3-momentum, N is the total number of particles of mass m. The extra $(1-3\phi)$ factor is due to the fact that q^i is the comoving momentum, and not the canonically conjugate variable of x^i. The perturbation to $f(x^i, q^j, \tau)$ is defined as

$$f(x^i, q^j, \tau) = f_0(q)\left[1 + \Psi(x^i, q^j, \tau)\right] . \tag{5.7}$$

Here $q^j = qn^j$, n^j being the unit vector in the direction of q^j, and $f_0(q)$ is the Bose or Fermi distribution depending on the particle statistics. With this definition, the perturbed stress-energy tensor reads

$$\begin{aligned} T^0_0 &= -a^{-4}\int d^3q\sqrt{q^2+a^2m^2}f_0(q)(1+\Psi)\,, \\ T^0_i &= a^{-4}\int d^3q\, qn_i f_0(q)\Psi\,, \\ T^i_j &= a^{-4}\int d^3q\,\frac{q^2 n_i n_j}{\sqrt{q^2+a^2m^2}}f_0(q)(1+\Psi)\,. \end{aligned} \tag{5.8}$$

For massless species, like photons, massless neutrinos, it is advantageous to define a momentum-integrated function $F(\mathbf{k}, \hat{n}, \tau)$ as

$$F(\mathbf{k}, \hat{n}, \tau) \equiv \frac{\int dqq^2\, qf_0(q)\Psi}{\int dqq^2\, qf_0(q)} \equiv \sum_{\ell=0}^{\infty}(-i)^\ell(2\ell+1)F_\ell(\mathbf{k},\tau)P_\ell(\hat{k}\cdot\hat{n})\,. \tag{5.9}$$

In terms of $F_\ell(\mathbf{k}, \tau)$, the perturbations read

$$\begin{aligned} \delta &= \frac{1}{4\pi}\int d\Omega F(\mathbf{k},\hat{n},\tau) = F_0\,, \\ \theta &= \frac{3i}{16\pi}\int d\Omega(\mathbf{k}\cdot\hat{n})F(\mathbf{k},\hat{n},\tau) = \frac{3}{4}kF_1\,, \\ \sigma &= -\frac{3}{16\pi}\int d\Omega\left[(\mathbf{k}\cdot\hat{n})^2 - \frac{1}{3}\right]F(\mathbf{k},\hat{n},\tau) = \frac{1}{2}F_2\,, \end{aligned} \tag{5.10}$$

for EoS $w = 1/3$ [2]. This series of different moments of $F(\mathbf{k}, \hat{n}, \tau)$ is sometimes called as the Boltzmann hierarchy. All species except the massive neutrinos can be described using the momentum-integrated perturbations δ, θ, σ and higher F_ℓs.

The Boltzmann equation for a species with distribution function $f(x^i, q, n^j, \tau)$ is

$$\frac{\partial f}{\partial \tau} + \frac{dx^i}{d\tau}\frac{\partial f}{\partial x^i} + \frac{dq}{d\tau}\frac{\partial f}{\partial q} + \frac{dn^j}{d\tau}\frac{\partial f}{\partial n^j} = \left(\frac{\partial f}{\partial \tau}\right)_C . \tag{5.12}$$

2 For generic EoS w, θ and σ equations change into

$$\begin{aligned} \theta &= \frac{i}{4\pi(1+w)}\int d\Omega(\mathbf{k}\cdot\hat{n})F(\mathbf{k},\hat{n},\tau) = \frac{1}{(1+w)}kF_1\,, \\ \sigma &= -\frac{1}{4\pi(1+w)}\int d\Omega\left[(\mathbf{k}\cdot\hat{n})^2 - \frac{1}{3}\right]F(\mathbf{k},\hat{n},\tau) = \frac{2}{3(1+w)}F_2\,, \end{aligned} \tag{5.11}$$

respectively.

The R.H.S. is the collision term that depends on the interactions with other particles. Finally, the perturbation evolution equations can be obtained by substituting Eq.(5.7) into Eq.(5.12), performing the integral over q, and using the definition of $F(\mathbf{k}, \hat{n}, \tau)$ from Eq.(5.9).

Because CDM is nonrelativistic during all epochs of interest, they can be described as pressureless perfect fluid with $w = 0$, $F_{\ell\geq 2} = 0$, and their using only density and velocity perturbations. For CDM,

$$\dot{\delta}_c = -\theta_c - 3\dot{\phi}, \quad \dot{\theta}_c = -\frac{\dot{a}}{a}\theta_c + k^2\psi\,. \tag{5.13}$$

These equations are identical to Eq.(5.5) with $w = 0$ which are obtained from the stress-energy conservation.

Massless neutrinos do not form a perfect fluid. They have anisotropic stress σ_ν and all higher mode perturbations,

$$\begin{aligned}
\dot{\delta}_\nu &= -\frac{4}{3}\theta_\nu - 4\dot{\phi}\,, \\
\dot{\theta}_\nu &= k^2\left(\frac{1}{4}\delta_\nu - \sigma_\nu\right) + k^2\psi\,, \\
\dot{F}_{\nu\ell} &= \frac{k}{2\ell+1}\left[\ell F_{\nu(\ell-1)} - (\ell+1)F_{\nu(\ell+1)}\right], \quad \ell \geq 2\,.
\end{aligned} \tag{5.14}$$

Photons and baryons were strongly coupled via Thomson scattering until recombination. Their distribution functions are affected by the Thomson scattering through the collision term in Eq.(5.12). Additionally, photons have two polarizations which are affected differently by the anisotropic Thomson scattering. The Boltzmann equations are

$$\begin{aligned}
\dot{\delta}_\gamma =& -\frac{4}{3}\theta_\gamma - 4\dot{\phi}\,, \\
\dot{\theta}_\gamma =& \; k^2\left(\frac{1}{4}\delta_\gamma - \sigma_\gamma\right) + k^2\psi + an_e\sigma_T(\theta_b - \theta_\gamma)\,, \\
\dot{F}_{\gamma 2} =& \; 2\dot{\sigma}_\gamma = \frac{8}{15}\theta_\gamma - \frac{3}{5}kF_{\gamma 3} - \frac{9}{5}an_e\sigma_T\sigma_\gamma + \frac{1}{10}an_e\sigma_T(G_{\gamma 0} + G_{\gamma 2})\,, \\
\dot{F}_{\gamma\ell} =& \; \frac{k}{2\ell+1}\left[\ell F_{\gamma(\ell-1)} - (\ell+1)F_{\gamma(\ell+1)}\right] - an_e\sigma_T F_{\gamma\ell}\,, \quad \ell \geq 3\,, \\
\dot{G}_{\gamma\ell} =& \; \frac{k}{2\ell+1}\left[\ell G_{\gamma(\ell-1)} - (\ell+1)G_{\gamma(\ell+1)}\right] \\
& - an_e\sigma_T\left[-G_{\gamma\ell} + \frac{1}{2}(F_{\gamma 2} + G_{\gamma 0} + G_{\gamma 2})\left(\delta_{\ell 0} + \frac{\delta_{\ell 2}}{5}\right)\right].
\end{aligned} \tag{5.15}$$

Here σ_T is the Thomson cross section, n_e is the electron number density, $F_{\gamma\ell}$ and $G_{\gamma\ell}$ are the momentum-averaged perturbations with the sum and difference of two perpendicular polarizations, respectively.

The baryons are nonrelativistic during the epochs of our interest. Therefore, their perturbations equations are similar to that of CDM except the acoustic term $c_s^2 k^2 \delta_b$ (c_s is the sound speed in the photon-baryon fluid and

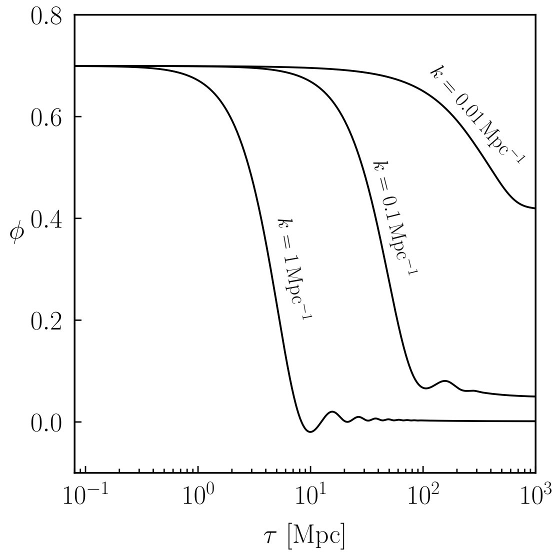

Figure 5.1: The evolution of the metric perturbation ϕ for three different modes $k = 0.01, 0.1, 1\,\mathrm{Mpc}^{-1}$.

is a function of the baryon temperature T_b), and the interaction term with photon velocity perturbation θ_γ. The equations are

$$\begin{aligned} \dot{\delta}_b &= -\theta_b - 3\dot{\phi}\,, \\ \dot{\theta}_b &= -\frac{\dot{a}}{a}\theta_b + c_s^2 k^2 \delta_b + \frac{4\bar{\rho}_\gamma}{3\bar{\rho}_b} a n_e \sigma_T (\theta_\gamma - \theta_b) + k^2 \psi\,. \end{aligned} \tag{5.16}$$

The perturbation equations for the metric and all species are to be solved numerically starting with some initial condition. The initial point in time is taken to be when a particular mode is still outside horizon, i. e., $k\tau \ll 1$. The initial conditions for the metric perturbations are set by the curvature perturbation created by some mechanism (e. g., inflation [162–164]) at super-horizon scale. The initial conditions for the density perturbations can be obtained by solving their equations in the small $k\tau$ limit. We shall not discuss the derivations of the initial conditions here. See Ref. [161] for details. The equations can be solved using any of the publicly available numerical codes, like `CAMB`[3] [165], `CLASS`[4] [166] etc.

In Fig. 5.1, we show the evolution of the metric perturbation ϕ with τ. The respective modes enter the horizon at $\tau_h \equiv 1/k$. Before horizon entry, ϕ remains constant for all modes. The subsequent behaviour depends on k whether it is larger or smaller than $k_{\rm eq}$ ($\simeq 0.011\,\mathrm{Mpc}^{-1}$), the mode which was entering the horizon during matter-radiation equality at $\tau_{\rm eq} \simeq 110\,\mathrm{Mpc}$. For smaller modes ($k > k_{\rm eq}$) which entered the horizon before $\tau_{\rm eq}$, the decay is fast and is followed by oscillations. The fast decay happens because the density perturbations do not grow appreciably during the radiation domination (RD) epoch. The oscillations are induced by the acoustic oscillations in the photon bath which dominates the total energy

3 https://github.com/cmbant/CAMB
4 https://github.com/lesgourg/class_public

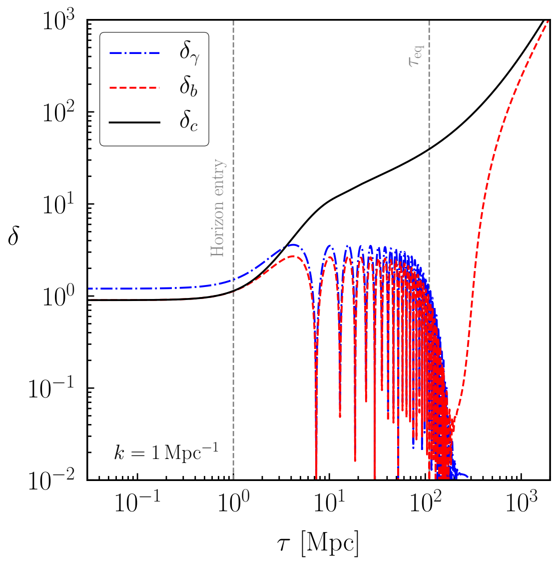

Figure 5.2: Density perturbation evolution for photon (dot-dashed blue), baryon (dashed red), and CDM (solid black) for the mode $k = 1\,\mathrm{Mpc}^{-1}$. The horizon-entry and the matter-radiation equality epochs are marked with dashed gray vertical lines.

density. The larger modes ($k < k_{\rm eq}$) also decrease after horizon-entry but by a smaller amount, and do not experience any oscillation as the Universe has already become matter-dominated. The other metric perturbation ψ differ from ϕ by a small amount due to the anisotropic stress coming from the free streaming neutrinos (see Eq.(5.3)).

All density perturbations remain constant before horizon-entry in the newtonian gauge. This can be seen in Fig. 5.2. The initial values are different for matter and radiation species. During RD, the growth of δ_c is slow logarithmic. When the Universe becomes matter-dominated, the growth is faster as $\delta_c \sim \tau^2$.

As the mode enters the horizon, photon and baryon perturbations start oscillating in unison because of their tight coupling. This is known as the baryon acoustic oscillation (BAO). After recombination when photons start diffusing, the amplitude of the oscillation is damped. Finally, the baryons 'slip' past the photons and begin to fall towards the gravitational potential 'wells' formed by CDM, and δ_b starts following CDM perturbation.

The most useful tool to study the theory of structure formation and test it against the observations is the *two-point function* of the inhomogeneity or the perturbations, called as the *matter power spectrum* $P(k)$. It is defined as

$$\langle \delta(\mathbf{k})\delta(\mathbf{k}')\rangle = (2\pi)^3 P(k)\delta^3(\mathbf{k}-\mathbf{k}')\,, \tag{5.17}$$

where $\delta(\mathbf{k})$ is the total matter density perturbation

$$\delta = \frac{\sum_i \bar{\rho}_i \delta_i}{\sum_i \bar{\rho}_i} \tag{5.18}$$

summed over all matter species (radiation does not cluster), and $\langle \cdots \rangle$ denotes statistical average. The magnitude of $P(k)$ represents the clumpiness of the Universe at the length scale $\sim 1/k$. Large $P(k)$ indicates a lot of collapsed structures at that scale, and small $P(k)$ means less abundance of structure. This $P(k)$ has dimensions of $(\text{Length})^3$. Often a dimensionless form of the power spectrum definition is used,

$$\Delta^2(k) = \frac{k^3 P(k)}{2\pi^2}. \tag{5.19}$$

The power spectrum $P(k)$ has two components – the primordial fluctuations sourced by some mechanism, like inflation, and the evolving perturbations during the history of the Universe. To isolate the evolution part, we define transfer function $T(k)$ as

$$T(k,\tau) = \frac{\delta(k,\tau)}{\Delta_p(k)} \tag{5.20}$$

where $\Delta_p(k)$ is the primordial density fluctuation. In terms of the transfer function, the matter power spectrum is given by

$$P(k) = \frac{2\pi^2 \mathcal{P}_p}{k^3} T(k)^2. \tag{5.21}$$

Here $\mathcal{P}_p(k)$ is the power spectrum of the primordial fluctuations defined as

$$\mathcal{P}_p(k) = A_s \left(\frac{k}{k_0}\right)^{n_s - 1} \tag{5.22}$$

in terms of the amplitude A_s, the scalar index n_s, and the pivot scale k_0.

The matter power spectrum for ΛCDM cosmology is shown in the left panel of Fig. 5.3. The shape of $P(k)$ can be understood by looking at the individual mode evolutions shown in the right panel of Fig. 5.3. The modes $k < k_{\text{eq}}$ enter the horizon after matter-radiation equality and grow as $\sim \tau^2$. However, the smaller k is, the larger τ_h becomes. So the mode has less time to grow until today. Therefore the power should increase with k in the regime $k < k_{\text{eq}}$. This is evident in the figure. Modes which cross the horizon before matter-radiation equality ($k > k_{\text{eq}}$) undergo a period of logarithmic growth during $\tau_h < \tau < \tau_{\text{eq}}$. This is slower than the $\sim \tau^2$ growth during matter domination (MD). As we go to larger k, this period of suppressed growth widens, and as a result the final power today decreases. The modes which enter horizon around the time of matter-radiation equality, i. e., $k \simeq k_{\text{eq}}$, do not experience the log growth period. Hence, the power spectrum has a *turnover* between the increasing behaviour at small k and decreasing behaviour at large k, which is around k_{eq}. In passing we note that, the discussion about structure formation presented here considered only the linear perturbation theory. However, today length scales smaller than $\sim 10\,\text{Mpc}$ have grown nonlinear and one needs to correct for the nonlinearities at those scales before comparing the theoretical prediction with the observed galaxy power spectrum.

Another very useful cosmological observable is the two-point correlation functions of the CMB photon density. Photons, unlike the matter species, do

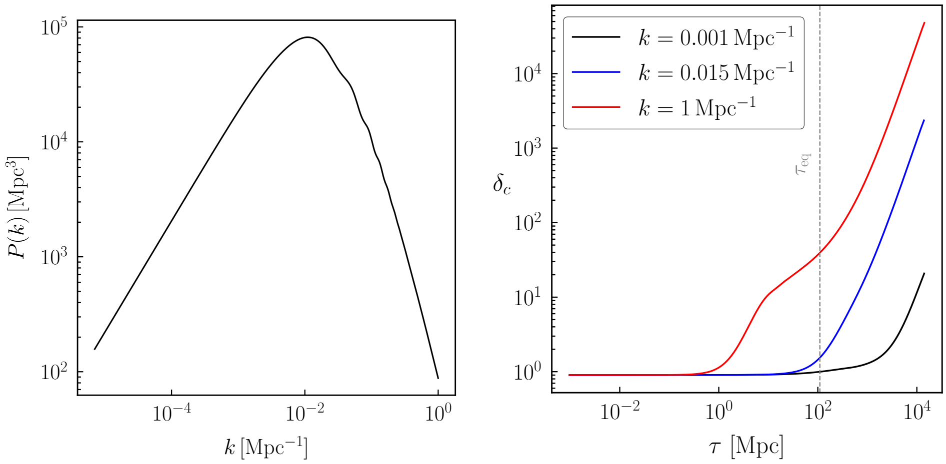

Figure 5.3: The ΛCDM matter power spectrum.

not cluster under gravity. After recombination, when they decoupled from the baryons they continued to free stream until today. As a result, photon perturbations are still small today ($\delta_\gamma \sim 10^{-5}$) and can easily be described by linear physics. The most convenient way study photon inhomogeneities is to look at the anisotropies in the 'sky' of CMB photons. The temperature of the CMB photons is written as

$$T(\hat{n}, \tau_0) = T(\tau_0)\,[1 + \Delta(\hat{n}, \tau_0)] \tag{5.23}$$

where $T(\tau_0) = 2.73$ K is the CMB background temperature today, Δ is a small perturbation. As the density $\bar{\rho}_\gamma \sim T^4$, we note that $\Delta = \delta_\gamma/4$. We expand Δ in terms of the spherical harmonics

$$\Delta(\hat{n}) = \sum_{\ell=1}^{\infty} \sum_{m=-\ell}^{\ell} a_{\ell m} Y_{\ell m}(\hat{n}) \,. \tag{5.24}$$

The anisotropy information of $\Delta(\hat{n})$ is then contained in the expansion coefficients $a_{\ell m}$. Similar to the matter power spectrum, in this case also the angular power spectrum is theoretically defined as the average of the $a_{\ell m}$ coefficients,

$$\langle a_{\ell m} a^*_{\ell' m'} \rangle = C_\ell \delta_{\ell\ell'} \delta_{mm'} \,. \tag{5.25}$$

The statistics of $a_{\ell m}$s were set by the initial fluctuations. If they follow Gaussian statistics with zero mean, then computing C_ℓs contain all the information. Otherwise, higher-point correlation functions would also be needed. From an observed CMB map, the C_ℓs can be computed using the angular two-point correlation function $C(\theta)$ as

$$C(\theta) \equiv \langle \Delta(\hat{n}) \Delta(\hat{n}') \rangle = \frac{1}{4\pi} \sum_{\ell=1}^{\infty} (2\ell + 1) C_\ell P_\ell(\hat{n} \cdot \hat{n}') \tag{5.26}$$

where the unit vectors $\hat{n}$ and $\hat{n}'$ are separated by an angle θ. We show the theoretical CMB angular power spectrum in Fig. 5.4.

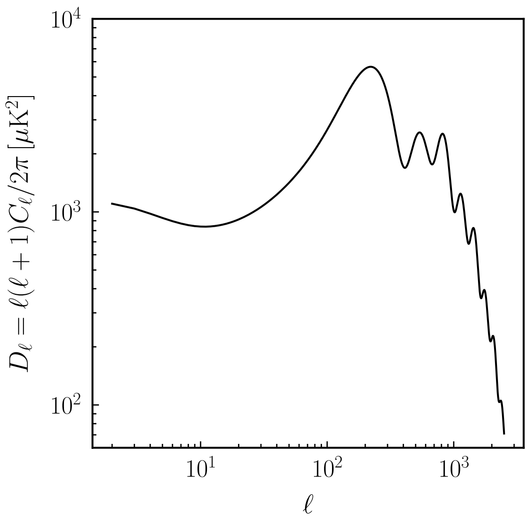

Figure 5.4: CMB anisotropy power spectrum, D_ℓ ($\equiv \ell(\ell+1)C_\ell/2\pi$) as a function of ℓ. Note that the C_ℓ is multiplied by $T^2(\tau_0)$ and, hence is a dimensionful quantity.

5.2 BALLISTIC DARK MATTER

To study the cosmology of late-forming DM, we shall follow an *effective, model-independent* approach. We consider that the dark sector consists of a self-interacting relativistic species at early times which we call as the dark radiation (DR). It transitions to non-interacting nonrelativistic particles, i.e., the dark matter (DM) phase, at a redshift z_* with the corresponding scale factor denoted by a_*. We further assume that the anisotropic stress and all higher order moment perturbations in the Boltzmann hierarchy vanish, i. e., $F_{\ell\geq 2} = 0$, leaving only the density and velocity perturbations. This allows the DR phase to be described by its equation of state. This assumption can be relaxed if we work with the full stress-energy tensor [167]. In the cosmological context, such an evolution can be encoded in a time-varying EoS for the BDM fluid,

$$w_B(z) = \begin{cases} \dfrac{1}{3} & z \gg z_* \quad \text{(before transition)} \\ 0 & z \ll z_* \quad \text{(after transition)}\,. \end{cases} \tag{5.27}$$

The subscript B denotes quantities associated to the BDM fluid.

The exact transition of the EoS between these two limits would depend on the details of the particle physics model of BDM. We expect that the cosmological observables, like the matter power spectrum, would be sensitive to the time or redshift of phase transition and how long the transition period lasts. Based on that, we adopt the following simple model for the EoS,

$$w_B = \frac{1}{6}\left[1 - \tanh\left(\frac{a - a_*}{\Delta}\right)\right] , \tag{5.28}$$

where Δ represents the extent in scale factor over which the transition takes place. We note that as long as $\Delta \ll a_*$ and $a_* \ll 1$, we have $|\Delta/a_*| \approx |\Delta z/z_*|$, where Δz is the redshift-duration of phase transition.

In general, BDM may form only a fraction $f_{\rm BDM}$ of the total dark matter energy density. We parametrize this possibility as define

$$f_{\rm BDM} = \frac{\Omega_{\rm BDM}}{\Omega_{\rm BDM} + \Omega_{\rm CDM}}\,, \tag{5.29}$$

as the present-day ratio of BDM to total dark matter, with the remaining fraction being ordinary CDM-like at all epochs.

The evolution equations for the linear perturbations of the BDM fluid in the conformal Newtonian gauge are given by

$$\dot{\delta_{\rm B}} = -(1+w_{\rm B})(\theta_{\rm B} + 3\dot{\phi}) - 3\frac{\dot{a}}{a}\left(c_s^2 - w_{\rm B}\right)\delta_{\rm B}\,, \tag{5.30}$$

$$\dot{\theta_{\rm B}} = -\frac{\dot{a}}{a}(1-3w_{\rm B})\theta_{\rm B} - \frac{\dot{w}_{\rm B}}{1+w_{\rm B}}\theta_{\rm B} + \frac{c_s^2}{1+w_{\rm B}}k^2\delta_{\rm B} + k^2\psi\,. \tag{5.31}$$

Here c_s is the speed of sound in the BDM fluid during the DR phase. The second term on the RHS of the first equation vanishes because we assume that the EoS does not depend on the energy density, and hence the speed of sound $c_s^2 \equiv \delta P/\delta\rho = w$. We combine Eqs. (5.30) and (5.31) to get a second order equation for $\delta_{\rm B}$.

$$\ddot{\delta_{\rm B}} + \frac{\dot{a}}{a}\left(1-3w_{\rm B}\right)\dot{\delta_{\rm B}} + k^2 w_{\rm B}\delta_{\rm B} = F\,,$$
$$F \equiv -3\frac{\dot{a}}{a}\left(1-3w_{\rm B}\right)\left(1+w_{\rm B}\right)\dot{\phi} - 3\dot{w}_{\rm B}\dot{\phi} - 3\left(1+w_{\rm B}\right)\ddot{\phi} - \left(1+w_{\rm B}\right)k^2\psi\,. \tag{5.32}$$

This is an equation of a damped forced oscillator for $\delta_{\rm B}$, with a forcing term F arising from the metric perturbations sourced by BDM as well as the other components of the Universe. Once the phase transition starts, the equation of state $w_{\rm B} < 1/3$ and the damping term ($\propto \dot{\delta_{\rm B}}$) becomes non-zero, damping the acoustic oscillations until the transition to DM phase is complete and the BDM fluid becomes non-interacting.

We implemented the BDM species, defined by Eqs. (5.28 - 5.31), in the codes `CAMB` [165] and `CLASS` [166]. We added a new species in `CAMB` for BDM. In `CLASS`, we used the `_fld` species as BDM[5]. We computed the transfer functions and the power spectra for this model using both codes and obtained essentially identical results. While using the synchronous gauge, we always keep a trace amount of ordinary CDM component to ensure that the gauge is well-defined. We assumed that the stress-energy tensor components vary continuously across the phase transition to connect the DR phase perturbations with the DM phase perturbations. We also assumed that no additional perturbations are created due to the phase transition itself.

5 The modified CLASS code is available at https://github.com/anirbandas89/BDM_CLASS.

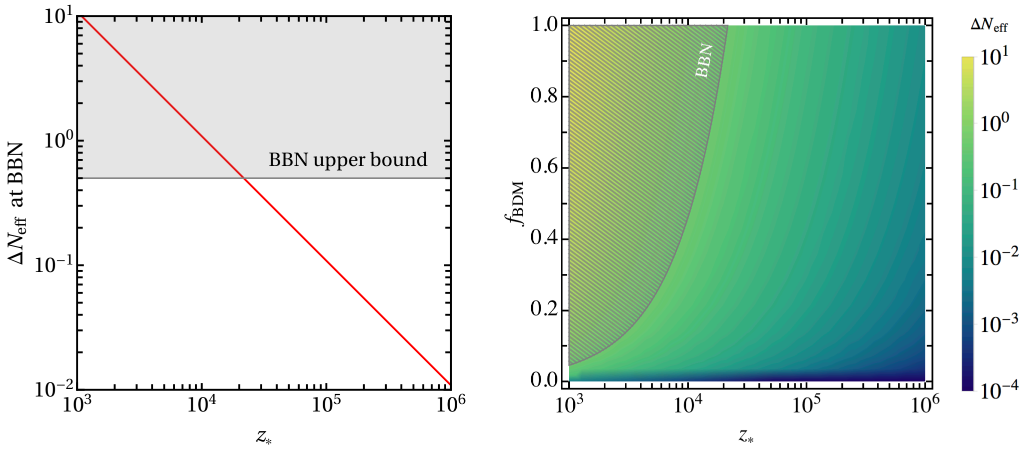

Figure 5.5: (Left) $\Delta N_{\rm eff}$ at BBN for a BDM transition at z_* for $f_{\rm BDM} = 1$. The upper bound is from primordial element abundance measurement that restricts $\Delta N_{\rm eff} < 0.5$ [114, 173]. (Right) The gray-striped region in the $z_* - f_{\rm BDM}$ plane is ruled out by the BBN constraint. Figures taken from Paper III [3].

5.3 COSMOLOGICAL SIGNATURES

5.3.1 *Extra relativistic degrees of freedom*

Before the phase transition, BDM acts like dark radiation and would contribute to the expansion of the Universe in the radiation dominated era modifying the expansion rate of the Universe. This effect is quantified by effective relativistic degrees of freedom $\Delta N_{\rm eff}$ defined in Eq.(2.40) and is repeated here.

$$N_{\rm eff} = \frac{\sum \rho_{\nu_i}}{\rho_\nu^{\rm FD}} + \frac{\rho_{\rm DR}}{\rho_\nu^{\rm FD}} \tag{5.33}$$

$$\equiv N_{\rm eff}^{\rm SM} + \Delta N_{\rm eff}\,. \tag{5.34}$$

Here, $\rho_{\rm DR}$ is the energy density of BDM before phase transition. The theoretical prediction in standard ΛCDM cosmology with only standard model neutrinos contributing to $N_{\rm eff}$ is $N_{\rm eff}^{\rm SM} = 3.046$; the extra 0.046 taking into account the energy gained by neutrinos during the electron-positron annihilation [168–172]. We have defined $\Delta N_{\rm eff}$ as the contribution by new physics.

The quantity $\Delta N_{\rm eff}$ is constrained by both CMB and big bang nucleosynthesis (BBN) observation data. The CMB experiments, such as Planck, WMAP etc. are sensitive to the amount of radiation density present during recombination at $z \sim 1100$. The DR in our BDM model never thermalized with the visible sector. Also the time of phase transition must be much earlier than the recombination era and the era of matter-radiation equality to satisfy the current cosmological constraints on the dark matter power spectrum. Therefore, the CMB anisotropy constraints on $N_{\rm eff}$ do not apply to our model because by the time of recombination BDM has the same background evolution as the CDM. Here we are implicitly assuming that

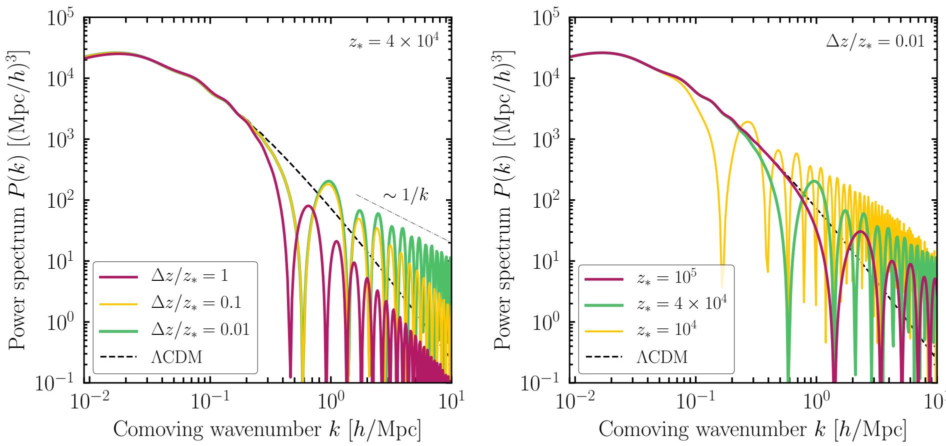

Figure 5.6: (Left) The matter power spectrum in a ΛBDM cosmology with phase transition at $z_* = 4 \times 10^4$, but with different transition widths $\Delta z/z_* = 1$ (purple), 0.1 (yellow), and 0.01 (green). (Right) The same matter power spectrum with different phase transition redshifts $z_* = 10^5$ (purple), 4×10^4 (green), and 10^4 (yellow), but now for a fixed width $\Delta z/z_* = 0.01$. For comparison, the ΛCDM power spectrum is shown as a dashed black curve in both panels. Note the enhancement of power at the acoustic peaks at small scales relative to the ΛCDM case. Figures taken from Paper III [3].

all of the energy density in the BDM converts to dark matter. If this is not the case, and some energy remains as radiation, the constraint from CMB may also be important. However, if the phase transition happens after the BBN then DR in BDM model will certainly contribute to the $N_{\rm eff}$ at the time of BBN and can be constrained from the measurement of the primordial helium and deuterium abundance [114, 173]. The strongest BBN constraints at present are given by $N_{\rm eff} = 3.28 \pm 0.28$ [114] or $\Delta N_{\rm eff} \lesssim 0.5$.

In the left panel of Fig. 5.5, we show the change in $\Delta N_{\rm eff}$ at the time of BBN as a function of z_*. For $f_{\rm BDM} = 1$, one finds $z_* \gtrsim 2 \times 10^4$. Note the $\simeq 1/z_*$ scaling of the limit. This was expected because the energy density due to BDM is fixed by requiring that it reproduce the present-day dark matter energy density. The excess radiation in the BBN epoch thus simply scales with the relative factor $(1 + z_{\rm BBN})/(1 + z_*)$. In the right panel of Fig. 5.5, the variation of $\Delta N_{\rm eff}$ in the plane of $z_* - f_{\rm BDM}$ is shown. The BBN constraint rules out the gray-striped region.

5.4 MATTER POWER SPECTRUM

The main signature of BDM is through its impact on the matter density perturbations. Unlike in ΛCDM cosmology, here the BDM can support 'sound' waves until the phase transition occurs at z_*, leading to acoustic oscillations for k modes inside the horizon at z_*. We will also see that the nature of these acoustic oscillations in BDM is somewhat different from the acoustic damping seen in models where CDM is allowed to interact with a radiation like species.

In Fig. 5.6, we show the dark matter power spectrum $P(k)$ in a ΛBDM cosmology for different values of the additional parameters of the theory, namely, the width of the phase transition $\Delta z/z_*$ and transition epoch z_*. In the left panel, the green, yellow and purple curves represent the matter power spectra for transition widths $\Delta z/z_* = 0.01,\ 0.1$, and 1, respectively. An important observation here is the relative suppression of the spectrum for slower phase transitions. This feature can be attributed to the second term ($\propto \dot{\delta}_{\rm B}$) on the LHS of Eq.(5.32). This term acts as a *friction* term in the oscillator equation and damps the fluctuations during the span of the phase transition. The effect of the phase transition epochs, $z_* = 10^4,\ 4\times 10^4$, and 10^5, on the matter power spectrum is shown in the right panel of Fig. 5.6. The value of z_* decides the scale or wavenumber k_* that was entering the horizon at the time of phase transition. All modes with $k < k_*$ entered the horizon after z_*, and are unaffected leaving the power spectrum is indistinguishable from the ΛCDM case. The modes with $k > k_*$ entered the horizon before the phase transition and experienced acoustic oscillations leading to the new features in the power spectrum. Of course, as one would expect, if the phase transition occurs at very early times the scale of acoustic oscillations moves to larger k, converging to the ΛCDM model in the limit $z_* \to \infty$.

5.4.1 *Analytical understanding of the acoustic peaks*

To understand the effect of the phase transition on the evolution of the perturbations in a simple way, we first assume an instantaneous transition at conformal time τ_*, corresponding to the redshift z_*. Also, in this section, we shall assume $z_* > z_{eq}$, i.e., the phase transition happens inside the radiation-dominated era. With this instantaneous phase transition approximation, the evolution equation for $\delta_{\rm B}$, Eq. (5.32), in each phase can be written as:

$$\ddot{\delta}_{\rm B} + \frac{k^2}{3}\delta_{\rm B} = -4\ddot{\phi} - \frac{4}{3}k^2\psi\,, \quad \text{DR phase}\,, \tag{5.35}$$

$$\ddot{\delta}_{\rm B} + \frac{\dot{a}}{a}\dot{\delta}_{\rm B} = -3\ddot{\phi} - 3\frac{\dot{a}}{a}\dot{\phi} - k^2\psi\,, \quad \text{DM phase}\,. \tag{5.36}$$

In this section, we shall be interested only in those modes which entered the horizon much before τ_*. We know that the metric perturbations decay to zero after a mode k enters the horizon during the radiation-domination era. Therefore, if we ignore the potential-dependent source terms on the RHS of Eqs. (5.35) and (5.36), the BDM perturbation equation Eq. (5.35) has an oscillatory solution

$$\delta_{\rm B}(x < x_*) = A\cos x\,, \tag{5.37}$$

where we have defined the dimensionless quantity $x \equiv k\tau/\sqrt{3}$ for convenience. We kept only the cosine solution, as required by the adiabatic initial conditions at $\tau = 0$. This solution represents perturbation modes with acoustic oscillations of frequency $k/\sqrt{3}$. After the phase transition the

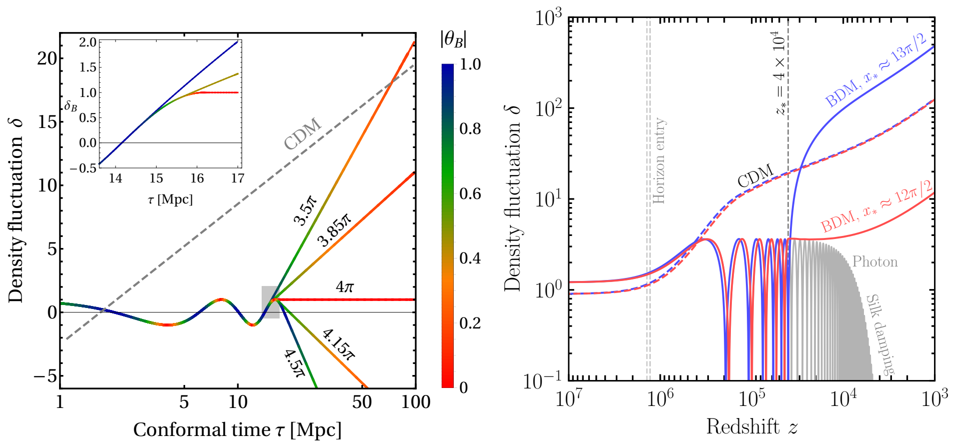

Figure 5.7: (Left) Analytical solution of the BDM linear perturbation equations for the mode $k = 2h/\mathrm{Mpc}$. Five curves are shown with different τ_*s corresponding to $x_* = 3.5\pi$, 3.85π, 4π, 4.15π and 4.5π, respectively. The colour of the curves represent the absolute value of the velocity perturbation $|\theta_\mathrm{B}|$. A zoomed-in version of the gray region is shown in the inset. The dashed, gray line shows the evolution of the same mode in CDM perturbation. (Right) Numerical solution for evolution of two modes of BDM perturbation δ_B corresponding to a maximum ($x_* \approx 13\pi/2$) and a minimum ($x_* \approx 12\pi/2$) in the matter power spectrum. Corresponding CDM mode evolutions in ΛCDM cosmology are also shown as dashed curves. The other parameter values are $z_* = 4 \times 10^4$, $\Delta z/z_* = 10^{-2}$ and $f_\mathrm{BDM} = 1$. Figures taken from Paper III [3].

evolution of BDM is described by Eq. (5.36), yielding logarithmic growth during radiation domination,

$$\delta_\mathrm{B}(x > x_*) = B \ln x + C\,. \tag{5.38}$$

To fix the constants of integration, B and C, we should know the T^{00} and T^{0i} components of the BDM stress-energy tensor at the end of the phase transition or at the beginning of the DM phase. Because we are trying to study the cosmology in a model-independent way, we consider the simplest possible choice, i.e., both these components of $T^{\mu\nu}$ are continuous during the phase transition. This assumption yields

$$\begin{aligned} (\delta_\mathrm{B})_\mathrm{DR} &= (\delta_\mathrm{B})_\mathrm{DM}\,, \\ (\dot{\delta_\mathrm{B}})_\mathrm{DR} &= (\dot{\delta_\mathrm{B}})_\mathrm{DM} - \dot{\phi}\,. \end{aligned} \tag{5.39}$$

Since the potential ϕ decays after the mode enters the horizon, we finally have continuous δ_B and $\dot{\delta_\mathrm{B}}$ across the phase transition happening $x = x_*$. Their values at x_* act as the initial conditions for the perturbations in the ensuing DM phase. Therefore, the solutions of Eq.(5.37) and (5.38) need to be matched at $x = x_*$ by equating δ_B and $\dot{\delta_\mathrm{B}}$. The final DM phase solution is then given by

$$\delta_\mathrm{B}(x > x_*) = A \cos x_* - A x_* \sin x_* \ln\left(\frac{x}{x_*}\right)\,. \tag{5.40}$$

The constant A is set by the initial conditions or initial curvature perturbation. Although the evolution is always logarithmic during radiation dominated era, depending on the value of $x_* = k\tau_*/\sqrt{3}$, two extreme cases are possible in the DM phase:

$$\delta_B(x) = (-1)^n A\,, \qquad \text{if } x_* = n\pi\,, \tag{5.41}$$

$$\delta_B(x) = (-1)^{n+1} A x_* \ln\left(\frac{x}{x_*}\right)\,, \qquad \text{if } x_* = \left(n + \frac{1}{2}\right)\pi\,. \tag{5.42}$$

Here n is any integer. For the modes with k such that $x_* = n\pi$, the density fluctuation does not grow at all after the phase transition. Eventually these modes at even multiples of $\pi/2$ (or zeros of the sine) at the phase transition will carry less power and correspond to the minima in the power spectrum. On the contrary, if $x_* = (n + 1/2)\pi$, these modes at odd multiples of $\pi/2$ at the phase transition (extrema of the sine function) will have logarithmic growth with maximum slope. This large initial slope or prefactor is responsible for fast initial growth which may, for sharp phase transitions, overtake the ΛCDM perturbation giving acoustic peaks that overshoot the ΛCDM power for the same k modes.

Physically these two families of solutions are caused by the different *velocities* of the perturbation at τ_*. The modes which were crossing zero and had maximum velocity at x_*, i.e., $|\dot{\delta}_B(x_*)| = A$, will continue moving *ballistically* with the same bulk velocity in the collisionless DM phase, until the initial velocity is redshifted away. This inherited extra *bulk velocity kick* w.r.t what we expect from just gravitational infall in standard CDM, results in a faster logarithmic growth for these modes compared to all other modes. On the other hand, the modes having maximum displacement and zero velocity at x_*, i.e., $|\dot{\delta}_B(x_*)| = 0$, will not grow initially because the prefactor of the logarithmic term in Eq. (5.40) vanishes. All other modes which do not belong to these two extreme cases also have logarithmic growth but with relatively smaller slope. After $\tau = \tau_{eq}$ in the matter-dominated era, all modes grow as $\delta_B \sim a \sim \tau^2$. These different types of mode evolution will reflect themselves in the shape of the matter power spectrum. In particular it is the peculiar or bulk velocities of acoustic oscillations, and hence the sine mode, which get imprinted in the matter power spectrum, similar to the phase shift experienced by the baryon acoustic oscillations w.r.t. to the acoustic oscillations imprinted in the CMB [174, 175].

In the left panel of Fig. 5.7, we show the evolution of δ_B as a function of τ for the mode $k = 2h/\text{Mpc}$ for five different values of τ_*. This is simply the analytical solution shown in Eq. (5.40). The color-coding represents the absolute value of $\dot{\delta}_B$, hence the absolute value of θ_B. The transition epochs are chosen such that $x_* = 3.5\pi,\ 3.85\pi,\ 4\pi,\ 4.15\pi$ and 4.5π, respectively. Until the phase transition the evolution is identical, but depending on x_* the curves emanate from the phase transition point with different colours (i.e., velocities) which can be seen in the zoomed-in version of the gray region in the inset. As was argued in Eq.(5.42), the cases $x_* = 3.5\pi$ and 4.5π correspond to the extrema of the sine function (or the peculiar velocities at the phase transition) which show fast growth of the perturbations, resulting in excess power at the acoustic peaks seen in Fig. 5.6. The case with $x_* = 4\pi$ is the zero of the sine function and has zero velocity but maximum density perturbation at $\tau = \tau_*$ and remains frozen at this value, lagging behind all other modes at late times. They correspond to the dips in the oscillatory part of the power spectrum. Other cases of $x_* = 3.85\pi$ and 4.15π have intermediate velocities at τ_*. Note how all peculiar velocities redshift as $\sim 1/a$ after the phase transition. Eventually, of course, the peculiar velocities sourced by gravitational potentials will take over.

In the right panel of Fig. 5.7, we see that the numerical results show the same behavior as above. The two modes, $k = 4.305h/\mathrm{Mpc}$ and $4.661h/\mathrm{Mpc}$, roughly correspond to $x_* \simeq 12\pi/2$ and $13\pi/2$, respectively, for a phase transition at $z_* = 4 \times 10^4$. These modes lead to a dip and a peak, respectively, in the matter power spectrum. The perturbations remain constant at their initial values until the time of their respective horizon entry which happens when $k\tau \simeq 1$. Afterwards they start oscillating with a frequency $k/\sqrt{3}$. They continue to oscillate until τ_*, thereafter they start growing as $\sim \ln \tau$ during the radiation-domination era and as $\sim \tau^2$ in the matter-domination era. The same modes for δ_c in a ΛCDM cosmology are also shown in the dashed curves. As discussed in the preceding paragraph, the modes starting with extra *bulk velocity kicks* from the pre-phase transition oscillations overshoot the ΛCDM value and eventually acquire more power. They give rise to the peaks in Fig. 5.6. Whereas those perturbations which were at their maximum values at the time of phase transition (hence, zero velocity) grow at a much slower rate and lead to the dips in Fig. 5.6. Indeed the mode labeled by $x_* \approx 13\pi/2$ (solid blue, peak of the sine function), grows faster and goes above the ΛCDM curve (dashed blue, zero of the sine function), while the mode labeled by $x_* \approx 12\pi/2$ (red curve) remains below it. This gives rise to the oscillatory feature in the matter power spectrum in Fig. 5.6, with the upper envelop of the oscillations going above the ΛCDM expectation.

From Eq.(5.42), we note that the absolute value of maximum perturbation is proportional to the wavenumber k. Hence the transfer function $T(k)_{\mathrm{max}} \sim k$. As a result, we expect the envelop of the peaks of the $P(k)$ to scale as $\sim 1/k$,

$$P(k)_{\mathrm{max}} \equiv \frac{2\pi^2 \mathcal{P}_p}{k^3} T(k)^2_{\mathrm{max}} \sim 1/k\,, \tag{5.43}$$

where $\mathcal{P}_p$ is the primordial scalar power spectrum defined as

$$\mathcal{P}_p = A_s \left(\frac{k}{k_0}\right)^{n_s - 1}, \tag{5.44}$$

in terms of the amplitude A_s, the scalar index $n_s = 0.96$, and the pivot scale k_0 [176]. The $1/k$ upper envelop of $P(k)$ predicted by Eq.(5.43) is evident in Fig. 5.6 for the case of fast transition, $\Delta z/z_* = 0.01$, as shown by the dashed gray line.

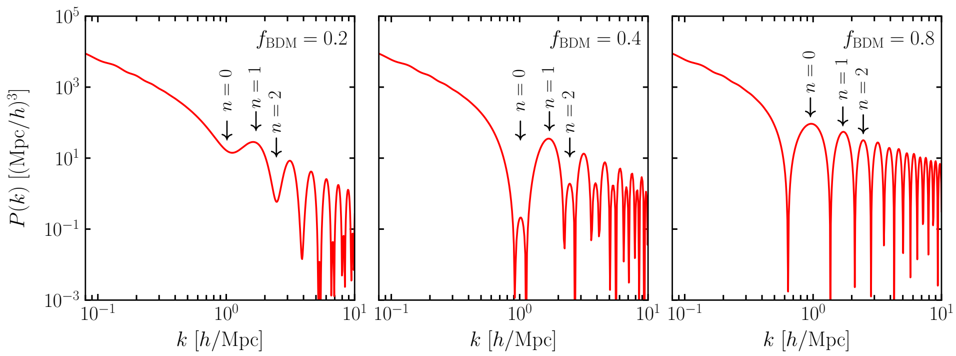

Figure 5.8: The matter power spectra for three different BDM fractions $f_{\mathrm{BDM}} = 0.2,\ 0.4$ and 0.8. The first three 'peaks' numbered by $n = 0, 1, 2$ (see Eq. (5.42) for details) are marked with black arrows. Figures taken from Paper III [3].

5.4.2 *Odd-even peak asymmetry*

An interesting asymmetry in the heights of the power spectrum peaks becomes apparent if the fraction of BDM is neither 0 nor 1. Three representative cases are shown in Fig. 5.8 with $f_{\mathrm{BDM}} = 0.2,\ 0.4$ and 0.8, respectively. We have numbered the peaks according of value of n in Eq. (5.42) with the first peak given by $n = 0$ corresponding to first zero crossing of cosine (density) or first extrema of sine (peculiar velocity). First, we concentrate on the $f_{\mathrm{BDM}} = 0.4$ case and observe that the heights of the odd-numbered peaks are greater than the even-numbered ones. To understand the reason behind this asymmetry, we plot in the left panel of Fig. 5.9 the individual BDM and CDM transfer functions T_{B} (dashed orange) and T_{C} (dashed light blue), along with the total dark matter transfer function $T_{\mathrm{DM}}(k)$ (solid black), which is defined as

$$T_{\mathrm{DM}}(k) = f_{\mathrm{BDM}} T_{\mathrm{B}}(k) + (1 - f_{\mathrm{BDM}}) T_{\mathrm{C}}(k)\,, \tag{5.45}$$

at a redshift $z = 3000$. Oscillations with amplitude growing with k are present in the BDM transfer function, $T_{\mathrm{B}}(k)$, as expected. However, we now see that such oscillations, albeit with smaller amplitude, are also imprinted in the CDM transfer function T_{C}. This is the result of the CDM responding to the gravity of BDM or the gravitational potential ϕ which has contribution from T_{B}. Further, we observe the relative sign between the two transfer functions. At the positions of the peaks of T_{B}, the two transfer functions have the same sign and reinforce each other resulting in a larger magnitude of T_{DM}. On the other hand, at the troughs of T_{B} they have opposite signs and can partially cancel each other. These shallower troughs of the T_{B}, that are below zero, appear as smaller peaks in the matter power spectrum. This leads to the asymmetry between the consecutive maxima in the matter power spectrum in Fig. 5.8. Physically, the initial velocities of BDM at the phase transition for k modes corresponding to even values of n were such that the (BDM) matter flowed from out of the initial overdensities, which were the same for CDM and BDM according to

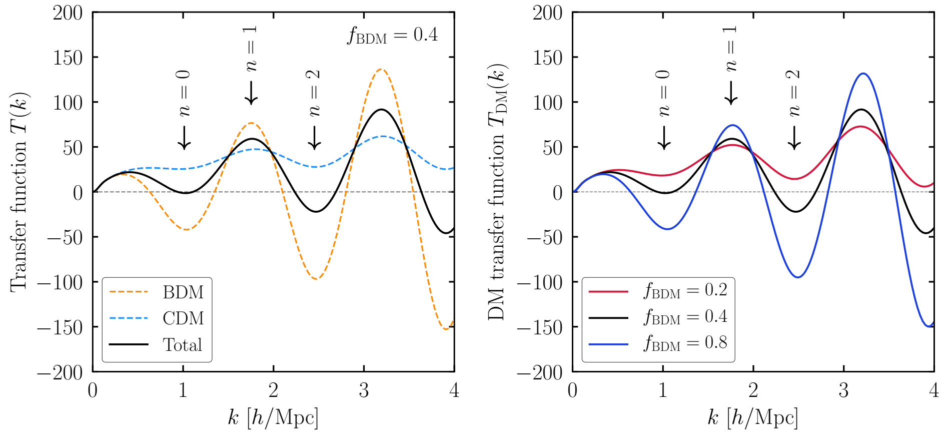

Figure 5.9: (Left) Individual transfer functions of BDM $T_B(k)$ (dashed orange), CDM $T_C(k)$ (dashed light blue), and the total dark matter transfer function $T_{DM} = f_{BDM}T_B + (1 - f_{BDM})T_C$ (solid black) at redshift $z = 3000$ for $f_{BDM} = 0.4$. (Right) Comparison between dark matter transfer functions $T_{DM}(k)$ computed for three different fractions of BDM, viz., $f_{BDM} = 0.2$ (red), 0.4 (blue), and 0.8 (green). Other phase transition parameters are $z_* = 4 \times 10^4$, $\Delta z/z_* = 10^{-2}$. Figures taken from Paper III [3].

the adiabatic initial conditions, and flowed into the initial underdensities and thus reducing the amplitude of perturbations for those modes. For the modes corresponding to odd values of n, the BDM matter flowed into the CDM overdensities and out of the CDM underdensities, increasing the density contrast.

Both components of the dark matter are needed in sizeable amount for the odd-even acoustic peak asymmetry to be prominent. This is evident from the $f_{BDM} = 0.2$ and 0.8 plots in Fig. 5.8 and the right panel of Fig. 5.9. For $f_{BDM} = 0.2$, the BDM has a sub-dominant contribution to the total power spectrum and the out of phase extrema of BDM (even-n) only result in giving minima in the total power spectrum. Thus only the odd-n modes result in acoustic peaks in the total matter power spectrum. As we increase f_{BDM}, the minima in the total transfer function become deeper and deeper and at some point cross zero (see Fig. 5.9, right panel). Once the total transfer function has a zero crossing, the zero-crossings become the deep minima in the matter power spectrum and the minima of the transfer function appear as additional peaks, doubling the number of acoustic peaks in the total power spectrum.

The asymmetry, i.e., the relative heights of the consecutive maxima in the power spectrum is fixed once the initial peculiar velocities have redshifted away. Subsequently, the BDM and CDM can be treated as a single collisionless cold fluid, with a modified power spectrum which grows linearly with redshift identically to the CDM fluid in the standard ΛCDM cosmology. In particular, subsequent linear growth does not change the shape of the power spectrum and the asymmetry and acoustic features persist until today in linear theory.

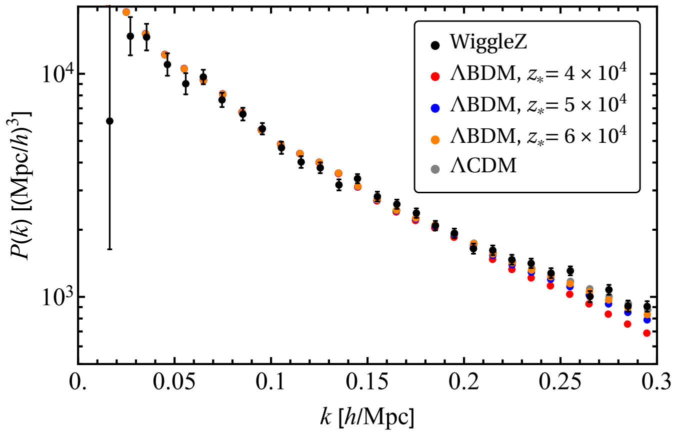

Figure 5.10: Comparison between the observed matter power spectrum by WiggleZ [6] and the theoretical power spectra for different transition redshifts, $z_* = 4 \times 10^4,\ 5 \times 10^4,\ 6 \times 10^4$. Figures taken from Paper III [3].

5.5 QUALITATIVE CONSTRAINTS FROM THE MATTER AND CMB POWER SPECTRUM

As we have already discussed, the effective relativistic degrees of freedom during BBN already gives interesting constraints on the redshift of phase transition. A more stringent lower bound on z_* is given by the measurement of the dark matter power spectrum. From Fig. 5.6 we see that even a value $z_* = 10^4$ predicts a sharp drop in power at $k = 0.1h/\mathrm{Mpc}$ near the second BAO peak. These scales are well measured at many redshifts by the current galaxy surveys like SDSS [177] and WiggleZ [6] and therefore $z_* = 10^4$ is clearly ruled out by the current matter power spectrum measurements. We show the WiggleZ data from the redshift range $0.5 < z < 0.7$ and theoretical ΛBDM power spectrum using the flat ΛCDMbest-fit model parameters in the Table VII of Ref. [6] in Fig. 5.10 for different z_*. We have used the same binning as the WiggleZ data for the theoretical power spectrum and convolved it with the WiggleZ window function. As we can see, even when restricting to approximately linear modes, $k < 0.3h/\mathrm{Mpc}$, we can already rule out z_* smaller than $\sim 5 \times 10^4$ by eye. We remind that this is a crude estimate, and to be more accurate one needs to do a more detailed study with degeneracies with other ΛCDMparameters, such as n_s, taken into account.

We will also expect modifications to the CMB anisotropy power spectrum at small angular scales as it is sensitive to the total dark matter power spectrum at the time of recombination. In a flat Universe, the mode k_* corresponds to an approximate angular scale of $\ell_* \simeq k_*\tau_0$ where $\tau_0 = 1.4 \times 10^4$ Mpc is the conformal time today. Therefore the observability of this effect in the CMB angular power spectrum would depend on the value of k_*. The smallest scale probed by the current Planck experiment corresponds to $\ell_{\max} = 2500$ implying a value of $k_* \simeq 0.2h/\mathrm{Mpc}$, therefore a sensitivity to $z_* \lesssim 6 \times 10^4$. The typical changes expected in the CMB

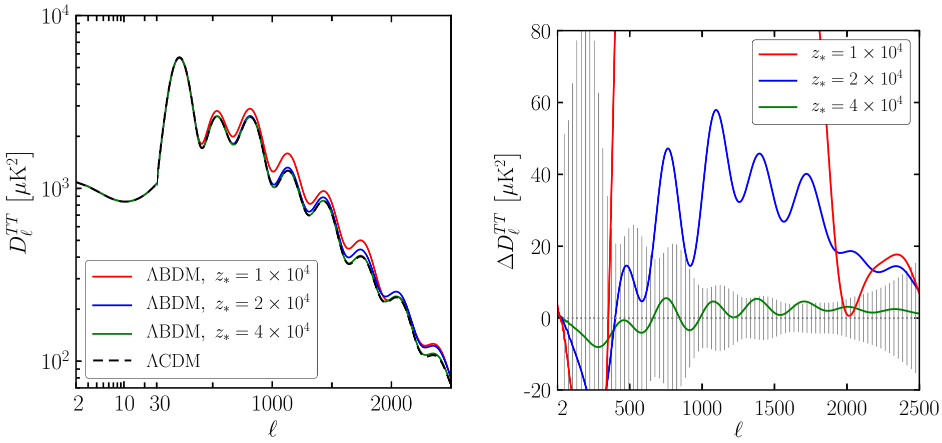

Figure 5.11: (Left) Effects in the CMB TT power spectrum is shown for $z_* = 10^4$ (red), 2×10^4 (blue), and 4×10^4 (green) with $\Delta z/z_* = 0.01$ and $f_{\rm BDM} = 1$. (Right) The difference between ΛBDM and ΛCDM powers $\Delta D_\ell^{TT} \equiv (D_\ell^{TT})_{\Lambda\rm BDM} - (D_\ell^{TT})_{\Lambda\rm CDM}$. We compare this ΔD_ℓ^{TT} with the Planck high-ℓ ($47 \leq \ell \leq 2499$) binned data, and conclude that the Planck data puts a rough lower limit on the transition redshift $z_* \gtrsim 4 \times 10^4$. Figures taken from Paper III [3].

TT angular power spectrum are shown in the left panel of Fig. 5.11 for $z_* = 10^4$ (red), 2×10^4 (blue) and 4×10^4 (green). We use the best-fit values of ΛCDM parameters from the Planck experiment [176]. In the right panel of Fig. 5.11, we plot the difference between ΛBDM and ΛCDM powers $\Delta D_\ell^{TT} \equiv (D_\ell^{TT})_{\Lambda\rm BDM} - (D_\ell^{TT})_{\Lambda\rm CDM}$ together with the Planck high-ℓ ($47 \leq \ell \leq 2499$) binned data error bars. We conclude that values of transition redshift $z_* \lesssim 4 \times 10^4$ are not consistent with the CMB data. The next-generation CMB observation experiments promise to probe even smaller angular scales and correspondingly smaller k values [178].

The matter power spectrum and the CMB power spectrum at present would give comparable constraints on the BDM parameters ($z_*, \Delta z/z_*, f_{\rm BDM}$) with the constraints from the matter power spectrum expected to be stronger. We leave a more detailed Markov Chain Monte Carlo study of the ΛBDM parameters using current CMB temperature and polarization data and matter power spectrum for a future publication.

5.6 SUMMARY & CONCLUSIONS

We studied the cosmological consequences of a class of dark matter models defined by two main properties:

1. The time when the dark matter becomes nonrelativistic coincides with it also becoming collisionless and the dark fluid is strongly interacting before this phase transition.

2. This phase transition happens much later than the decoupling of dark matter from the visible sector and in particular happens after BBN and before recombination.

Before the transition to non-relativistic collisionless dark matter, the radiation-like particles were tightly coupled together and constituted a perfect fluid. The pressure in the fluid supports acoustic oscillations and stalls the growth of density perturbations during the period between a mode's horizon entry at τ_h and the phase transition at τ_*. The consequence of the above two features is that the non-relativistic phase of the dark matter starts with a non-zero peculiar velocities which are a sinusoidally oscillating function of the mode k, and which are out of phase by $\pi/2$ w.r.t. the density fluctuations, inherited from the previous tightly coupled relativistic phase. The initial evolution in the collisionless phase is ballistic until the initial acoustic peculiar velocities have been redshifted away. Afterwards the perturbations grow in a similar fashion as in the ΛCDM cosmology. The initial evolution after the phase transition of a mode is therefore driven almost entirely by the peculiar velocities at the phase transition. The modes which had the maximum velocity at τ_* grow fastest, and the modes for which the density perturbation was at the maximum amplitude and hence had zero velocity have the slowest initial growth. The acoustic oscillations before the phase transition are thus imprinted on the dark matter power spectrum. For fast phase transitions, the acoustic peaks in the matter power spectrum, driven by high initial peculiar velocities, can exceed the ΛCDM power. The excess growth of power relative to the ΛCDM case can be suppressed if the phase transition happens rather slowly. A gradual variation of the EoS of the dark sector fluid leads to damping of perturbations.

If BDM does not dominate the matter energy density in the Universe then an asymmetry arises in the peak heights of the matter power spectrum. This happens because the transfer functions of CDM and BDM can be in-phase or out-of-phase at the extrema of the BDM transfer function. The minima and maxima of the BDM transfer function have opposite signs and would give rise to similar amplitude acoustic peaks if BDM formed all of dark matter. The CDM transfer function on the other hand does not change sign as a function of k. Therefore successive extrema of the BDM would have alternatively the same and the opposite sign to that of CDM and the two can add constructively or destructively. The acoustic peaks in the total matter power spectrum would be therefore alternate between enhancement and suppression giving rise to an odd-even peak asymmetry.

By varying the three parameters of our BDM model, the redshift of phase transition, z_*, the duration of phase transition, $\Delta z/z_*$, and the fraction of dark matter formed by BDM, $f_{\rm BDM}$, we can get a rich variety of features and, in particular, tune the matter power spectrum to be enhanced or suppressed at particular wavenumbers k. We have shown, by comparison with existing data, that for fast transitions and all of DM formed by BDM, the phase transitions must happen at $z_* > 5 \times 10^4$. Our results indicate that Ballistic Dark Matter has rich cosmological phenomenology and motivate a more detailed study of the consequences of such a dark matter model on the large scale structure, in particular in the non-linear regime, in the future.

6 CONCLUSIONS & OUTLOOK

Dark matter forms a large part of today's Universe, accounting for at least $\sim 25\%$ of the Universe, yet we do not know about its origin or its microscopic nature. Theories of particle dark matter have been most persuasive. It is thought that the dark matter particles are nonrelativistic and mostly collisionless today. Observational data, both astrophysical and cosmological, straddling over several orders of magnitude of length scale can be successfully explained within the paradigm of cold collisionless dark matter. As a result, this theory has been standardized and forms an essential part of the standard model of modern cosmology, namely the ΛCDM cosmology.

However, a few unresolved issues still remain which demand for a better understanding of the baryonic astrophysics or of the dark sector, or both. For example, collisionless cold dark matter fails to explain the diversity in the observed galaxy density profiles. Even though, this apparent diversity could be a result of complicated astrophysical phenomena, like supernova explosion, mass accretion, tidal interaction between dark matter halos etc., there have been tantalizing evidences that collisional dark matter particle can also be an answer to this puzzle. Another question that we do not know the answer of is when the dark matter became cold and collisionless during the course of the history of the Universe. We tried to investigate these questions in this thesis, and find novel effects due to *beyond standard model* dark sector physics that would be observable in various experiments and observations.

In Ch. 3, we studied the phenomenology of a two-level dark matter model to illustrate a new angular momentum and spin-dependent selection mechanism in the Sommerfeld effect. The particle exchange symmetry picks out certain partial wave channels that are enhanced by the Sommerfeld effect, suppressing the other channels at the same time. Multilevel dark matter models where dark matter annihilation is otherwise p-wave suppressed can exhibit large annihilation rate because of this effect. This yields a signature behavior of the annihilation rate with the dark matter velocity, e.g., dark matter particles annihilate faster in MW-like galaxies than in dwarf galaxies or galaxy clusters. This could also potentially help us explain the positron excess seen in several experiments. Future cosmic ray experiments will decide if the excess is due to enhanced dark matter annihilation or other astrophysical sources in the MW.

In Ch. 4, we discussed the scattering phenomenology of a two-level dark matter system. The presence of multiple states bears the possibility of inelastic scattering, and thereby an energy dissipation mechanism with possible implications for the dark matter halo morphology and dynamics. When two dark matter particles upscatter from the ground state to the excited state and decay back to the ground state, two light mediator particles are emitted carrying away a certain amount of energy. A dark matter halo could lose energy through this process. The same process also leads to a drag force in addition to the usual elastic scattering induced drag between two colliding halos. Simple numerical estimates of these processes were given. Computer simulations with dissipation mechanism implemented in the dark sector will test such multilevel dark matter theories.

In Ch. 5, we considered the effects of a late dark sector 'phase transition', when a collisional relativistic fluid converts into the cold collisionless dark matter, on the cosmological observables. In the radiation phase, the fluid experiences acoustic oscillations followed by logarithmic growth of the density perturbations owing to the *bulk velocity* of the fluid during the matter phase. The acoustic oscillations leave imprint on the matter power spectrum at scales that entered the horizon before the transition. The ballistic motion of the dark matter fluid following the transition enhances the power of the maxima modes compared to the ΛCDM. As a result, the overall envelope of the oscillations in the power spectrum goes above the ΛCDM. An odd-even peak height asymmetry arises if the ballistic dark matter forms only a fraction of the dark matter population which was explained by an alternate cancellation/enhancement between the ballistic and ordinary cold dark matter transfer functions. The temperature and polarization anisotropy power spectra of the CMB radiation are also modified. This model could be tested by comparing the matter and CMB power spectrum with the observed ones. Especially, this theory predicts drastic modification in the matter power spectrum at small scales. This would have implications for the dark matter halo abundance in today's Universe.

[1] Anirban Das and Basudeb Dasgupta. "A Selection Rule for Enhanced Dark Matter Annihilation." In: *Phys. Rev. Lett.* 118.25 (2017), p. 251101. DOI: 10.1103/PhysRevLett.118.251101. arXiv: 1611.04606 [hep-ph] (cit. on pp. ix, 27, 37, 47, 49).

[2] Anirban Das and Basudeb Dasgupta. "New dissipation mechanisms from multilevel dark matter scattering." In: *Phys. Rev.* D97.2 (2018), p. 023002. DOI: 10.1103/PhysRevD.97.023002. arXiv: 1709.06577 [hep-ph] (cit. on pp. ix, 43, 45, 47, 50, 53).

[3] Anirban Das, Basudeb Dasgupta, and Rishi Khatri. "Ballistic Dark Matter oscillates above ΛCDM." In: *JCAP* 1904.04 (2019), p. 018. DOI: 10.1088/1475-7516/2019/04/018. arXiv: 1811.00028 [astro-ph.CO] (cit. on pp. ix, 59, 69, 70, 72, 75–78).

[4] N. Aghanim et al. "Planck 2018 results. VI. Cosmological parameters." In: (2018). arXiv: 1807.06209 [astro-ph.CO] (cit. on pp. 1–3, 6, 24).

[5] Max Tegmark et al. "Cosmological parameters from SDSS and WMAP." In: *Phys. Rev.* D69 (2004), p. 103501. DOI: 10.1103/PhysRevD.69.103501. arXiv: astro-ph/0310723 [astro-ph] (cit. on p. 1).

[6] D. Parkinson et al. "The WiggleZ Dark Energy Survey: Final data release and cosmological results." In: *Phys. Rev. D* 86.10, 103518 (Nov. 2012), p. 103518. DOI: 10.1103/PhysRevD.86.103518. arXiv: 1210.2130 (cit. on pp. 1, 77).

[7] M. Costanzi et al. "Dark Energy Survey Year 1 Results: Methods for Cluster Cosmology and Application to the SDSS." In: (2018). arXiv: 1810.09456 [astro-ph.CO] (cit. on p. 1).

[8] T. M. C. Abbott et al. "Dark Energy Survey Year 1 Results: Constraints on Extended Cosmological Models from Galaxy Clustering and Weak Lensing." In: (2018). arXiv: 1810.02499 [astro-ph.CO] (cit. on p. 1).

[9] Adam G. Riess et al. "Observational evidence from supernovae for an accelerating universe and a cosmological constant." In: *Astron. J.* 116 (1998), pp. 1009–1038. DOI: 10.1086/300499. arXiv: astro-ph/9805201 [astro-ph] (cit. on pp. 1, 4).

[10] S. Perlmutter et al. "Measurements of Omega and Lambda from 42 high redshift supernovae." In: *Astrophys. J.* 517 (1999), pp. 565–586. DOI: 10.1086/307221. arXiv: astro-ph/9812133 [astro-ph] (cit. on pp. 1, 4).

[11] Douglas Clowe et al. "A direct empirical proof of the existence of dark matter." In: *Astrophys. J.* 648 (2006), pp. L109–L113. DOI: 10.1086/508162. arXiv: astro-ph/0608407 [astro-ph] (cit. on pp. 1, 6, 8).

[12] *ESA Science and Technology* (cit. on p. 1).

[13] Edward W. Kolb and Michael S. Turner. "The Early Universe." In: *Front. Phys.* 69 (1990), pp. 1–547 (cit. on p. 2).

[14] Steven Weinberg. *Cosmology*. 2008. ISBN: 9780198526827. URL: http://www.oup.com/uk/catalogue/?ci=9780198526827 (cit. on p. 2).

[15] Scott Dodelson. *Modern Cosmology*. Amsterdam: Academic Press, 2003. ISBN: 9780122191411. URL: http://www.slac.stanford.edu/spires/find/books/www?cl=QB981:D62:2003 (cit. on pp. 2, 59).

[16] Robert M. Wald. *General Relativity*. Chicago, USA: Chicago Univ. Pr., 1984. DOI: 10.7208/chicago/9780226870373.001.0001 (cit. on p. 2).

[17] Adam G. Riess et al. "Milky Way Cepheid Standards for Measuring Cosmic Distances and Application to Gaia DR2: Implications for the Hubble Constant." In: *Astrophys. J.* 861.2 (2018), p. 126. DOI: 10.3847/1538-4357/aac82e. arXiv: 1804.10655 [astro-ph.CO] (cit. on p. 3).

[18] D. J. Fixsen. "The Temperature of the Cosmic Microwave Background." In: *Astrophys. J.* 707.2 (2009), pp. 916–920. DOI: 10.1088/0004-637X/707/2/916. arXiv: 0911.1955 [astro-ph.CO] (cit. on p. 5).

[19] C. L. Bennett et al. "Nine-year Wilkinson Microwave Anisotropy Probe (WMAP) Observations: Final Maps and Results." In: *Astrophys. J.* 208.2, 20 (2013), p. 20. DOI: 10.1088/0067-0049/208/2/20. arXiv: 1212.5225 [astro-ph.CO] (cit. on p. 6).

[20] Wayne T. Hu. "Wandering in the Background: A CMB Explorer." PhD thesis. UC, Berkeley, 1995. arXiv: astro-ph/9508126 [astro-ph] (cit. on p. 6).

[21] *Ringing in the New Cosmology* (cit. on p. 6).

[22] Marusa Bradac et al. "Revealing the properties of dark matter in the merging cluster MACSJ0025.4-1222." In: *Astrophys. J.* 687 (2008), p. 959. DOI: 10.1086/591246. arXiv: 0806.2320 [astro-ph] (cit. on pp. 6, 8).

[23] M. J. Jee et al. "Hubble Space Telescope Advanced Camera for Surveys Weak-Lensing and Chandra X-Ray Studies of the High-Redshift Cluster MS 1054-0321." In: *Astrophys. J.* 634 (Dec. 2005), pp. 813–832. DOI: 10.1086/497001. eprint: astro-ph/0508044 (cit. on pp. 6, 8).

[24] *Chandra X-ray Observatory* (cit. on p. 6).

[25] Kyu-Hyun Chae. "The Cosmic Lens All-Sky Survey: statistical strong lensing, cosmological parameters, and global properties of galaxy populations." In: *Monthly Notices of the Royal Astronomical Society* 346.3 (Dec. 2003), pp. 746–772. ISSN: 0035-8711. DOI: 10.1111/j.1365-2966.2003.07092.x. eprint: http://oup.prod.sis.lan/mnras/article-pdf/346/3/746/3046881/346-3-746.pdf (cit. on p. 7).

[26] Raphael Gavazzi et al. "The Sloan Lens ACS Survey. 4. The mass density profile of early-type galaxies out to 100 effective radii." In: *Astrophys. J.* 667 (2007), pp. 176–190. DOI: 10.1086/519237. arXiv: astro-ph/0701589 [astro-ph] (cit. on p. 7).

[27] Richard Massey, Thomas Kitching, and Johan Richard. "The dark matter of gravitational lensing." In: *Rept. Prog. Phys.* 73 (2010), p. 086901. DOI: 10.1088/0034-4885/73/8/086901. arXiv: 1001.1739 [astro-ph.CO] (cit. on p. 7).

[28] F. Zwicky. "Die Rotverschiebung von extragalaktischen Nebeln." In: *Helv. Phys. Acta* 6 (1933). [Gen. Rel. Grav.41,207(2009)], pp. 110–127. DOI: 10.1007/s10714-008-0707-4 (cit. on p. 7).

[29] V. C. Rubin and W. K. Ford Jr. "Rotation of the Andromeda Nebula from a Spectroscopic Survey of Emission Regions." In: *Astrophys. J.* 159 (Feb. 1970), p. 379. DOI: 10.1086/150317 (cit. on p. 7).

[30] V. C. Rubin, N. Thonnard, and W. K. Ford Jr. "Rotational properties of 21 SC galaxies with a large range of luminosities and radii, from NGC 4605 /R = 4kpc/ to UGC 2885 /R = 122 kpc/." In: *Astrophys. J.* 238 (1980), p. 471. DOI: 10.1086/158003 (cit. on p. 7).

[31] Massimo Persic, Paolo Salucci, and Fulvio Stel. "The Universal rotation curve of spiral galaxies: 1. The Dark matter connection." In: *Mon. Not. Roy. Astron. Soc.* 281 (1996), p. 27. DOI: 10.1093/mnras/281.1.27, 10.1093/mnras/278.1.27. arXiv: astro-ph/9506004 [astro-ph] (cit. on p. 7).

[32] P. J. E. Peebles. "Large-scale background temperature and mass fluctuations due to scale-invariant primeval perturbations." In: *Astrophys. J.* 263 (Dec. 1982), pp. L1–L5. DOI: 10.1086/183911 (cit. on p. 7).

[33] G. R. Blumenthal et al. "Formation of galaxies and large-scale structure with cold dark matter." In: *Nature* 311 (Oct. 1984), pp. 517–525. DOI: 10.1038/311517a0 (cit. on p. 7).

[34] E. Aprile et al. "Dark Matter Search Results from a One Ton-Year Exposure of XENON1T." In: *Phys. Rev. Lett.* 121.11 (2018), p. 111302. DOI: 10.1103/PhysRevLett.121.111302. arXiv: 1805.12562 [astro-ph.CO] (cit. on p. 7).

[35] D. S. Akerib et al. "Results from a search for dark matter in the complete LUX exposure." In: *Phys. Rev. Lett.* 118.2 (2017), p. 021303. DOI: 10.1103/PhysRevLett.118.021303. arXiv: 1608.07648 [astro-ph.CO] (cit. on p. 7).

[36] R. Agnese et al. "First Dark Matter Constraints from a SuperCDMS Single-Charge Sensitive Detector." In: *Phys. Rev. Lett.* 121.5 (2018). [Erratum: Phys. Rev. Lett.122,no.6,069901(2019)], p. 051301. DOI: 10.1103/PhysRevLett.122.069901, 10.1103/PhysRevLett.121.051301. arXiv: 1804.10697 [hep-ex] (cit. on p. 7).

[37] Andi Tan et al. "Dark Matter Results from First 98.7 Days of Data from the PandaX-II Experiment." In: *Phys. Rev. Lett.* 117.12 (2016), p. 121303. DOI: 10.1103/PhysRevLett.117.121303. arXiv: 1607.07400 [hep-ex] (cit. on p. 7).

[38] F. Petricca et al. "First results on low-mass dark matter from the CRESST-III experiment." In: *15th International Conference on Topics in Astroparticle and Underground Physics (TAUP 2017) Sudbury, Ontario, Canada, July 24-28, 2017*. 2017. arXiv: 1711.07692 [astro-ph.CO] (cit. on p. 7).

[39] H. Abdalla et al. "Searches for gamma-ray lines and 'pure WIMP' spectra from Dark Matter annihilations in dwarf galaxies with H.E.S.S." In: *JCAP* 1811.11 (2018), p. 037. DOI: 10.1088/1475-7516/2018/11/037. arXiv: 1810.00995 [astro-ph.HE] (cit. on p. 7).

[40] M. G. Aartsen et al. "Search for neutrinos from decaying dark matter with IceCube." In: *Eur. Phys. J.* C78.10 (2018), p. 831. DOI: 10.1140/epjc/s10052-018-6273-3. arXiv: 1804.03848 [astro-ph.HE] (cit. on p. 7).

[41] M. G. Aartsen et al. "Search for Neutrinos from Dark Matter Self-Annihilations in the center of the Milky Way with 3 years of IceCube/DeepCore." In: *Eur. Phys. J.* C77.9 (2017), p. 627. DOI: 10.1140/epjc/s10052-017-5213-y. arXiv: 1705.08103 [hep-ex] (cit. on p. 7).

[42] A. Albert et al. "Searching for Dark Matter Annihilation in Recently Discovered Milky Way Satellites with Fermi-LAT." In: *Astrophys. J.* 834.2 (2017), p. 110. DOI: 10.3847/1538-4357/834/2/110. arXiv: 1611.03184 [astro-ph.HE] (cit. on p. 7).

[43] M. L. Ahnen et al. "Indirect dark matter searches in the dwarf satellite galaxy Ursa Major II with the MAGIC Telescopes." In: *JCAP* 1803.03 (2018), p. 009. DOI: 10.1088/1475-7516/2018/03/009. arXiv: 1712.03095 [astro-ph.HE] (cit. on p. 7).

[44] Morad Aaboud et al. "Search for dark matter and other new phenomena in events with an energetic jet and large missing transverse momentum using the ATLAS detector." In: *JHEP* 01 (2018), p. 126. DOI: 10.1007/JHEP01(2018)126. arXiv: 1711.03301 [hep-ex] (cit. on p. 7).

[45] Morad Aaboud et al. "Search for dark matter produced in association with bottom or top quarks in $\sqrt{s} = 13$ TeV pp collisions with the ATLAS detector." In: *Eur. Phys. J.* C78.1 (2018), p. 18. DOI: 10.1140/epjc/s10052-017-5486-1. arXiv: 1710.11412 [hep-ex] (cit. on p. 7).

[46] Vardan Khachatryan et al. "Search for dark matter, extra dimensions, and unparticles in monojet events in proton–proton collisions at $\sqrt{s} = 8$ TeV." In: *Eur. Phys. J.* C75.5 (2015), p. 235. DOI: 10.1140/epjc/s10052-015-3451-4. arXiv: 1408.3583 [hep-ex] (cit. on p. 7).

[47] Manoj Kaplinghat, Sean Tulin, and Hai-Bo Yu. "Dark Matter Halos as Particle Colliders: Unified Solution to Small-Scale Structure Puzzles from Dwarfs to Clusters." In: *Phys. Rev. Lett.* 116.4 (2016), p. 041302. DOI: 10.1103/PhysRevLett.116.041302. arXiv: 1508.03339 [astro-ph.CO] (cit. on pp. 8, 13).

[48] Gary Steigman, Basudeb Dasgupta, and John F. Beacom. "Precise Relic WIMP Abundance and its Impact on Searches for Dark Matter Annihilation." In: *Phys. Rev.* D86 (2012), p. 023506. DOI: 10.1103/PhysRevD.86.023506. arXiv: 1204.3622 [hep-ph] (cit. on p. 8).

[49] Julio F. Navarro, Carlos S. Frenk, and Simon D. M. White. "A Universal density profile from hierarchical clustering." In: *Astrophys. J.* 490 (1997), pp. 493–508. DOI: 10.1086/304888. arXiv: astro-ph/9611107 [astro-ph] (cit. on p. 9).

[50] S. S. McGaugh, V. C. Rubin, and W. J. G. de Blok. "High-Resolution Rotation Curves of Low Surface Brightness Galaxies. I. Data." In: *"The Astronomical Journal"* 122 (Nov. 2001), pp. 2381–2395. DOI: 10.1086/323448. eprint: astro-ph/0107326 (cit. on p. 9).

[51] D. Marchesini et al. "Halpha rotation curves: the soft core question." In: *Astrophys. J.* 575 (2002), pp. 801–813. DOI: 10.1086/341475. arXiv: astro-ph/0202075 [astro-ph] (cit. on p. 9).

[52] Rachel Kuzio de Naray, Stacy S. McGaugh, and W. J. G. de Blok. "Mass Models for Low Surface Brightness Galaxies with High Resolution Optical Velocity Fields." In: *Astrophys. J.* 676 (2008), pp. 920–943. DOI: 10.1086/527543. arXiv: 0712.0860 [astro-ph] (cit. on p. 9).

[53] W. J. G. de Blok et al. "High-Resolution Rotation Curves and Galaxy Mass Models from THINGS." In: *Astrophys. J.* 136 (Dec. 2008), pp. 2648–2719. DOI: 10.1088/0004-6256/136/6/2648. arXiv: 0810.2100 (cit. on p. 9).

[54] S.-H. Oh et al. "The Central Slope of Dark Matter Cores in Dwarf Galaxies: Simulations versus THINGS." In: *The Astronomical Journal* 142, 24 (July 2011), p. 24. DOI: 10.1088/0004-6256/142/1/24. arXiv: 1011.2777 (cit. on p. 9).

[55] Kyle A. Oman et al. "The unexpected diversity of dwarf galaxy rotation curves." In: *Mon. Not. Roy. Astron. Soc.* 452.4 (2015), pp. 3650–3665. DOI: 10.1093/mnras/stv1504. arXiv: 1504.01437 [astro-ph.GA] (cit. on p. 9).

[56] E. Tollet et al. "NIHAO - IV: core creation and destruction in dark matter density profiles across cosmic time." In: *Mon. Not. Roy. Astron. Soc.* 456 (Mar. 2016), pp. 3542–3552. DOI: 10.1093/mnras/stv2856. arXiv: 1507.03590 (cit. on p. 9).

[57] Alex Fitts et al. "FIRE in the Field: Simulating the Threshold of Galaxy Formation." In: *Mon. Not. Roy. Astron. Soc.* 471.3 (2017), pp. 3547–3562. DOI: 10.1093/mnras/stx1757. arXiv: 1611.02281 [astro-ph.GA] (cit. on p. 9).

[58] M. Boylan-Kolchin, J. S. Bullock, and M. Kaplinghat. "Too big to fail? The puzzling darkness of massive Milky Way subhaloes." In: *Mon. Not. Roy. Astron. Soc.* 415 (July 2011), pp. L40–L44. DOI: 10.1111/j.1745-3933.2011.01074.x. arXiv: 1103.0007 [astro-ph.CO] (cit. on p. 9).

[59] E. J. Tollerud, M. Boylan-Kolchin, and J. S. Bullock. "M31 satellite masses compared to ΛCDM subhaloes." In: *Mon. Not. Roy. Astron. Soc.* 440 (June 2014), pp. 3511–3519. DOI: 10.1093/mnras/stu474. arXiv: 1403.6469 (cit. on p. 9).

[60] James S. Bullock and Michael Boylan-Kolchin. "Small-Scale Challenges to the ΛCDM Paradigm." In: *Ann. Rev. Astron. Astrophys.* 55 (2017), pp. 343–387. DOI: 10.1146/annurev-astro-091916-055313. arXiv: 1707.04256 [astro-ph.CO] (cit. on pp. 10, 11).

[61] T. Sawala et al. "The APOSTLE simulations: solutions to the Local Group's cosmic puzzles." In: *Mon. Not. Roy. Astron. Soc.* 457 (Apr. 2016), pp. 1931–1943. DOI: 10.1093/mnras/stw145. arXiv: 1511.01098 (cit. on p. 10).

[62] Joshua D. Simon et al. "High-resolution measurements of the halos of four dark matter-dominated galaxies: Deviations from a universal density profile." In: *Astrophys. J.* 621 (2005), pp. 757–776. DOI: 10.1086/427684. arXiv: astro-ph/0412035 [astro-ph] (cit. on p. 10).

[63] A. Drlica-Wagner et al. "Eight Ultra-faint Galaxy Candidates Discovered in Year Two of the Dark Energy Survey." In: *Astrophys. J.* 813.2 (2015), p. 109. DOI: 10.1088/0004-637X/813/2/109. arXiv: 1508.03622 [astro-ph.GA] (cit. on p. 10).

[64] B. F. Griffen et al. "The Caterpillar Project: A Large Suite of Milky Way Sized Halos." In: *Astrophys. J.* 818, 10 (Feb. 2016), p. 10. DOI: 10.3847/0004-637X/818/1/10. arXiv: 1509.01255 (cit. on p. 10).

[65] P. Bode, J. P. Ostriker, and N. Turok. "Halo Formation in Warm Dark Matter Models." In: *ApJ* 556 (July 2001), pp. 93–107. DOI: 10.1086/321541. eprint: astro-ph/0010389 (cit. on p. 11).

[66] E. J. Tollerud et al. "Hundreds of Milky Way Satellites? Luminosity Bias in the Satellite Luminosity Function." In: *ApJ* 688 (Nov. 2008), pp. 277–289. DOI: 10.1086/592102. arXiv: 0806.4381 (cit. on p. 11).

[67] Antonino Del Popolo and Morgan Le Delliou. "Small scale problems of the ΛCDM model: a short review." In: *Galaxies* 5.1 (2017), p. 17. DOI: 10.3390/galaxies5010017. arXiv: 1606.07790 [astro-ph.CO] (cit. on p. 11).

[68] David H. Weinberg et al. "Cold dark matter: controversies on small scales." In: *Proc. Nat. Acad. Sci.* 112 (2015), pp. 12249–12255. DOI: 10.1073/pnas.1308716112. arXiv: 1306.0913 [astro-ph.CO] (cit. on p. 11).

[69] David N. Spergel and Paul J. Steinhardt. "Observational evidence for selfinteracting cold dark matter." In: *Phys. Rev. Lett.* 84 (2000), pp. 3760–3763. DOI: 10.1103/PhysRevLett.84.3760. arXiv: astro-ph/9909386 [astro-ph] (cit. on p. 13).

[70] M. Vogelsberger, J. Zavala, and A. Loeb. "Subhaloes in self-interacting galactic dark matter haloes." In: *Mon. Not. Roy. Astron. Soc.* 423 (July 2012), pp. 3740–3752. DOI: 10.1111/j.1365-2966.2012.21182.x. arXiv: 1201.5892 (cit. on p. 13).

[71] A. H. G. Peter et al. "Cosmological simulations with self-interacting dark matter - II. Halo shapes versus observations." In: *Mon. Not. Roy. Astron. Soc.* 430 (Mar. 2013), pp. 105–120. DOI: 10.1093/mnras/sts535. arXiv: 1208.3026 (cit. on p. 13).

[72] A. B. Fry et al. "All about baryons: revisiting SIDM predictions at small halo masses." In: *Mon. Not. Roy. Astron. Soc.* 452 (Sept. 2015), pp. 1468–1479. DOI: 10.1093/mnras/stv1330. arXiv: 1501.00497 (cit. on p. 13).

[73] O. D. Elbert et al. "Core formation in dwarf haloes with self-interacting dark matter: no fine-tuning necessary." In: *Mon. Not. Roy. Astron. Soc.* 453 (Oct. 2015), pp. 29–37. DOI: 10.1093/mnras/stv1470. arXiv: 1412.1477 (cit. on p. 13).

[74] Tao Ren et al. "Reconciling the Diversity and Uniformity of Galactic Rotation Curves with Self-Interacting Dark Matter." In: (2018). arXiv: 1808.05695 [astro-ph.GA] (cit. on p. 13).

[75] Omid Sameie et al. "Self-Interacting Dark Matter Subhalos in the Milky Way's Tides." In: (2019). arXiv: 1904.07872 [astro-ph.GA] (cit. on p. 13).

[76] Steven Weinberg. "Goldstone Bosons as Fractional Cosmic Neutrinos." In: *Phys. Rev. Lett.* 110.24 (2013), p. 241301. DOI: 10.1103/PhysRevLett.110.241301. arXiv: 1305.1971 [astro-ph.CO] (cit. on pp. 14, 27, 28).

[77] Camilo Garcia-Cely, Alejandro Ibarra, and Emiliano Molinaro. "Dark matter production from Goldstone boson interactions and implications for direct searches and dark radiation." In: *JCAP* 1311 (2013), p. 061. DOI: 10.1088/1475-7516/2013/11/061. arXiv: 1310.6256 [hep-ph] (cit. on pp. 14, 28).

[78] Xiaoyong Chu and Basudeb Dasgupta. "Dark Radiation Alleviates Problems with Dark Matter Halos." In: *Phys. Rev. Lett.* 113.16 (2014), p. 161301. DOI: 10.1103/PhysRevLett.113.161301. arXiv: 1404.6127 [hep-ph] (cit. on pp. 14, 29).

[79] M. C. Bento et al. "Selfinteracting dark matter and invisibly decaying Higgs." In: *Phys. Rev.* D62 (2000), p. 041302. DOI: 10.1103/PhysRevD.62.041302. arXiv: astro-ph/0003350 [astro-ph] (cit. on p. 14).

[80] John McDonald. "Thermally generated gauge singlet scalars as selfinteracting dark matter." In: *Phys. Rev. Lett.* 88 (2002), p. 091304. DOI: 10.1103/PhysRevLett.88.091304. arXiv: hep-ph/0106249 [hep-ph] (cit. on p. 14).

[81] Jonathan L. Feng, Manoj Kaplinghat, and Hai-Bo Yu. "Halo Shape and Relic Density Exclusions of Sommerfeld-Enhanced Dark Matter Explanations of Cosmic Ray Excesses." In: *Phys. Rev. Lett.* 104 (2010), p. 151301. DOI: 10.1103/PhysRevLett.104.151301. arXiv: 0911.0422 [hep-ph] (cit. on pp. 14, 23).

[82] Sean Tulin, Hai-Bo Yu, and Kathryn M. Zurek. "Beyond Collisionless Dark Matter: Particle Physics Dynamics for Dark Matter Halo Structure." In: *Phys. Rev.* D87.11 (2013), p. 115007. DOI: 10.1103/PhysRevD.87.115007. arXiv: 1302.3898 [hep-ph] (cit. on p. 14).

[83] Katelin Schutz and Tracy R. Slatyer. "Self-Scattering for Dark Matter with an Excited State." In: *JCAP* 1501.01 (2015), p. 021. DOI: 10.1088/1475-7516/2015/01/021. arXiv: 1409.2867 [hep-ph] (cit. on pp. 14, 50).

[84] James M. Cline et al. "Scattering properties of dark atoms and molecules." In: *Phys. Rev.* D89.4 (2014), p. 043514. DOI: 10.1103/PhysRevD.89.043514. arXiv: 1311.6468 [hep-ph] (cit. on p. 14).

[85] Kimberly K. Boddy et al. "Hidden Sector Hydrogen as Dark Matter: Small-scale Structure Formation Predictions and the Importance of Hyperfine Interactions." In: *Phys. Rev.* D94.12 (2016), p. 123017. DOI: 10.1103/PhysRevD.94.123017. arXiv: 1609.03592 [hep-ph] (cit. on pp. 14, 54).

[86] Matthew R. Buckley and Patrick J. Fox. "Dark Matter Self-Interactions and Light Force Carriers." In: *Phys. Rev.* D81 (2010), p. 083522. DOI: 10.1103/PhysRevD.81.083522. arXiv: 0911.3898 [hep-ph] (cit. on pp. 14, 22).

[87] Abraham Loeb and Neal Weiner. "Cores in Dwarf Galaxies from Dark Matter with a Yukawa Potential." In: *Phys. Rev. Lett.* 106 (2011), p. 171302. DOI: 10.1103/PhysRevLett.106.171302. arXiv: 1011.6374 [astro-ph.CO] (cit. on p. 14).

[88] Sean Tulin, Hai-Bo Yu, and Kathryn M. Zurek. "Resonant Dark Forces and Small Scale Structure." In: *Phys. Rev. Lett.* 110.11 (2013), p. 111301. DOI: 10.1103/PhysRevLett.110.111301. arXiv: 1210.0900 [hep-ph] (cit. on p. 14).

[89] Kimberly K. Boddy et al. "Self-Interacting Dark Matter from a Non-Abelian Hidden Sector." In: *Phys. Rev.* D89.11 (2014), p. 115017. DOI: 10.1103/PhysRevD.89.115017. arXiv: 1402.3629 [hep-ph] (cit. on p. 14).

[90] P. Ko and Y. Tang. "Self-interacting scalar dark matter with local Z_3 symmetry." In: *JCAP* 1405 (2014), p. 047. DOI: 10.1088/1475-7516/2014/05/047. arXiv: 1402.6449 [hep-ph] (cit. on p. 14).

[91] Zhaofeng Kang. "View FImP miracle (by scale invariance) à la self-interaction." In: *Phys. Lett.* B751 (2015), pp. 201–204. DOI: 10.1016/j.physletb.2015.10.031. arXiv: 1505.06554 [hep-ph] (cit. on p. 14).

[92] Brando Bellazzini, Mathieu Cliche, and Philip Tanedo. "Effective theory of self-interacting dark matter." In: *Phys. Rev.* D88.8 (2013), p. 083506. DOI: 10.1103/PhysRevD.88.083506. arXiv: 1307.1129 [hep-ph] (cit. on p. 14).

[93] Eric D. Carlson, Marie E. Machacek, and Lawrence J. Hall. "Self-interacting dark matter." In: *Astrophys. J.* 398 (1992), pp. 43–52. DOI: 10.1086/171833 (cit. on pp. 14, 59).

[94] Alon E. Faraggi and Maxim Pospelov. "Selfinteracting dark matter from the hidden heterotic string sector." In: *Astropart. Phys.* 16 (2002), pp. 451–461. DOI: 10.1016/S0927-6505(01)00121-9. arXiv: hep-ph/0008223 [hep-ph] (cit. on pp. 14, 59).

[95] Mads T. Frandsen, Subir Sarkar, and Kai Schmidt-Hoberg. "Light asymmetric dark matter from new strong dynamics." In: *Phys. Rev.* D84 (2011), p. 051703. DOI: 10.1103/PhysRevD.84.051703. arXiv: 1103.4350 [hep-ph] (cit. on p. 14).

[96] James M. Cline et al. "Composite strongly interacting dark matter." In: *Phys. Rev.* D90.1 (2014), p. 015023. DOI: 10.1103/PhysRevD.90.015023. arXiv: 1312.3325 [hep-ph] (cit. on p. 14).

[97] Lev Davidovich Landau and E. M. Lifshits. *Quantum Mechanics*. Vol. v.3. Course of Theoretical Physics. Oxford: Butterworth-Heinemann, 1991. ISBN: 9780750635394 (cit. on pp. 16, 22).

[98] S. Cassel. "Sommerfeld factor for arbitrary partial wave processes." In: *J. Phys.* G37 (2010), p. 105009. DOI: 10.1088/0954-3899/37/10/105009. arXiv: 0903.5307 [hep-ph] (cit. on pp. 17, 20–22, 38, 39).

[99] A. Sommerfeld. "Über die Beugung und Bremsung der Elektronen." In: *Annalen der Physik* 403.3 (1931), pp. 257–330. ISSN: 1521-3889. DOI: 10.1002/andp.19314030302. URL: http://dx.doi.org/10.1002/andp.19314030302 (cit. on pp. 18, 20).

[100] Junji Hisano, S. Matsumoto, and Mihoko M. Nojiri. "Unitarity and higher order corrections in neutralino dark matter annihilation into two photons." In: *Phys. Rev.* D67 (2003), p. 075014. DOI: 10.1103/PhysRevD.67.075014. arXiv: hep-ph/0212022 [hep-ph] (cit. on p. 19).

[101] Junji Hisano, Shigeki Matsumoto, and Mihoko M. Nojiri. "Explosive dark matter annihilation." In: *Phys. Rev. Lett.* 92 (2004), p. 031303. DOI: 10.1103/PhysRevLett.92.031303. arXiv: hep-ph/0307216 [hep-ph] (cit. on p. 19).

[102] Junji Hisano et al. "Non-perturbative effect on dark matter annihilation and gamma ray signature from galactic center." In: *Phys. Rev.* D71 (2005), p. 063528. DOI: 10.1103/PhysRevD.71.063528. arXiv: hep-ph/0412403 [hep-ph] (cit. on p. 19).

[103] Junji Hisano et al. "Non-perturbative effect on thermal relic abundance of dark matter." In: *Phys. Lett.* B646 (2007), pp. 34–38. DOI: 10.1016/j.physletb.2007.01.012. arXiv: hep-ph/0610249 [hep-ph] (cit. on p. 19).

[104] Marco Cirelli, Alessandro Strumia, and Matteo Tamburini. "Cosmology and Astrophysics of Minimal Dark Matter." In: *Nucl. Phys.* B787 (2007), pp. 152–175. DOI: 10.1016/j.nuclphysb.2007.07.023. arXiv: 0706.4071 [hep-ph] (cit. on p. 19).

[105] Nima Arkani-Hamed et al. "A Theory of Dark Matter." In: *Phys. Rev.* D79 (2009), p. 015014. DOI: 10.1103/PhysRevD.79.015014. arXiv: 0810.0713 [hep-ph] (cit. on pp. 19, 28).

[106] Oscar Adriani et al. "An anomalous positron abundance in cosmic rays with energies 1.5-100 GeV." In: *Nature* 458 (2009), pp. 607–609. DOI: 10.1038/nature07942. arXiv: 0810.4995 [astro-ph] (cit. on p. 19).

[107] M. Ackermann et al. "Measurement of separate cosmic-ray electron and positron spectra with the Fermi Large Area Telescope." In: *Phys. Rev. Lett.* 108 (2012), p. 011103. DOI: 10.1103/PhysRevLett.108.011103. arXiv: 1109.0521 [astro-ph.HE] (cit. on p. 19).

[108] C. Grimani et al. "Measurements of the absolute energy spectra of cosmic-ray positrons and electrons above 7-GeV." In: *Astron. Astrophys.* 392 (2002), pp. 287–294. DOI: 10.1051/0004-6361:20020845 (cit. on p. 19).

[109] M. Boezio et al. "Measurements of cosmic-ray electrons and positrons by the Wizard/CAPRICE collaboration." In: *Adv. Space Res.* 27.4 (2001), pp. 669–674. DOI: 10.1016/S0273-1177(01)00108-9 (cit. on p. 19).

[110] M. A. DuVernois et al. "Cosmic ray electrons and positrons from 1-GeV to 100-GeV: Measurements with HEAT and their interpretation." In: *Astrophys. J.* 559 (2001), pp. 296–303. DOI: 10.1086/322324 (cit. on p. 19).

[111] Steen Hannestad and Thomas Tram. "Sommerfeld Enhancement of DM Annihilation: Resonance Structure, Freeze-Out and CMB Spectral Bound." In: *JCAP* 1101 (2011), p. 016. DOI: 10.1088/1475-7516/2011/01/016. arXiv: 1008.1511 [astro-ph.CO] (cit. on p. 20).

[112] J. J. Sakurai and Jim Napolitano. *Modern Quantum Mechanics*. 2nd ed. Cambridge University Press, 2017 (cit. on p. 22).

[113] Carl Ramsauer. "Über den Wirkungsquerschnitt der Gasmoleküle gegenüber langsamen Elektronen." In: *Annalen der Physik* 369.6 (1921), pp. 513–540. DOI: 10.1002/andp.19213690603. eprint: https://onlinelibrary.wiley.com/doi/pdf/10.1002/andp.19213690603. URL: https://onlinelibrary.wiley.com/doi/abs/10.1002/andp.19213690603 (cit. on p. 23).

[114] Ryan Cooke et al. "Precision measures of the primordial abundance of deuterium." In: *Astrophys. J.* 781.1 (2014), p. 31. DOI: 10.1088/0004-637X/781/1/31. arXiv: 1308.3240 [astro-ph.CO] (cit. on pp. 24, 69, 70).

[115] Yasunori Nomura and Jesse Thaler. "Dark Matter through the Axion Portal." In: *Phys. Rev.* D79 (2009), p. 075008. DOI: 10.1103/PhysRevD.79.075008. arXiv: 0810.5397 [hep-ph] (cit. on p. 28).

[116] Torsten Bringmann and Stefan Hofmann. "Thermal decoupling of WIMPs from first principles." In: *JCAP* 0704 (2007). [Erratum: JCAP1603,no.03,E02(2016)], p. 016. DOI: 10.1088/1475-7516/2007/04/016,10.1088/1475-7516/2016/03/E02. arXiv: hep-ph/0612238 [hep-ph] (cit. on p. 29).

[117] Geoffrey T. Bodwin, Eric Braaten, and G. Peter Lepage. "Rigorous QCD analysis of inclusive annihilation and production of heavy quarkonium." In: *Phys. Rev.* D51 (1995). [Erratum: Phys. Rev.D55,5853(1997)], pp. 1125–1171. DOI: 10.1103/PhysRevD.55.5853,10.1103/PhysRevD.51.1125. arXiv: hep-ph/9407339 [hep-ph] (cit. on p. 31).

[118] Michael E. Peskin and Daniel V. Schroeder. *An Introduction to quantum field theory*. Reading, USA: Addison-Wesley, 1995. ISBN: 9780201503975, 0201503972. URL: http://www.slac.stanford.edu/~mpeskin/QFT.html (cit. on p. 32).

[119] Vladyslav Shtabovenko, Rolf Mertig, and Frederik Orellana. "New Developments in FeynCalc 9.0." In: *Comput. Phys. Commun.* 207 (2016), pp. 432–444. DOI: 10.1016/j.cpc.2016.06.008. arXiv: 1601.01167 [hep-ph] (cit. on p. 32).

[120] Tracy R. Slatyer. "The Sommerfeld enhancement for dark matter with an excited state." In: *JCAP* 1002 (2010), p. 028. DOI: 10.1088/1475-7516/2010/02/028. arXiv: 0910.5713 [hep-ph] (cit. on pp. 33, 39).

[121] S. N. Ershov, J. S. Vaagen, and M. V. Zhukov. "Modified variable phase method for the solution of coupled radial Schrodinger equations." In: *Phys. Rev.* C84 (2011), p. 064308. DOI: 10.1103/PhysRevC.84.064308 (cit. on p. 35).

[122] M. Beneke, C. Hellmann, and P. Ruiz-Femenia. "Non-relativistic pair annihilation of nearly mass degenerate neutralinos and charginos III. Computation of the Sommerfeld enhancements." In: *JHEP* 05 (2015), p. 115. DOI: 10.1007/JHEP05(2015)115. arXiv: 1411.6924 [hep-ph] (cit. on p. 35).

[123] M. Aguilar et al. "Towards Understanding the Origin of Cosmic-Ray Positrons." In: *Phys. Rev. Lett.* 122.4 (2019), p. 041102. DOI: 10.1103/PhysRevLett.122.041102 (cit. on pp. 39, 40).

[124] Marco Cirelli et al. "PPPC 4 DM ID: A Poor Particle Physicist Cookbook for Dark Matter Indirect Detection." In: *JCAP* 1103 (2011). [Erratum: JCAP1210,E01(2012)], p. 051. DOI: 10.1088/1475-7516/2012/10/E01,10.1088/1475-7516/2011/03/051. arXiv: 1012.4515 [hep-ph] (cit. on p. 40).

[125] B. Zygelman, A. Dalgarno, and R. D. Sharma. "Molecular theory of collision-induced fine-structure transitions in atomic oxygen." In: *Phys. Rev. A* 49 (4 1994), pp. 2587–2606. DOI: 10.1103/PhysRevA.49.2587. URL: https://link.aps.org/doi/10.1103/PhysRevA.49.2587 (cit. on pp. 45, 47).

[126] F. Calogero. *Variable Phase Approach to Potential Scattering*. Mathematics in Science and Engineering. Elsevier Science, 1967. ISBN: 9780080955421. URL: https://books.google.co.in/books?id=fmjuIREIN8gC (cit. on p. 46).

[127] B.R Johnson. "The multichannel log-derivative method for scattering calculations." In: *Journal of Computational Physics* 13.3 (1973), pp. 445 –449. ISSN: 0021-9991. DOI: 10.1016/0021-9991(73)90049-1. URL: http://www.sciencedirect.com/science/article/pii/0021999173900491 (cit. on p. 48).

[128] B. R. Johnson. "Comment on a recent criticism of the formula used to calculate the *S* matrix in the multichannel log-derivative method." In: *Phys. Rev. A* 32 (2 1985), pp. 1241–1242. DOI: 10.1103/PhysRevA.32.1241. URL: https://link.aps.org/doi/10.1103/PhysRevA.32.1241 (cit. on p. 48).

[129] Mattias Blennow, Stefan Clementz, and Juan Herrero-Garcia. "Self-interacting inelastic dark matter: A viable solution to the small scale structure problems." In: *JCAP* 1703.03 (2017), p. 048. DOI: 10.1088/1475-7516/2017/03/048. arXiv: 1612.06681 [hep-ph] (cit. on p. 50).

[130] George R. Blumenthal et al. "Contraction of Dark Matter Galactic Halos Due to Baryonic Infall." In: *Astrophys. J.* 301 (1986), p. 27. DOI: 10.1086/163867 (cit. on p. 51).

[131] O. Y. Gnedin et al. "Response of Dark Matter Halos to Condensation of Baryons: Cosmological Simulations and Improved Adiabatic Contraction Model." In: *ApJ* 616 (Nov. 2004), pp. 16–26. DOI: 10.1086/424914. eprint: astro-ph/0406247 (cit. on p. 51).

[132] D. Lynden-Bell and P. P. Eggleton. "On the consequences of the gravothermal catastrophe." In: *Mon. Not. Roy. Astron. Soc.* 191 (May 1980), pp. 483–498. DOI: 10.1093/mnras/191.3.483 (cit. on p. 53).

[133] Jason Pollack, David N. Spergel, and Paul J. Steinhardt. "Supermassive Black Holes from Ultra-Strongly Self-Interacting Dark Matter." In: *Astrophys. J.* 804.2 (2015), p. 131. DOI: 10.1088/0004-637X/804/2/131. arXiv: 1501.00017 [astro-ph.CO] (cit. on p. 53).

[134] John Dubinski. "The Effect of dissipation on the shapes of dark halos." In: *Astrophys. J.* 431 (1994), pp. 617–624. DOI: 10.1086/174512. arXiv: astro-ph/9309001 [astro-ph] (cit. on p. 54).

[135] Keita Todoroki and Mikhail V. Medvedev. "Dark matter haloes in the multicomponent model ? II. Density profiles of galactic haloes." In: *Mon. Not. Roy. Astron. Soc.* 483.3 (2019), pp. 4004–4019. DOI: 10.1093/mnras/sty3353. arXiv: 1711.11085 [astro-ph.CO] (cit. on p. 54).

[136] Mark Vogelsberger et al. "Evaporating the Milky Way halo and its satellites with inelastic self-interacting dark matter." In: (2018). DOI: 10.1093/mnras/stz340. arXiv: 1805.03203 [astro-ph.GA] (cit. on p. 54).

[137] Felix Kahlhoefer et al. "Colliding clusters and dark matter self-interactions." In: *Mon. Not. Roy. Astron. Soc.* 437.3 (2014), pp. 2865–2881. DOI: 10.1093/mnras/stt2097. arXiv: 1308.3419 [astro-ph.CO] (cit. on pp. 54, 55).

[138] Janis Kummer, Felix Kahlhoefer, and Kai Schmidt-Hoberg. "Effective description of dark matter self-interactions in small dark matter haloes." In: (2017). arXiv: 1706.04794 [astro-ph.CO] (cit. on p. 54).

[139] J. I. Read et al. "Thin, thick and dark discs in LCDM." In: *Mon. Not. Roy. Astron. Soc.* 389 (2008), pp. 1041–1057. DOI: 10.1111/j.1365-2966.2008.13643.x. arXiv: 0803.2714 [astro-ph] (cit. on p. 56).

[140] Chris W. Purcell, James S. Bullock, and Manoj Kaplinghat. "The Dark Disk of the Milky Way." In: *Astrophys. J.* 703 (2009), pp. 2275–2284. DOI: 10.1088/0004-637X/703/2/2275. arXiv: 0906.5348 [astro-ph.GA] (cit. on p. 56).

[141] Ilias Cholis and Lisa Goodenough. "Consequences of a Dark Disk for the Fermi and PAMELA Signals in Theories with a Sommerfeld Enhancement." In: *JCAP* 1009 (2010), p. 010. DOI: 10.1088/1475-7516/2010/09/010. arXiv: 1006.2089 [astro-ph.HE] (cit. on p. 56).

[142] JiJi Fan et al. "Double-Disk Dark Matter." In: *Phys. Dark Univ.* 2 (2013), pp. 139–156. DOI: 10.1016/j.dark.2013.07.001. arXiv: 1303.1521 [astro-ph.CO] (cit. on p. 56).

[143] JiJi Fan et al. "Dark-Disk Universe." In: *Phys. Rev. Lett.* 110.21 (2013), p. 211302. DOI: 10.1103/PhysRevLett.110.211302. arXiv: 1303.3271 [hep-ph] (cit. on p. 56).

[144] Matthew McCullough and Lisa Randall. "Exothermic Double-Disk Dark Matter." In: *JCAP* 1310 (2013), p. 058. DOI: 10.1088/1475-7516/2013/10/058. arXiv: 1307.4095 [hep-ph] (cit. on p. 56).

[145] Surhud More et al. “Detection of the Splashback Radius and Halo Assembly bias of Massive Galaxy Clusters.” In: *Astrophys. J.* 825.1 (2016), p. 39. DOI: 10.3847/0004-637X/825/1/39. arXiv: 1601.06063 [astro-ph.CO] (cit. on p. 56).

[146] J. A. Fillmore and P. Goldreich. “Self-similiar gravitational collapse in an expanding universe.” In: *Astrophys. J.* 281 (1984), pp. 1–8. DOI: 10.1086/162070 (cit. on p. 56).

[147] E. Bertschinger. “Self - similar secondary infall and accretion in an Einstein-de Sitter universe.” In: *Astrophys. J. Suppl.* 58 (1985), p. 39. DOI: 10.1086/191028 (cit. on p. 56).

[148] Susmita Adhikari, Neal Dalal, and Robert T. Chamberlain. “Splashback in accreting dark matter halos.” In: *JCAP* 1411.11 (2014), p. 019. DOI: 10.1088/1475-7516/2014/11/019. arXiv: 1409.4482 [astro-ph.CO] (cit. on p. 56).

[149] http://risa.stanford.edu/redmapper/ (cit. on p. 56).

[150] E. S. Rykoff et al. “redMaPPer. I. Algorithm and SDSS DR8 Catalog.” In: *ApJ* 785, 104 (Apr. 2014), p. 104. DOI: 10.1088/0004-637X/785/2/104. arXiv: 1303.3562 (cit. on p. 56).

[151] L. B. Okun. “THETONS.” In: *JETP Lett.* 31 (1980). [Pisma Zh. Eksp. Teor. Fiz.31,156(1979)], pp. 144–147 (cit. on p. 59).

[152] Jose E. Juknevich, Dmitry Melnikov, and Matthew J. Strassler. “A Pure-Glue Hidden Valley I. States and Decays.” In: *JHEP* 07 (2009), p. 055. DOI: 10.1088/1126-6708/2009/07/055. arXiv: 0903.0883 [hep-ph] (cit. on p. 59).

[153] Bobby Samir Acharya, Malcolm Fairbairn, and Edward Hardy. “Glueball dark matter in non-standard cosmologies.” In: *JHEP* 07 (2017), p. 100. DOI: 10.1007/JHEP07(2017)100. arXiv: 1704.01804 [hep-ph] (cit. on p. 59).

[154] S. Nussinov. “Technocosmology — could a technibaryon excess provide a “natural” missing mass candidate?” In: *Physics Letters B* 165.1 (1985), pp. 55 –58. ISSN: 0370-2693. DOI: https://doi.org/10.1016/0370-2693(85)90689-6 (cit. on p. 59).

[155] S.M. Barr, R. Sekhar Chivukula, and Edward Farhi. “Electroweak fermion number violation and the production of stable particles in the early universe.” In: *Physics Letters B* 241.3 (1990), pp. 387 –391. ISSN: 0370-2693. DOI: https://doi.org/10.1016/0370-2693(90)91661-T. URL: http://www.sciencedirect.com/science/article/pii/037026939091661T (cit. on p. 59).

[156] Stephen M. Barr. “Baryogenesis, sphalerons and the cogeneration of dark matter.” In: *Phys. Rev.* D44 (1991), pp. 3062–3066. DOI: 10.1103/PhysRevD.44.3062 (cit. on p. 59).

[157] David B. Kaplan. "Single explanation for both baryon and dark matter densities." In: *Phys. Rev. Lett.* 68 (6 1992), pp. 741–743. DOI: 10.1103/PhysRevLett.68.741. URL: https://link.aps.org/doi/10.1103/PhysRevLett.68.741 (cit. on p. 59).

[158] David E. Kaplan, Markus A. Luty, and Kathryn M. Zurek. "Asymmetric Dark Matter." In: *Phys. Rev.* D79 (2009), p. 115016. DOI: 10.1103/PhysRevD.79.115016. arXiv: 0901.4117 [hep-ph] (cit. on p. 59).

[159] Graham D. Kribs et al. "Quirky Composite Dark Matter." In: *Phys. Rev.* D81 (2010), p. 095001. DOI: 10.1103/PhysRevD.81.095001. arXiv: 0909.2034 [hep-ph] (cit. on p. 59).

[160] Mattias Blennow et al. "Aidnogenesis via Leptogenesis and Dark Sphalerons." In: *JHEP* 03 (2011), p. 014. DOI: 10.1007/JHEP03(2011)014. arXiv: 1009.3159 [hep-ph] (cit. on p. 59).

[161] Chung-Pei Ma and Edmund Bertschinger. "Cosmological perturbation theory in the synchronous and conformal Newtonian gauges." In: *Astrophys. J.* 455 (1995), pp. 7–25. DOI: 10.1086/176550. arXiv: astro-ph/9506072 [astro-ph] (cit. on pp. 59, 63).

[162] Alan H. Guth. "The Inflationary Universe: A Possible Solution to the Horizon and Flatness Problems." In: *Phys. Rev.* D23 (1981). [Adv. Ser. Astrophys. Cosmol.3,139(1987)], pp. 347–356. DOI: 10.1103/PhysRevD.23.347 (cit. on p. 63).

[163] Andrei D. Linde. "A New Inflationary Universe Scenario: A Possible Solution of the Horizon, Flatness, Homogeneity, Isotropy and Primordial Monopole Problems." In: *Phys. Lett.* 108B (1982). [Adv. Ser. Astrophys. Cosmol.3,149(1987)], pp. 389–393. DOI: 10.1016/0370-2693(82)91219-9 (cit. on p. 63).

[164] Andreas Albrecht and Paul J. Steinhardt. "Cosmology for Grand Unified Theories with Radiatively Induced Symmetry Breaking." In: *Phys. Rev. Lett.* 48 (1982). [Adv. Ser. Astrophys. Cosmol.3,158(1987)], pp. 1220–1223. DOI: 10.1103/PhysRevLett.48.1220 (cit. on p. 63).

[165] Antony Lewis, Anthony Challinor, and Anthony Lasenby. "Efficient computation of CMB anisotropies in closed FRW models." In: *Astrophys. J.* 538 (2000), pp. 473–476. DOI: 10.1086/309179. arXiv: astro-ph/9911177 [astro-ph] (cit. on pp. 63, 68).

[166] D. Blas, J. Lesgourgues, and T. Tram. "The Cosmic Linear Anisotropy Solving System (CLASS). Part II: Approximation schemes." In: *JCAP* 7, 034 (July 2011), p. 034. DOI: 10.1088/1475-7516/2011/07/034. arXiv: 1104.2933 (cit. on pp. 63, 68).

[167] Wayne Hu. "Structure formation with generalized dark matter." In: *Astrophys. J.* 506 (1998), pp. 485–494. DOI: 10.1086/306274. arXiv: astro-ph/9801234 [astro-ph] (cit. on p. 67).

[168] A. D. Dolgov and M. Fukugita. “Nonequilibrium effect of the neutrino distribution on primordial helium synthesis.” In: *Phys.Rev.D* 46 (Dec. 1992), pp. 5378–5382. DOI: 10.1103/PhysRevD.46.5378 (cit. on p. 69).

[169] S. Hannestad and J. Madsen. “Neutrino decoupling in the early Universe.” In: *Phys.Rev.D* 52 (Aug. 1995), pp. 1764–1769. DOI: 10.1103/PhysRevD.52.1764. eprint: astro-ph/9506015 (cit. on p. 69).

[170] A. D. Dolgov, S. H. Hansen, and D. V. Semikoz. “Non-equilibrium corrections to the spectra of massless neutrinos in the early universe.” In: *Nuclear Physics B* 503 (Feb. 1997), pp. 426–444. DOI: 10.1016/S0550-3213(97)00479-3. eprint: hep-ph/9703315 (cit. on p. 69).

[171] N. Fornengo, C. W. Kim, and J. Song. “Finite temperature effects on the neutrino decoupling in the early Universe.” In: *Phys.Rev.D* 56 (Oct. 1997), pp. 5123–5134. DOI: 10.1103/PhysRevD.56.5123. eprint: hep-ph/9702324 (cit. on p. 69).

[172] G. Mangano et al. “A precision calculation of the effective number of cosmological neutrinos.” In: *Physics Letters B* 534 (May 2002), pp. 8–16. DOI: 10.1016/S0370-2693(02)01622-2. eprint: astro-ph/0111408 (cit. on p. 69).

[173] G. Mangano and P. D. Serpico. “A robust upper limit on N from BBN, circa 2011.” In: *Physics Letters B* 701 (July 2011), pp. 296–299. DOI: 10.1016/j.physletb.2011.05.075. arXiv: 1103.1261 [astro-ph.CO] (cit. on pp. 69, 70).

[174] R. A. Sunyaev and Y. B. Zeldovich. “Small-Scale Fluctuations of Relic Radiation.” In: *Astrophysics and Space Science* 7 (Apr. 1970), pp. 3–19. DOI: 10.1007/BF00653471 (cit. on p. 73).

[175] D. J. Eisenstein and W. Hu. “Baryonic Features in the Matter Transfer Function.” In: *ApJ* 496 (Mar. 1998), pp. 605–614. DOI: 10.1086/305424. eprint: astro-ph/9709112 (cit. on p. 73).

[176] P. A. R. Ade et al. “Planck 2015 results. XIII. Cosmological parameters.” In: *Astron. Astrophys.* 594 (2016), A13. DOI: 10.1051/0004-6361/201525830. arXiv: 1502.01589 [astro-ph.CO] (cit. on pp. 74, 78).

[177] Will J. Percival et al. “The shape of the SDSS DR5 galaxy power spectrum.” In: *Astrophys. J.* 657 (2007), pp. 645–663. DOI: 10.1086/510615. arXiv: astro-ph/0608636 [astro-ph] (cit. on p. 77).

[178] Kevork N. Abazajian et al. “CMB-S4 Science Book, First Edition.” In: (2016). arXiv: 1610.02743 [astro-ph.CO] (cit. on p. 78).